FLUID DYNAMIC STUDY OF BUBBLE ENTRAPMENT DURING ENCAPSULATION

By

Qiang Deng

Dissertation

Submitted to the Faculty of the

Graduate School of Vanderbilt University

in partial fulfillment of the requirements

for the degree of

DOCTOR OF PHILOSOPHY

in

Mechanical Engineering

May, 2007

Nashville, Tennessee

Approved:

Dr. Taylor G. Wang

Dr. Amrutur V. Anilkumar

Dr. Frederick R. Haselton

Dr. G. Kane Jennings

Dr. Dongqing Li

Dr. Alvin C. Powers

To my parents

and

beloved wife, Yuyang Zhou

ACKNOWLEDGEMENTS

I would like to thank my advisors, Dr. Taylor G. Wang and Dr. Amrutur V. Anilkumar for guiding me through this journey at Vanderbilt. As a mentor and dedicated researcher, you both set a perfect example to me on how to conduct a good scientific research. Without your insightful, constructive and inspirational advice, I would have never been able to discover the intriguing beauty of droplets and bubbles as presented in this dissertation. I am especially indebted to Dr. Anilkumar for his effort and patience in improving the presentation of this work.

I am thankful to Mr. Jim Hightower for his assistance in fabrication of the apparatus used in this study, and to Ms. Irena Trenary for assistance in the laboratory. I like to thank members of my thesis committee for their valuable comments. I gratefully acknowledge the support of this research through funds from the National Aeronautics and Space Administration, the Juvenile Diabetes Research Foundation, the Evans-Gilruth Foundation, the Children's Miracle Foundation, and the Ronald McDonald Children's Charities.

Finally, I give my most gracious thanks to each of my family members, my friends, and my loving wife. Without your continued love and support, I would have never made it this far.

TABLE OF CONTENTS

Page

LIST OF TABLES

LIST OF FIGURES

CHAPTER I

INTRODUCTION AND BACKGROUND

Introduction and summery

Over the last two decades, cell encapsulation has emerged as a promising technique to transplant living cells (allo- or xeno- source) without the need for immuno-suppression drugs. Recent results in animal trials show that encapsulated living islets can effectively reverse diabetes in both small and big animals up to six months. In addition to treating diabetes, cell encapsulation may have broad applications in treating major diseases such as cancer, autoimmune deficiency syndrome and a wide range of other disorders resulting from functional defects of native cell systems. The key point of successful cell encapsulation is to develop biocompatible polymer complex capsules with tailored membrane properties. These capsules serve as a media to immobilize living cells, protect them from immune attack and maintain a bio-viable environment for the transplanted cells. Besides some progresses made recently, developing a precise protocol for making uniform capsules with optimal properties has been challenging.

The morphological qualities such as smoothness and roundness of microcapsules are known to be important factors in microcapsule's biocompatibility. In order to improve the capsule's morphology, complete understanding of the dynamics involved in the encapsulation process is essential. Usually, capsules used for cell transplantation are made by dispensing poly-anion drops into a cation solution bath. While many groups have investigated the single drop impact onto liquid pool problem, the phenomenon of

viscous poly-anion drop impact onto a reactive gelling pool, as in encapsulation, has not been systematically studied. The objective of the current work is to examine the problem in the physical plane, through standard criteria like fluid physical properties, impact parameters, and reaction conditions, and point out simplifications in understanding and modeling the problem. The main theme of this dissertation is to experimentally investigate the dynamic process of capsule formation, which involves both fluid dynamic and chemical reaction issues. It is hoped that these studies will help establish the criteria for making physically perfect capsules.

The dissertation is organized as follows: A review of the literature with respect to both cell encapsulation technology and classical drop impact phenomenon is presented in chapter I, where the significance of current study is also discussed. In chapter II the experimental methods and test liquid systems used in current study are briefly described. Chapter III focuses on understanding the liquid drop impact and related free surface signatures from a classical fluid dynamic point of view. The preliminary experimental results on water drop impact onto a water pool are presented first. Then the role of viscosity and surface tension in bubble entrapment during drop impact onto a deep pool of the same liquid is examined in detail. Some results on non-reactive asymmetric drop impact experiments are also reported in the end of chapter III. This establishes a transition from the studies of simple drop impact phenomenon to the more complex study of reactive drop impact as in encapsulation. Chapter IV continues bubble entrapment study in the context of reactive drop impact. The results are compared with the non-reactive system, and some conclusions are drawn based on the observation. Besides the bubble entrapment study, the origins of other morphological issues such as capsule deformation and recovery, and surface

wrinkles and bubble entrapment due to initial contact are identified in three appendixes respectively, where the effects of chemical conditions as well as the kinetic condition on capsule's morphological quality are discussed. Finally, a parametric map for optimal encapsulation operation is provided.

Cell encapsulation

Cell encapsulation has a high potential to treat a variety of human diseases resulting from functional defects of native cell systems. The underlying principle of cell encapsulation is to protect transplanted cells from host immune-attack, while maintaining the cells' functional bioactivity. Three major approaches have been developed during the last two decades: macrocapsules, microcapsules and intravascular devices[1-3]. Microcapsules offer a number of distinct advantages over other methods like: higher diffusivity owing to the greater surface to volume ratio, improved mechanical stability and ease of production and implantation. Thus, spherical microcapsules appear to have the highest therapeutic potential. To date most of the studies have been aimed at transplanting microencapsulated pancreatic islets to treat diabetes. There are several reasons for the focus on islet encapsulation: (i) diabetes is the leading cause of morbidity and mortality in the world;(ii) pancreatic islets, which comprise only 1-2% of the human pancreatic volume, can be isolated from animal sources; and (iii) the quantity of differentiated islet tissue to be transplanted is within a reasonable range (less than 1g).

Although promising progress in microencapsulation has been made by research groups around the world[4-8], the cell encapsulation technology has not lived up to the expectation of the wide range of potential applications. The challenges remaining include

chemical and mechanical strength of capsule membrane, permeability, transplanted cell's functional performance, biosafety, and long term survival of the graft [9, 10].

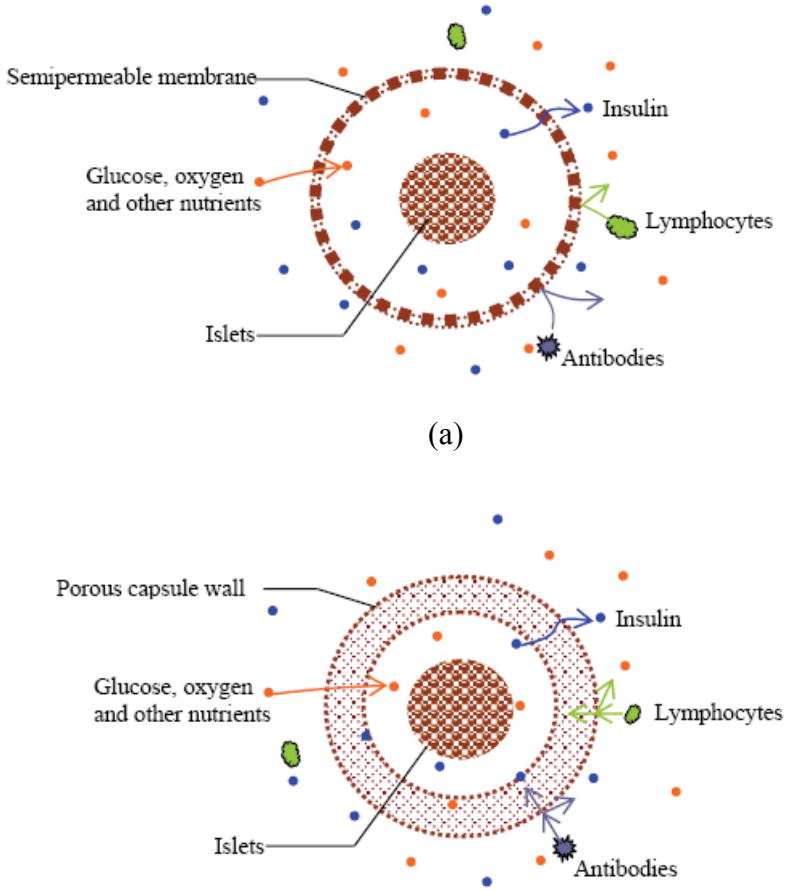

Figure 1.1. Sketch showing the mechanism of immuno-isolation provided by semi-permeable capsules: (a) gate-keeper model; (b) barrier model

Theoretical Background

Immuno-isolation: One primary advantage of cell encapsulation is that it maintains functional activity of the donor cells while protecting them from the host immune system attack. The basic mechanism for immuno-isolation is shown in figure 1.1. Ideally, the

capsule serves as a gatekeeper, which allows nutrition, oxygen and hormones to pass through without impedance and excludes immune system from entering. The effectiveness of immune isolation of a polymer capsule is closely tied to its membrane permeability, or the pore size distribution of the membrane.

It has been suggested that with proper selection of a cutoff pore size, the polymer membrane can block all the components of immune system (antibody cells), and allow the smaller molecular weight (MW) molecules, such as glucose, oxygen and hormones, to pass through without impedance. However, identifying the optimal pore size for capsule membrane has been a tough challenge in capsule design [11]. The permeability of a diffusing component depends not only on the pore size, but also on the size and shape of the solute molecules. The electrostatic/hydrophobic interactions between the membrane and the solute may also delay the diffusion. Another concern in modeling the permeability is the ability of some proteins to combine monomer units of polymers into larger associates (dimers, trimers). Considering the above issues, there is a need to understand molecular structure of each component of the immune system, and its functions in the immuno-response process.

The immune isolation model suggested by Wang and Lanza [12] introduces the concept of immune barrier instead of gate keeper. As the pore size of every polymeric membrane is not homogeneous by nature, but consists of a broad spectrum of sizes, the immune barrier model suggests that the capsule membrane may not completely block the immune particles, but rather significantly delay their contact with the enclosed cells. By assuming that the immune components pass through the membrane in a “random walk motion”, the immune isolation time, Γ, can be calculated qualitatively [12] according to:

$$\Gamma \approx 3\frac{d^2}{R^2} f\tau \tag{1.1}$$

where d is the membrane thickness, R is the average pore size, f is the ratio between surface areas of small pores and large pores, and τ is the time that the immune system is trapped by the small pores in each encounter. The value f can be determined quantitatively from the surface area distribution, and the value of τ for different immune systems can be estimated from the dextran size exclusion chromatography (SEC) retention time [13]. The calculated immuno-isolation time for a SA-PLL-SA capsule (110KDa pore size, 2μm wall thickness) is in the order of days, which is in agreement with experimental observations.

Mass Transport: To maintain the islets viability inside an immuno-protective capsule, the nutrients and oxygen must be allowed to diffuse freely in, and insulin be allowed to diffuse out. The mass transport across a random network structure is extremely complicated. Wang *et al.* [7] simplifies this diffusive process by expressing the mass transport flux, Q, across the membrane as

$$Q \approx \frac{R^4 T}{r\eta d}\Delta cN \tag{1.2}$$

where Δc is the mass concentration difference between the inside and outside of the membrane, N is the number of pores on capsule surface, r the particle radius, T the temperature and η the fluid viscosity.

Mechanical Strength: Once implanted, capsules may be subjected to severe physiological normal and shear stresses. In order to maintain a long term immuno-isolation for the

transplanted islets, the capsules must have strong mechanical strength to avoid breakage.

The small deformation of capsule, δr, under an unidirectional pressure P_x can be written as:

$$\frac{\delta r}{R_c} = \frac{R_c}{4Yd} P_x \tag{1.3}$$

where R_c is the capsule radius and Y is the Young's Modulus and d is the thickness of membrane.

Equation (1.1), (1.2), (1.3) provide a general estimation of capsule parameters and its functional behavior. It is seen that the mass transport requires dichotomal capsule parameters (bigger pore size, R, thinner membrane, d) as those for immune isolation (smaller pore size and thicker membrane). In order to achieve optimal performance, there is need for numerous experiments through which each parameter should be evaluated and selected independently.

Development of capsules

Among many biomaterials that can be used to for making semi-permeable capsules, alginate is the most promising one simply because it is a naturally occurring substance (seaweed), and thereby biocompatibility is probably assured. Alginates are straight-chain polysaccharides derived from seaweed with functional blocks of manuronic (M) and guluronic acid(G). In solution, alginate molecules behave like free flexible coils. However, upon interaction with divalent metal ions, such as Ca^{2+}, Ba^{2+}, the G blocks on the molecular chain are bonded with each other to form a well ordered network structure with porous properties. The Ca^{2+} fits into the molecular network like eggs in an egg box and when more Ca^{2+} is available, the complex will produce more packed gel. The

alginate network structure and strength after the gelling process strongly depends on the innate characteristics of alginates such as M/G composition, sequential structure, and molecular weight distribution.

To form spherical capsules, the alginate drops containing dispersed islets are extruded continuously from the tip of a needle and enter into a reactive gelling pool. Usually, the extrusion can be accomplished though air stripping [14, 15], electrostatic force [16] or centrifugal force[17]. By adjusting the external force amplitude and/or frequency, the alginate drop size can be well controlled. The spherical alginate droplets can also be prepared by emulsion method[18], or by breakup of co-flowing stream[19, 20].

Once the alginate drop contacts the cation solution, gelation proceeds and a bead is formed. The gelation of alginate is an instantaneous and irreversible process, which is governed by the relative rate of diffusion of binding cations into the gelling zone. In the case of only Ca^{2+} serving as binding media, the gelation process can be accurately modeled as diffusion limited reaction[21]. Due to the nature of this gelling process, the alginate gel network density is not homogeneous inside the bead. In fact, experiments[22, 23] have shown that the alginate concentration is higher at the outer surface than in the core area.

The simplest system for cell encapsulation may be an alginate-bead with cells inside. However, metabolic cation bonded alginate gels are too porous to provide suitable immune protection to the implant, especially in the context of xeno-transplantation. Also the calcium alginate bead is not stable in physiological environment. A way to improve this is to form an additional complex membrane with higher ionic density poly-anion(PA), like cellulose sulfate [6] and poly-cation, like poly-L-lysine (PLL, [6,14]) or

poly(methylene-co-guanidine) hydrochloride (PMCG, [6, 7]). The presence of additional membrane at the capsule surface can effectively reduce the cut-off molecular weight and increase the capsule's strength and stability. The drawback of adding the compact membrane is that it complicates the function of immuno-isolation and mechanical strength. It may also cause additional biocompatibility problems, probably owing to the high charge density arising from poly-cation residues. To minimize immune response, an outside coating of alginate is suggested and this has been proven to reduce the host's immune response and fibrotic growth on the membrane surface.

Recently in the cell encapsulation lab at Vanderbilt University, a systematic capsule evaluation process has been developed, which can evaluate capsule's mechanical property [6], permeability[13] and surface morphology[24]. It is also suggested that multi-component polyelectrolyte system has the flexibility of adjusting capsule's individual properties. Over a thousand combinations of poly-anions and poly-cations were tested to search for the polymer candidate that would be suitable for cell encapsulation. The combination of sodium alginate, cellulose sulfate, PMCG, calcium chloride, and sodium chloride appeared to be most promising[7]. In parallel, a novel chemical reactor [25] has been designed and developed to generate uniform capsules continuously and at a high rate of production. A schematic of this encapsulation system is shown in figure 1.2. In this method, anion drops are continuously sheared off a nozzle by the air stream. The drop size can be tailored by adjusting pumping pressure of anion solution and the coaxial air flow rate. Anion drop then falls into a funnel, which connects to a pipe composed of several circular loops. A steady flow of cation solution is pumped to circulate through the pipe from funnel to the exit of reactor. Individual capsules pass

through the reactor loop and then enter a buffer solution, which quenches the reaction. The loop is designed to prevent capsule sedimentation while reaction occurs in the pipe. One important advantage of this system is that it ensures that each capsule passing through the system has the same reaction time. Thus the membrane thickness is uniform within and between batches. The reaction time can also be controlled by adjusting the length of loops and cation solution pumping rate.

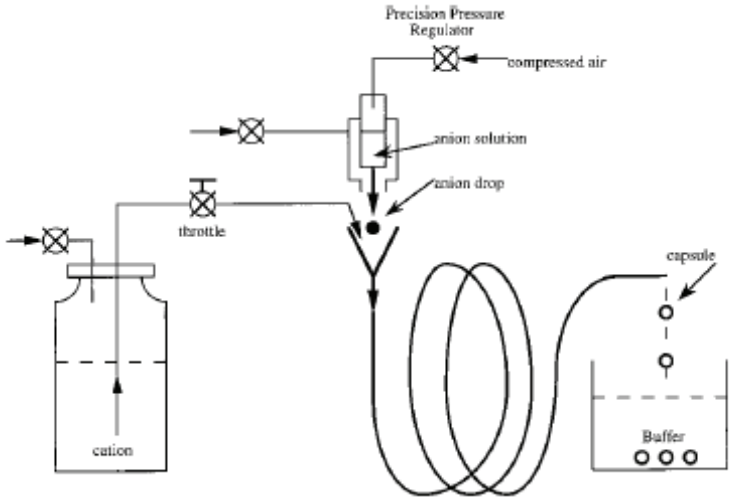

(a)

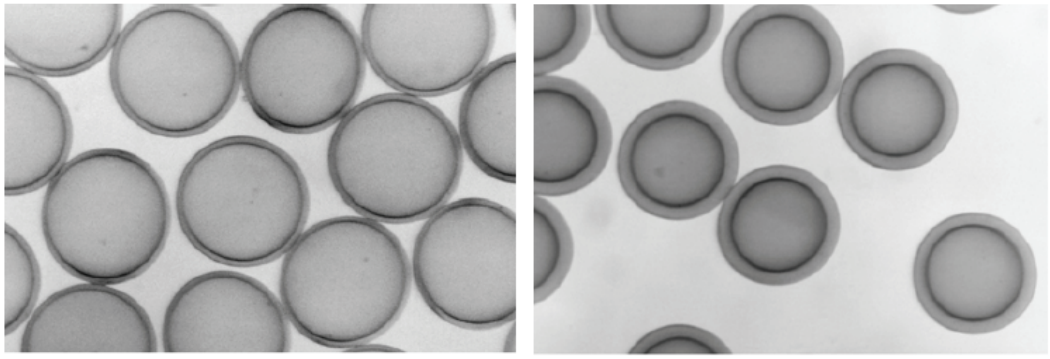

(b) (c)

Figure 1.2. (a) Encapsulation system designed for generating uniform capsules; (b, c) Capsules with uniform wall thickness produced with the multi-loop reactor, based on two different reaction times [25].

Biocompatibility issue

A biomaterial's biocompatibility is usually defined as the ability of the biomaterial to perform with an appropriate host response in a specific application[1]. In the context of islet transplantation using immuno-protective microcapsules, the biocompatibility can be interpreted as the capsule's ability to elicit no or minimal foreign body reaction, and maintain the long term viability and functional performance (insulin production) of donor islets as well. By this extended definition, almost all the failures of encapsulated islets transplantation, including the inadequate immuno-protection, can be viewed as insufficient biocompatibility, as summarized by G. C. Weir [26] (see figure 1.3). Therefore, biocompatibility is the critical issue in whether or not cell encapsulation technology can be widely implemented.

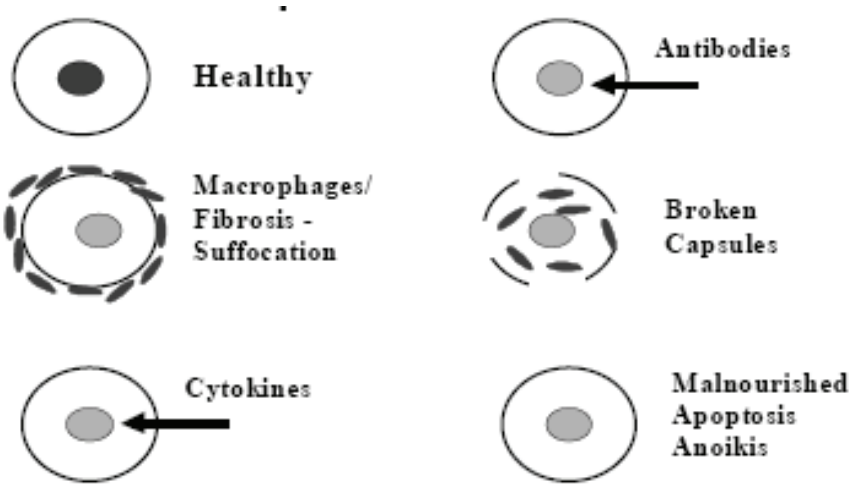

Figure 1.3. Possible reasons for encapsulation failure [26].

One of the major reasons for the failure of encapsulated islets is cellular overgrowth on the capsule surface. This overgrowth interferes with the free diffusion of nutrition and oxygen, and consequently causes the donor islet necrosis. In addition, the activated immune cells utilize nutrients and oxygen, further stiffening the local metabolic environment for encapsulated islets. The initiation of cellular overgrowth is related to the non-specific host response to the foreign material. De Vos *et al.* [27] show that the cellular overgrowth is composed of monocyte/macrophages, granulocytes, fibroblasts, erythrocytes, multinucleated giant cells and basophiles. Also they found that the overgrowth is in a time dependent fashion, rather than being steady. Known factors that may induce the cellular overgrowth include chemical component of the capsule [28-31], surface smoothness[27], breakdown of membrane[27], and the imperfections of encapsulation[27, 32, 33].

There are studies which suggest that encapsulated islets are also susceptible to the suppressions due to the inflammatory cytokines [28, 34, 35]. Cytokines play a key role in stimulating inflammatory cells such as macrophage and fibroblast. Cytokines such as interleukin-1 (IL-1β) and tumor necrosis factor α (TNF- α) are all proven β cell toxins. They can reduce the insulin secretion and cause damage to the encapsulated islets[34-36]. Therefore, it is important for the capsule membrane to be able to prevent the lower molecular weight cytokines from diffusing into the capsule. On the other hand, even though the cell-cell contact between host and graft is prevented by the capsule membrane, soluble antigens derived from grafts, whose MW is about 8-10 kDa, may still gain access to the host immune system, and cause T cell-dependent immune response toward transplanted islets [37, 38]. In this case, adjunct immuno-modulatory therapies may be

required to optimize the survival of encapsulated grafts. Another aspect of biocompatibility related to cell encapsulation comes from the graft's biological failure instead of immune failure. Biological failure can be viewed as the deterioration of viability and functionality of encapsulated islets even though the immune rejection is insignificant [1, 39, 40]. Several reasons can be contributed to this: (1) the pre-transplantation islets are not healthy, (2) the lack of direct vascularization of enclosed islets, (3) the exhaustion of the graft as a consequence of too high glycemic load on an insufficient volume of transplanted islets. Special attention should be paid to pre-translation islets manipulation, defining optimal encapsulation loading density and transplantation volume, and selecting transplantation site.

Some important works reported in the last few decades that focus on improving the biocompatibility and longevity of alginate microcapsules are summarized as follow:

Purity of Alginates: Commercially available alginates usually contain impurities which can induce host immune activities and thus contribute the failure of islets transplantation[1]. The use of highly purified alginate has been proved to be able to minimize physical imperfections in the generation of alginate microcapsules[41, 42]. The impurities contained in alginates may be classified into three kinds[43]: (1) contaminations during polymer synthetic process, such as monomers, catalysts, and initiators; (2) pyrogens and (3) mitogens. Among them, mitogen is most harmful impurity because it can activate many cell types including lymphocytes and fibroblasts and thus lead to the graft rejection. Contaminants like monomers, catalysts and initiators can be largely removed by dialysis, while the removal of pyrogens and mitogens is not simple. Zimmermann *et al.* [44] has shown that free flow electrophoresis method is able

to reduce the content of mitogens to an acceptable level. Klock *et al*. [45] and Prokop and Wang [43] suggest that multi-step chemical extraction can effectively remove both pyrogens and mitogens. The industrial provider FMC BioPolymer, based in Oslo, Norway, has developed a sterile, ultra-pure alginate powder, which is easy to dissolve and handle under sterile conditions.

Chemical component of capsules: Besides the impurity, the chemical composition of alginate itself, specifically the percentage of G-guluronic (G) acid in alginate macromolecules, has been proved to affect the biocompatibility of capsules. A review of recently reported experimental data suggests that low or intermediate G content appears to be more biocompatible[28, 29, 42] than high-G/low-M alginate. When PLL is used as a coating material to modify the surface of capsule, the PLL itself has been suggested as a major initiator of fibrosis[46, 47] and macrophage[30] growth, possibly because of the excessive positive charges on the PLL molecules. To neutralize the positive PLL sections, a final layer of poly anion is usually applied. Bunger *et al*. [48] has shown that the using polyacrylic as final outer coating induces much less immune response than alginate and heparin. A new promising method which can highly control alginate structure has been recently developed to improve the materials biocompatibility. This is done by using some specific enzymes, such as C-5 epimerases and AlgE4, to convert M acid to G or alternating M-G acid in alginate chain. With enzymaticaly tailored alginate used as outer coating material, the biocompatibility of alginate/PLL/alginate capsules shows a great improvement [49, 50].

Capsule size, shape and surface imperfections: As mentioned above, smaller microcapsules are preferred owing to their higher transport efficiency and mechanical strength. Results from animal experiments (implanted in rats) suggest the smaller capsules(diameters <700 micron) induce less cellular attachment, less capsule breakage and higher retrieval rate than regular microcapsules (diameters > 1 mm)[4, 51]. However, although smaller capsules are preferred, the capsule size must also be restricted to be above a lower limit. This lower limit on one hand comes from the technical difficulties of making extremely small capsules. On the other hand, capsule size must be big enough to ensure that the capsule fully encloses the islet. If the capsule diameter is too small, then the islets (diameters range from 50 to 250 μm) will more likely protrude from capsule membrane and induce severe immune response. The phenomenon of islets protrusion was first studied by De Vos and his colleagues[32, 33], and has been termed as *inadequate encapsulation*. They reported that capsules with 800 μm diameter were associated with the lowest rate of inadequate encapsulation when compared with 500, 600 and 1800 μm capsules.

In cell encapsulation, many research groups have identified the need for making smooth and perfect spherical capsules. Physical imperfections on capsule surface, such as membrane breakage, islets protrusion, polymorphic shape, local micro-artifacts (tails, craters), are considered capable of inducing more foreign body reactions [9, 27, 32, 33, 42, 52]. The other morphological factor relating to the biocompatibility is the overall smoothness of the capsule surface. The surface smoothness is important due to the following reasons: (1) the biomaterials with smooth surface are found to be able to induce less cell adhesion than the those with wrinkles and micro-artifacts (tails, craters) [9, 24,

48, 53-56]; (2) rough surface or local artifacts represent potentially weaker loci of the membrane and thus make the capsule more susceptible to physiological stress[24].

There are some studies in the literature focusing on improving the capsule's surface morphology. Goosen *et al.* [41] pointed out that the alginate viscosity must be higher than 30 cp in order to make spherical capsules. De Vos *et al.*[32] reported that the percentage of imperfect capsules with islets protrusion can be reduced by employing the optimal capsule diameter. Lacik *et al.* [55] proposed a two step encapsulation system to reduce the capsule surface wrinkles, which takes advantage of Na^{+}'s anti gelling effect [24], while maintaining the membrane's mechanical strength. Bunger *et al*. [48] successfully improved the surface smoothness and biocompatibility by coating alginate/PLL with polyacrylic, as compared to alginate and heparin coating.

The proposed study is directed toward improving the capsule's physical/ morphological quality. As will be shown later in this study, most physical imperfections originate from the encapsulation/drop impact process, and can be suppressed by carefully selecting the operation window.

Co-encapsulation of drugs and Sertoli cells: As a partial effort to enhance the functionality and longevity of transplanted islets, co-encapsulation of drug conjugated polymers has been suggested by some groups. For example, Yiu Han Bae and his colleagues revealed that the co-encapsulation of cross linked hemoglobin (Hb-C) with islets in alginate poly-L-lysine alginate capsules promotes graft functions for a longer period of time than the conventional islets capsules[57]. This is because the Hb-C can facilitate oxygen supply and protect the islets from oxidative stress. Another conjugate

water-soluble sulfonylurea/pullulan (SUP) is found be able to boost the insulinotropic activity and islets viability[58]. Sertoli cells can secrete immunosuppressive factors and protect themselves as well as islets from immune rejection[59]. It is reported that the co-encapsulation of sertoli cells with islets can also provide long-term immune protection for both allograft [60] and xeno-graft [61].

Fluidic and chemical processes in encapsulation

Although numerous concerns have been addressed in optimizing the physical and chemical properties of the microcapsules used for cell encapsulation, the basic understanding of the fluid and chemical dynamics involved in the capsule formation process is still lacking. Recently, it has been noted in our lab that entrapped air bubbles following drop impact pose a new problem in the cell encapsulation process. The capsules are made by continuously dispensing viscous poly-anion drops into water-like poly-cation solution [25], where the membrane-forming chemical reaction proceeds as the drop contacts the reactive bulk during impact. At that time, a single air bubble often embeds on the drop surface, locally impeding the chemical reaction and membrane formation (figure 1.4.a). The presence of such an air bubble adversely affects the capsule surface quality and makes the capsule vulnerable to immune attack (figure 1.4.b). This problem has stimulated our current study of drop impact and the associated problems. The mechanism of bubble entrapment in the context of capsule formation will be a major focus of this study.

Figure 1.5 shows a schematic representation of the processes taking place in the drop-dispenser-based encapsulation process. The whole procedure starts with the

separation of a liquid poly-anion drop from the nozzle tip. Before hitting the pool-air surface, the liquid drop restores into an overall spherical shape during the free fall through air, owing to the air drop surface tension. Once the drop impacts onto the pool surface, the kinetic energy of the drop is transferred into the potential energy of the liquid system, through the following two processes: (i) the formation of impacting crater (the air void beneath the pool surface), and (ii) the deformation (flattening) of the drop liquid. The problem of a water drop impact on the air-water interface has been well studied in the literature, and will be reviewed in the next section of this chapter. However, the poly-anion and cation complexation process proceeds as soon as the drop liquid contacts the pool. This complexation complicates the drop impact problem by effectively changing the drop/complex properties and the interfacial dynamics. One possibility is that the complexation occurs so fast that it freezes the drop liquid before it can restore to spherical shape, then the final capsule shape will be irregular. The other extreme case is that if the complexation rate is very slow, then the capsule shape is more determined by the surrounding convective flow, and a non- spherical capsule shape may still be observed. The ideal scenario would be for gelling reactions to occur on a spherically rounded drop shape. To achieve this, one must carefully select the kinetic impacting condition of the anion drop, and the concentration of the reaction systems.

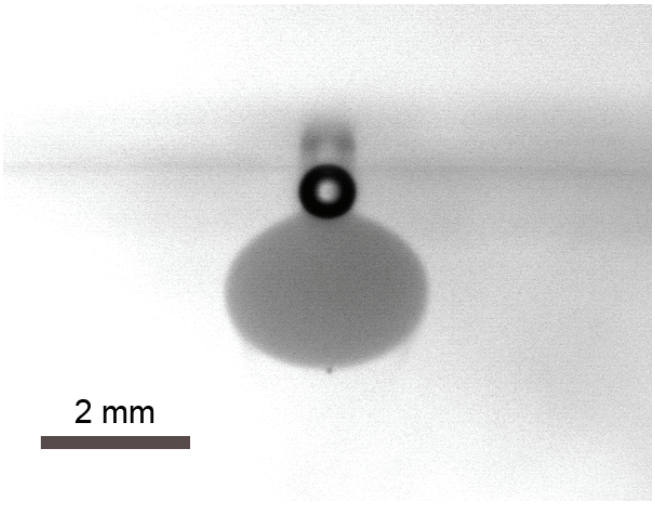

(a)

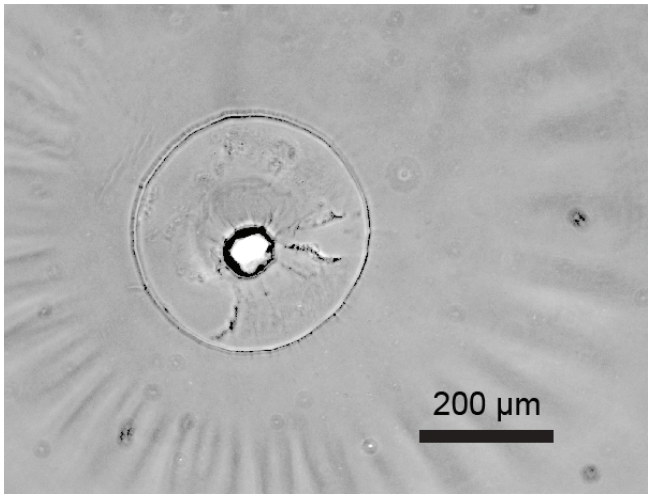

(b)

Figure 1.4. Bubble entrapment observed during the encapsulation process: (a) entrapped air bubble embeds on the drop/capsule surface, impeding chemical reaction locally; (b) enlarged picture showing surface defects due to the presence, and eventual rupture, of the air bubble.

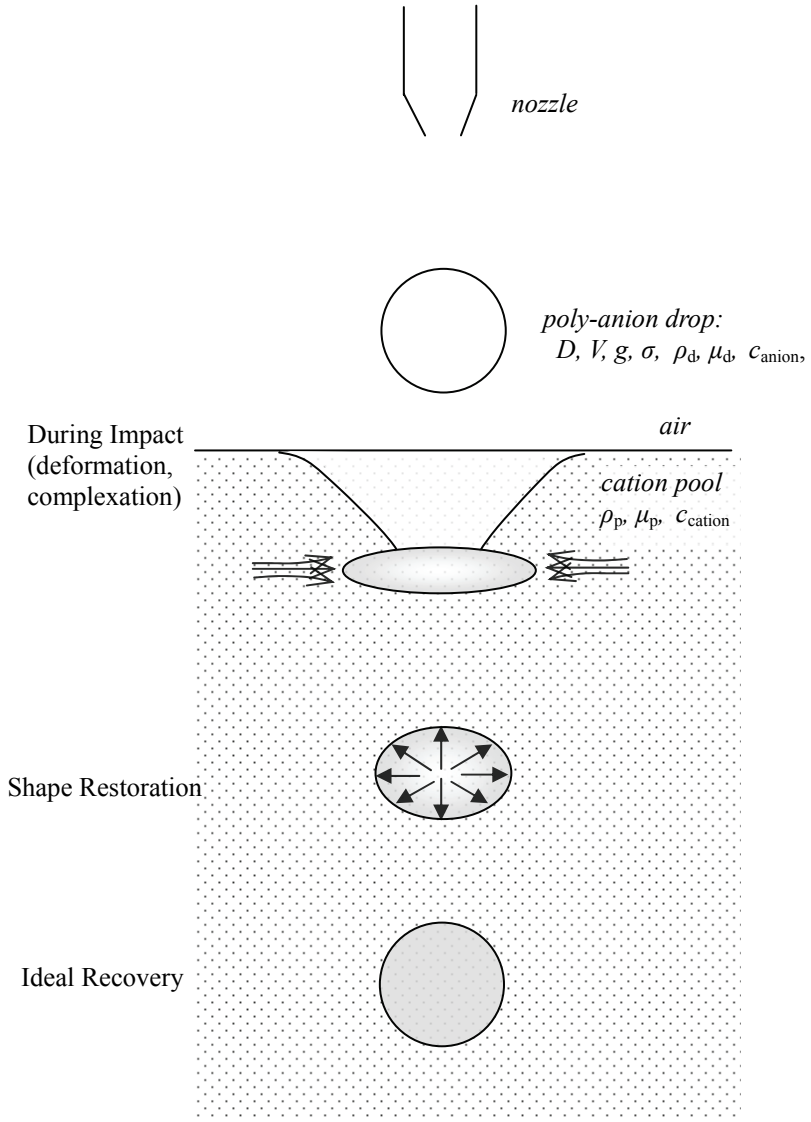

Figure 1.5. Schematic representation of the processes taking place in the capsule formation process.

Drop impact onto liquid/air interface

The phenomenon of a water drop impact onto the surface of a water pool, a very familiar scene seen in nature during a rainfall, has been studied for nearly a century. While initial studies were motivated purely by scientific curiosity, the more recent studies have been prompted by the practical application of this phenomenon. For example, the vortex ring developed after low energy drop impact can enhance the mixing of drop fluid with pool fluid [62]. The underwater noise during raindrop impact on water surface is caused by the oscillation of small air bubbles, repeatedly entrapped at the bottom of the impacting crater under certain conditions [63]. The air entrapment increases gas transport between the atmosphere and the ocean, and provides boiling nucleates for bulk fluid [64].

The physical forces involved in drop impact are surface tension, inertia of the impacting drop, viscous force and gravity. Hence three dimensionless parameters are applied in describing this process: Froude *Fr*, Weber *We* and Reynolds *Re* number, which are defined by:

$$Fr = V^2 / (g*D), \qquad We = (\rho*D*V^2) / \sigma, \qquad Re = (D*V) / \nu \tag{1.4}$$

Here V is the impacting velocity, D the drop diameter, σ the surface tension coefficient, ν the kinematic viscosity, ρ the liquid density and g the acceleration of gravity. Viscous effects have been neglected in most previous works ($Re \gg 1$), but they will be a major focus of this study.

Within different ranges of impacting conditions, several types of phenomenon have been studied following the drop impact onto liquid surface, including: drop floating, bouncing, vortex ring, jetting (thick and thin), bubble entrapment, and splashing. A complete plot that delineates regimes for each impacting signature in the *We-Fr* plane is

provided by [65], also as seen in figure 1.6. Among these various phenomena, vortex ring and bubble entrapment are most frequently studied in recent publications. These two phenomena occur in the same range of kinetic conditions as in our encapsulation problem. In the following review, a summary of significant progresses reported in the literature about vortex ring and bubble entrapment will be presented. Later, some theoretical and numerical approaches that have been employed in interpretation of drop impact phenomena will be discussed.

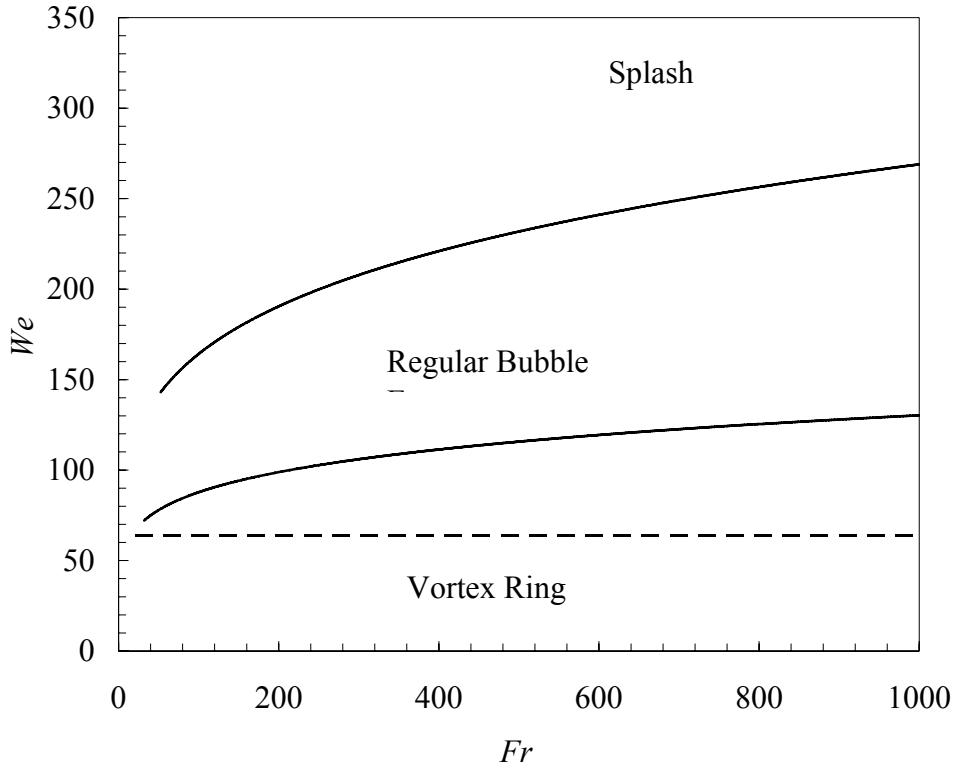

Figure 1.6. Regimes in *We-Fr* plane for different phenomenon observed during a drop impact onto a pool of the same liquid.

Low or zero velocity impact: vortex ring

When a liquid drop contacts a liquid surface with zero or low velocity, a vortex ring is observed penetrating downward from the free surface. In the literature, this type of impact is also called coalescence. One typical photograph of this phenomenon is shown in figure 1.7 [62]. The procedure of coalescence can be described as follows. As a drop approaches a surface at near-zero velocity, an air film exists between two surfaces, which can be evidenced by the common phenomenon of drops floating on the surface. This floating condition is usually a transient one, except for the case when Marangoni effect is involved or the system is kept oscillating at certain conditions[66]. The air film is drained out while the drop is continuously falling. Finally the two liquids from the drop and pool contact, and the excess surface energy from drop drives the drop liquid downward rapidly into the pool, forming toroidal vortex ring which travels down as revealed by dyed drop liquid in figure 1.7. Hsiao *et al*. [71] give a critical value *We* about 64 for the impacting drop, below which the vortex ring can be seen to form upon the impact.

The source of vorticity for the vortex ring formation must be related to the viscous stress on free surface as the surface is disturbed by the coalescence. Cresswell and Morton [67] suggests that the formation of vortex ring requires the development and separation of a boundary layer during the initial stage of coalescence process. Picture from Dooley *et al.* [68] clearly shows that the pool liquid rolls up and surrounds the drop liquid very quickly within first one or two milliseconds of the coalescence process. This surface parallel acceleration generates positive vorticity flux into the drop liquid, which could be the vorticity source of the later developed vortex ring.

Some scaling analyses have been developed for understanding the mechanism and

properties of this vortex ring. The surface tension-dominated time scale [69] is :

$$\tau_1 = (\rho D^3/\sigma)^{1/2}, \tag{1.5}$$

and the convective time scale:

$$\tau_2 = D/U \tag{1.6}$$

One could expect that the dominant force during the ring formation is surface tension, while the viscosity and gravity can be neglected, so the ring formation time τ^* is proportional to τ_1, which gives

$$\tau^* \sim D^{3/2}\, \sigma^{-1/2} \tag{1.7}$$

If convective time scale τ_2 is much larger than surface tension time scale τ_1, the inertial force term becomes dominant and there is not enough time to develop the vortex ring. Then a totally different event is observed at higher *We* impact as will be discussed next in this section.

Dooley *et al.* [68] developed an experimental system which can precisely measure the ring formation time τ^*. Their result proved the that relationship between drop size, surface tension and ring formation time agree well with equation 1.7.

Another scaling analysis on vortex ring is made by Anilkumar *et al.* [62], where they derived a power law relationship of penetration depth, drop size and viscosity by equating the surface tension energy to the energy dissipation from the viscous effect.

Some studies have pointed that in the case of small velocity impact, the penetration depth of vortex ring following the impact varies with the drop shape at the time of contact. Usually a free falling drop oscillates due to the surface tension effect. The oscillation frequency for the primary mode is:

$$f = 1/\pi\, (2\sigma/\rho R^3)^{1/2} \tag{1.8}$$

where R is the impacting drop radius. Chapman and Crichlow [70] performed a photographic study to explore the relationship between drop shape and maximum vortex penetration depth. They found that the vortices that penetrate deepest are formed from a spherical drop in the phase of oscillation where the drop is transitioning from an oblate drop to a prolate drop. Conversely, when the drop is spherical and transforming from oblate to prolate, the penetration depth is minimum. Rodriguez and Mesler [71] found that the most penetrating vortex is observed when the drop is prolate in shape as it contacts the pool surface, while the least penetrating vortices occurred when the drop is oblate.

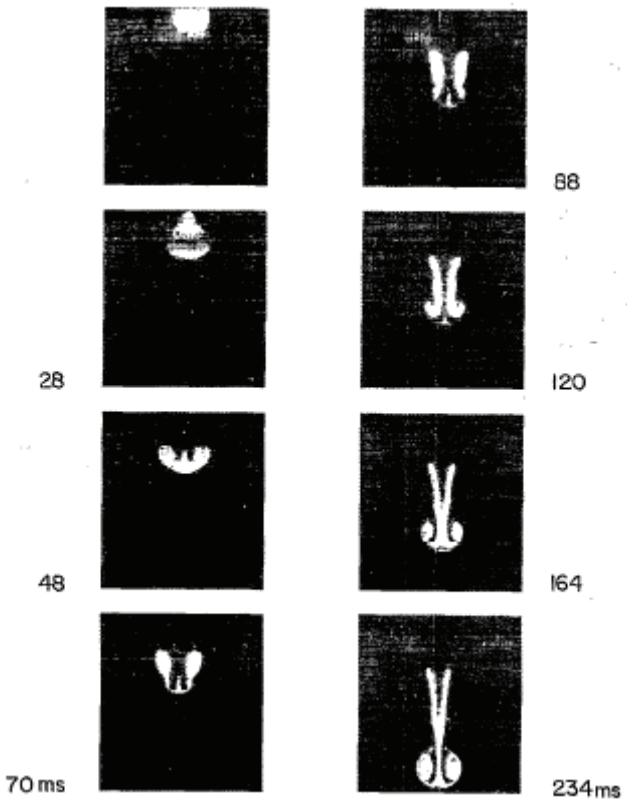

Figure 1.7. LIF picture showing vortex ring formation following drop coalescence into a deep pool, from [62].

Regular bubble entrapment in drop impact

According to the experimental work of Hsiao *et al.* [69], when the *We* number for falling drop is above the critical value (*We* ~ 64), the vortex ring structure is suppressed, instead, new phenomenon are observed, including regular bubble entrapment, upward moving central jet (either thin or thick), and crown formation.

Regular bubble entrapment during drop impact has been well studied in the past two decades. The so called regular bubble entrapment/entrainment indicates that this specific bubble entrapment event is repeatable under particular impact kinetic conditions. Figure 8 lists a series of pictures representing typical interface(crater) evolvement when regular bubble entrapment occurs following a 2.13 mm water drop impact onto a deep water pool [65].

From photographical investigation on regular bubble entrapment, the following conclusions can be drawn: (a) regular bubble entrapment occurs at the bottom of impacting crater, when the crater represents a critical cone shape; (b) the bubble entrapment observation is reproducible when the drop strikes the water at a speed between certain upper and lower impact velocity limits; (c) bubble entrapment is always accompanied by the ejection of a high speed thin jet from the crater center. This phenomenon has been studied in detail by Rein (1996) [72], in which he determined that the parametric limits for high-rising thin jet actually encompass the regular entrapment limits, and (d) the dependence on surface tension is noticeable, e.g. the regular bubble entrapment disappears when the surface tension is lowered from 74 dyn/cm to 30 dyn/cm [73].

Many studies have focused on the mechanism of regular bubble entrapment.

Pumphrey and Elmore [73] experimentally studied regular bubble entrapment in a wide kinetic range. They found that regular bubble entrapment occurs in a well-defined region in the *We-Fr* plane. The lower and upper region are represented by a power law relationship of the type $We \sim Fr^{0.179}$ and $We \sim Fr^{0.248}$ respectively. Oguz and Prospereitti [74] stated that "whether a bubble is entrapped or not is determined by a delicate balance between the times at which the outward motion of the crater wall is reversed at different positions". Based on the observations of Pumphrey's experimental results [73], they further proposed two scaling models showing that the lower and upper limits for bubble entrapment are $We \sim Fr^{1/5}$ and $We \sim Fr^{1/4}$ respectively, which agree well with the experimental data. In their analysis, they did not mention the traveling capillary ripple along the crater wall, as observed by Pumphrey & Elmore [73]. Later studies, however, have addressed the role of the traveling capillary wave in regular bubble entrapment [73, 75-77].

It has been observed that the impact crater resembles an inverted cone shape prior to bubble entrapment. Longuet-Higgins [78, 79] first proposed a general velocity potential model, neglecting gravity and surface tension effects, leading to a solution with a hyperboloid free surface, which fairly well represents the conical crater shape before bubble pinch-off. More interestingly, he found that there exists a critical cone angle of 109.5^{o}, at which the flow field diverges. This critical cone angle compares well with the numerical results of Oguz & Prosperetti [74] and the experimental results of Leng [65], however, it is not clear as to why the bubble entrapment event occurs at this point.

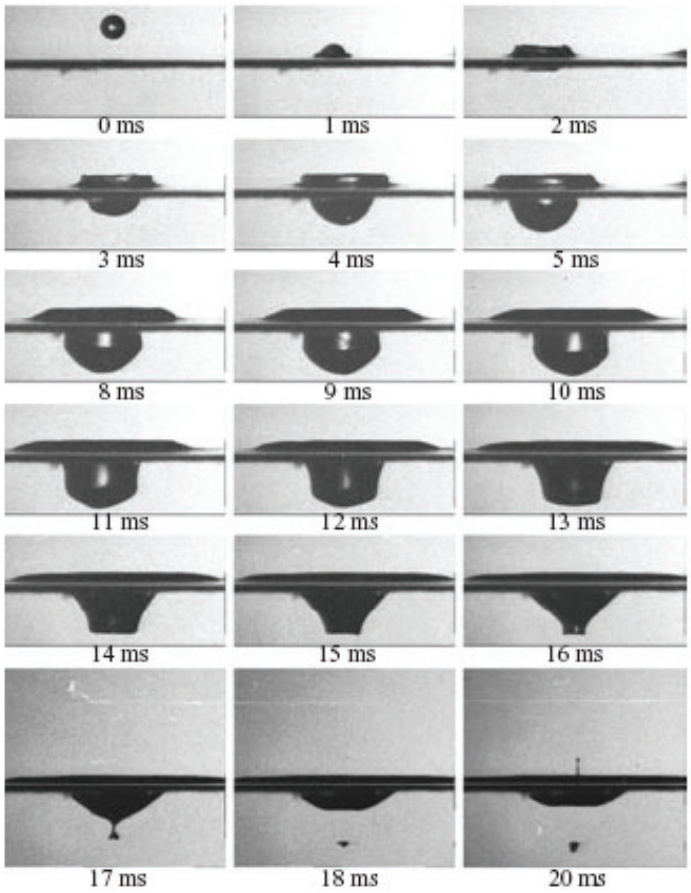

Figure 1.8. A series of pictures showing the impacting crater deformation and regular bubble entrapment[65].

Rein [72] carried out a series of experiments using 2.3 mm water drops to investigate the transitional regime between coalescence and splashing. He pointed out that drop impact in the region of regular bubble entrapment is always accompanied with the ejection of a high-rising thin liquid jet originating from the center of the impact crater. He attributed this phenomenon to the occurrence of a high pressure stagnation region during crater collapse. More recent studies have shown high-speed thin jet formation in other hydrodynamic situations like surface wave collapse [80, 81] and collapse of surface voids [82, 83]. In these contexts, the jet formation is driven by the inertial focusing of the bulk flow during the collapse. To demonstrate this focusing effect, the surface

geometries prior to collapse have been scaled as power law dependence with time[82, 84-86]. A similar scaling approach in the drop impact problem could draw attention to the bulk flow focusing effects on bubble entrapment and thin jet formation.

Impact with higher *We*: Splash

In the regime above the regular bubble entrapment limit, the crater bottom reverses its moving direction before it can pinch off an air bubble. A thick jet is observed rising from the center of the crater and may or may not jet off a drop from tip, depending on the magnitude of the impacting kinetic energy [87]. At even higher impacting kinetic energy, the edge of crater wall ejects a sheet of liquid upward. The liquid sheet is unstable due to capillary effect and always ejects off tiny droplets from its upper rim, which forms the well-known crown pattern[88]. This is probably the earliest reported signature of drop impact in literature. Generally, the phenomenon of crown formation and central jet shedding of daughter droplets is termed as splash, which means some liquid mass separates from the main body. As the impacting energy is further increased, the crown sheet will enclose above the crater bottom, which leaves a bigger air pocket entrained and leads to a upward and downward liquid jet originating from the enclosure point[89]. This air entrainment should be differentiated from bubble entrapment, and it is beyond the scope of present study.

Miscellaneous bubble entrapments

In addition to regular bubble entrapment as discussed above, several smaller bubble entrapment mechanisms have been reported sporadically [73, 90]. The length scales for

these bubbles are from a few microns to less than a hundred microns. Usually they are entrapped right after the impacting drop contacts with the bulk and before the crater is formed. Experiments show that these miscellaneous entrapments are unrepeatable events and are very sensitive to surface tension, and occur within a wider parametric range than regular entrapment, including both low and high impacting velocity. Due to the nearly indiscernible size and unpredictable formation mechanism, it is difficult to photograph and hence thoroughly study these bubble entrapment events. Recently, with the aid of extremely high-speed digital video camera, combined with long-distance microscope, Thoroddsen [64] has been able to investigate the minute bubble entrapment at early stage of impact in detail. From the photos, they discovered that an air sheet is entrapped first when impacting drop contacts with bulk surface. The air sheet then rapidly contracts into a vertical column of air pocket, which may split into two bubbles. During the contraction of the air sheet, a necklace shape was observed along the air sheet edge due to azimuthal capillary instability. Their experiments also suggested that the thickness of the air disk almost linearly decreases as increasing impacting velocity, while the volume of the entrapped bubble is related to the bottom shape of impacting drop.

Another possible mechanism that may cause small bubble entrapment is the so called Oguz-Prosperitti ring, which was first proposed by Oguz and Prosperitti [91] based on their numerical simulation. Their description of this bubble entrapment can be simplified as follows. As the drop continuously falls down to the pool surface, after the initial contact, the contact area of drop and bulk surface spreads in horizontal direction. Meanwhile, a capillary wave is formed on both the drop and the bulk surface and travels outward. The wave crests on the drop and on the pool surface can meet thereby trapping a

very thin toroidal bubble. This is very unstable and rapidly breaks into a ring of tiny spherical bubbles. The process may be repeated several times giving several concentric bubble rings. However, little direct evidence exists to justify this mechanism in the literature. Figure 7(a) from [64] appears to be the closest one, where one clear ring of 110 and 65 bubbles respectively, about 25 μm in diameter, is shown.

In addition, the secondary drops generated from upward jet and crown edges, as well as ejecta sheet may also contribute to numerous miscellaneous entrapments occurring under different impacting parameters. This phenomenon can only be studied in detail using extremely high-speed video photography.

Theoretical considerations on crater dynamics

The formation of impacting crater is a dynamic process where the kinetic energy stored in the impacting drop is transformed into the kinetic and potential energy of the receiving pool. Most analytical methods consider the flow to be inviscid, so that the viscous dissipation is neglected and the flow field during the impact can be simplified as potential flow. This is justified because the convective time scale, D/V, is usually of the order of a few milliseconds, while the viscous timescale, $\rho D^2/\mu$, is of the order of hundreds of milliseconds for water system. Further, gravity affects the geometry of crater in a time scale of $(2D/g)^{1/2}$, which is in few tens of milliseconds. According to this time scale analysis, it is seen that in the first few (ten) milliseconds, it is the inertial force that drives crater growth. During the time of crater growth, gravity does not affect the crater morphology, so the growth should be hemi-spherical, which is proved by experimental observations. In the next few tens of milliseconds, gravity starts to deform the crater and

finally the crater interface recovers to the equilibrium, horizontal flat surface. In the same time frame, capillary ripples generated at the impact crater edge travel down the crater and viscosity works to damp out the wave motion.

In modeling the crater growth, Leng [67] used an approach similar to Engel [89, 92], by assuming that the impacting drop provides a potential energy source to the receiving pool fluid. His model gives a flow field identical to the one observed during crater growth, which has only radial velocity and the velocity is constant along the spherical surface. It is argued that if Froude number (*Fr*) is large, then the kinetic energy of the mean flow driven by the expanding cavity does not change substantially during the early stages of crater formation. By further neglecting both the gravity and surface tension potential, the energy conservation analysis gives [65]:

$$t \sim R^{5/2}, \quad t_m \sim R_m^{5/2}, \tag{1.9}$$

where t is time and R is the crater depth, t_{m} is the time for the crater to reach maximum depth R_{m}.

The maximum crater depth, R_{m} will be reached when all the kinetic energy is converted to the crater's potential energy. R_{m} can be evaluated by a simple model, which equates the kinetic energy of the impacting drop, $1/12\pi\rho D^3 V_i^2$ to the gravity potential energy arising due to the crater, which can be expressed as $1/4\rho g R_m^4$. Then the maximum crater depth, R_{m} can be scaled as:

$$\frac{R_m}{D} = 0.76 Fr^{\frac{1}{4}} \tag{1.10}$$

Experimental results suggest that the power law scale of 1/4 is valid for a high *Fr*. However, the R_{m} by equation 10 is overestimated since this equation dose not count the

surface energy on the newly formed surface and the potential and kinetic energy of the swelling wave. Surprisingly, Leng's result shows that only 28% of the impacting drop kinetic energy is converted to the crater gravity potential energy[65].

A more thorough semi-empirical model for the crater formation is provided by Engel[89, 92], where surface tension energy increase due to the crater formation and the viscous dissipation term are included. This model is applicable when the impacting kinetic energy is very high.

In order to capture the conical feature of the impacting crater, Longuett-Higgins[78, 79] proposed another velocity potential model as:

$$\Phi = \frac{1}{2} A(t)(2z^2 - x^2 - y^2) \tag{1.11}$$

Then the velocity vector:

$$\nabla\Phi = A(-x,-y,2z) \tag{1.12}$$

depends linearly on x, y, z, which indicates that any material particles lying in a straight line will remain in a straight line after Δt. Thus, if the free surface is a cone, it always remains a cone shape except that the vertex cone angle 2γ depends on time.

The time dependence term of A is:

$$A(t) = \frac{\dot{\lambda}}{2\lambda} \tag{1.13}$$

where $\boldsymbol{\lambda}$ is given in terms of time t by the elliptic integral:

$$\frac{t}{t_0} = \pm\int_1^{\lambda} (1 - \lambda^{-3})^{1/2}\, d\lambda \tag{1.14}$$

$\boldsymbol{t_0}$ being an arbitrary constant.

It is derived that the free surface ($p=0$) is a cone with semi-vertex angle:

$$\gamma = \arctan(2/\lambda^3)^{\frac{1}{2}} \tag{1.15}$$

At t=0, with corresponding λ=1, the entire velocity field at the cone tip is found to become infinity as

$$v = |t|^{-\frac{1}{3}} \tag{1.16}$$

and acceleration:

$$\dot{v} = |t|^{-\frac{4}{3}} \tag{1.17}$$

At the moment t=0, the cone angle has a critical value of:

$$\gamma_c = 2\arctan(2)^{\frac{1}{2}} = 109.47^\circ \tag{1.18}$$

This implies that whenever the free surface flow represents a cone shape with this vertex value, the entire flow field must have a singularity in time.

It is also noted that as time approaches to t=0, the cone angle varies in a fashion predicted as:

$$\Delta\gamma = (\arctan 2^{\frac{1}{2}} - \gamma) \sim t^{\frac{2}{3}} \tag{1.19}$$

The critical value of 109.5^o and the relationship of equation 1.19 agree well with both numerical [78] and experimental [65] results, where impacting craters due to water drop impact are examined in detail. However, in this potential flow model, the effects of viscosity, surface tension, and gravity are not included. It is also not clear as to why bubble entrapment, which is the local phenomenon, should coincide with the observation of the critical cone angle.

Numerical Methods

Solving full Navier-Stokes equations in the presence of deforming interface, as in the case of drop impact, is complicated. However, many efforts have been made in tackling this problem via different numerical approaches. The oldest but still most popular approach to compute free surface flow problem is the boundary integral method (BIM). BIM is preferred when only the interface configuration is concerned and the flow must be potential, which means the viscous effect is neglected. For example, Lee *et al.* [93] used this method to calculate the steady shape of acoustically levitated drop. Oguz and Prosperetti [91] simulated the liquid-air interface at the early stage of two liquid body contact, and provided insightful details of the interface, that has never been observed experimentally. Later, they incorporated new time stepping and curvature damping methods and successfully captured bubble entrapment signature of the impacting crater [74].

The second family of numerical methods is to capture the interface directly on a regular stationary Euler grid. In this class, marker and cell (MAC) method, where marker particles are advected at the interface, and the volume of fluid (VOF) method, where a specific marker function is advected, are best known examples. A recent application of this method can be found in Morton *et al.* [76], who simulated the drop impact problem under conditions encompassing the regular bubble entrapment regime. A significant progress made in their work is that the viscous term is included in the Navier-Stokes equation. As a result, the formation of vortex ring and the vorticity distribution pattern under the crater surface can be revealed from the numerical results. In addition, the authors used a fractional fluid volume function to account for complex fluid interface

topology, which enables the simulation to reproduce the bubble after it is pinched off from crater. The bubble can not be tracked in Oguz and Prosperetti's BIM method, since the simulation must stop at the entrapment moment. Some other applications of similar methods include the study of the drop splashing on a liquid film[94], and the drop impact on an orifice plate[95]. The classical difficulties in this Eulerian based simulation involve maintaining sharp interfaces and computing the surface tension.

Recently, a novel improved front tracking method has been developed by Tryggvason and his colleagues [96]. In this method, the unsteady Navier-Stokes equations are solved on a fixed structured grid, and the interface, or front, is tracked explicitly by a separate set of grid points (marker) of lower dimension. The advection of fluid properties such as density and viscosity can be done by following the motion of the front. This method has been implemented in studying various types of classical free surface flow problems, such as drop collisions[97] and bubbly flow[98, 99]. It is also shown to be capable of simulating more complicated free surface problems which involve dynamic surface tension and phase change[100-102]. With this consideration, front tracking method perhaps is the most promising in studying encapsulation process, where surface membrane formation proceeds during interface deformation.

Scope of the present study

Although significant progresses have been made in the last few decades, the long term biocompatibility and viability of microcapsules remain a challenge. Many evidences have shown that physical imperfection of microcapsules may decrease capsule's bio compatibility and thereby lead to unsuccessful cell transplant treatment. One ready

technical concern in encapsulation is to make uniform microcapsules with very smooth surface. In order to achieve the optimal morphological quality of microcapsules, further understanding of the fluidic and polymeric dynamics during the encapsulation is needed.

The encapsulation method used today involves two complicated concurrent processes: viscous liquid drop impact onto inviscid liquid pool and interfacial chemical reaction. The drop impact problem has been well studied for many years. However, almost all previous works are limited to inviscid drop impacting onto same liquid pool. The role of viscosity and surface tension on regular bubble entrapment, and related surface flow phenomenon, are not completely understood. The current study of drop impact with varied fluid properties provides a significant addition to the literature in this field.

In encapsulation, the final morphology of the microcapsule is determined by the complicated interaction of interface deformation and front gelation. This study attempts to correlate the physical imperfections of microcapsules to the dynamics involved in the reactive (gelation) drop impact, by carrying out photographic studies within a wide parameter space. Results of this proposed research can serve as a guide in optimizing the encapsulation process. The study of front reactive liquid drop impact is also of special interest to metallurgical processes, surface coating, quenching, and any other material process applications associated with material phase change. The experimental data may provide fundamental bases for modeling and simulating the reactive drop impact phenomenon in the future.

CHAPTER II

MATERIALS AND METHODS

Materials

For the simple liquid drop impact experiments, as discussed in chapter III, three sets of liquids were used: distilled water, glycerin/water mixture and silicon oil (Dow Corning Fluid 200). The properties of silicon oil are available through manufacturer's data sheet. Different concentrations of glycerin/water mixtures were made by mixing distilled water and pure glycerin (Fisher Scientific) in appropriate weight ratios. The viscosities of these mixtures were measured by a falling ball type viscometer. The surface tension was measured through a ring type tensiometer (Fisher Surface Tensionmat, Model 21). Table 2.1 lists the typical properties of the liquids used in this study. In some cases, a small amount (less than 0.5% in weight) of dye was added to the drop liquid in order to highlight the drop liquid during impact. The dye added to silicon oil was oil orange powder (DuPont), and red food color (McCormick) was used for glycerin/water mixture. The addition of dye to the test fluids had negligible effects on their physical properties.

In encapsulation experiments, the poly-anion (PA) solution was made by dissolving medium viscosity sodium alginate, MVG (FMC BioPolymer) and cellulose sulfate (Acros Organics) in phosphate buffered saline (PBS, Baxter Labs). The typical concentration of MVG/CS was 0.8/0.8 wt % for poly-anion solution, with the viscosity measured as 171 cp. The viscosity decreases as the chemical concentration of the poly-anion solution is lowered. The viscosity of 0.6/0.6 wt % MVG/CS was measured as 59 cp

Table 2.1. Properties of simple liquids used in the experiments (* measured data; # manufacturer's data).

	Density (10^3 kg/m^3)	Surface tension (dyne / cm)	Viscosity (cp)
* Distilled water	0.998	73.6	1
# 1 cs silicon oil	0.818	17.4	0.82
# 2 cs silicon oil	0.878	18.9	1.76
# 5 cs silicon oil	0.909	19.7	4.55
* 50 w% glycerin/water	1.126	69.2	5.9
* 60 w% glycerin/water	1.153	67.2	10.2
* 67 w% glycerin/water	1.172	63.9	14.7
* 85 w% glycerin/water	1.221	63.0	90.0

Table 2.2. Measured properties of chemical solutions used in the experiments.

	Density (10^3 kg/m^3)	Surface tension (dyne / cm)	Viscosity (cp)
Poly-anion I (0.8/0.8 wt % MVG/CS)	1.013	73.0	171.0
Poly-anion II (0.6/0.6 wt % MVG/CS)	1.010	72.5	59.1
Poly-anion III (0.4/0.4 wt % MVG/CS)	1.006	73.6	19.5
Cation solution (0.76/0.9 wt % $CaCl_2$/Nacl)	1.011	73.6	1.0

and that 0.4/0.4 wt % as 19.5 cp. The gelling solution was prepared by dissolving 10g $CaCl_2 \cdot 2H_20$ in 1000ml PBS ($CaCl_2$/NaCl 0.76/0.9 wt %). The fluid properties of the gelling solution were measured to be very close to that of water. Table 2.2 lists the measured properties for the reactive chemical solutions. Before the experiments, the poly-anion was filtered with a 0.4 μm filter and a small amount (less than 0.5 wt %) of red color was added for highlighting the anion solution in the pictures.

Drop on demand photographic system

Figure 2.1 is the schematic drawing of the experimental setup. A square transparent Lucite tank of 7.6 cm side and 17.8 cm height was used to hold the bulk liquid. The container is filled to almost four-fifths of the way to the top. The drop liquid is loaded into a high-capacity syringe (Hamilton Gastight 1050), which is mounted horizontally in a screw-driven slide (Velmex) actuated by a low speed stepper-motor. A small lure lock syringe (3 ml) with a needle termination is connected to the outlet of the high capacity syringe through silicon rubber tubing. The needle is positioned vertically above the center of the liquid tank. A laser diode-detector combination is mounted below the needle so that each time a drop pinches off the needle, the detector can detect it. The stepper motor can be switched on manually through a control box, and is automatically switched off once a pinched-off drop is detected. The pendant drop grows very slowly at the tip of needle. At a critical point, the drop weight exceeds the surface tension restraining force and the drop pinches off. A digital CCD camera (UNIQ-2000-12B), in combination with a Micro Nikkor 200mm lens, was used to record the interface deformations during drop impact. The camera resolution is 1680×1234 pixels. The sharpest spatial resolution of

this camera system is 9.0 micron/pixel. A high intensity fiber optic lamp in conjunction with a diffuser was used to uniformly illuminate the field of view. The typical frame exposure time is 50 μs, which is determined by the camera's electrical shutter speed. In later experiments, a synchronized flashing system, comprised of a digital delay box and a high power stroboscope (Stroboslave 1059, General Radio), was used to obtain sharper interface images. The flash duration of 1.2 μs eliminates the blur due to the high speed interface movement and thus allows more accurate measurement of the geometries.

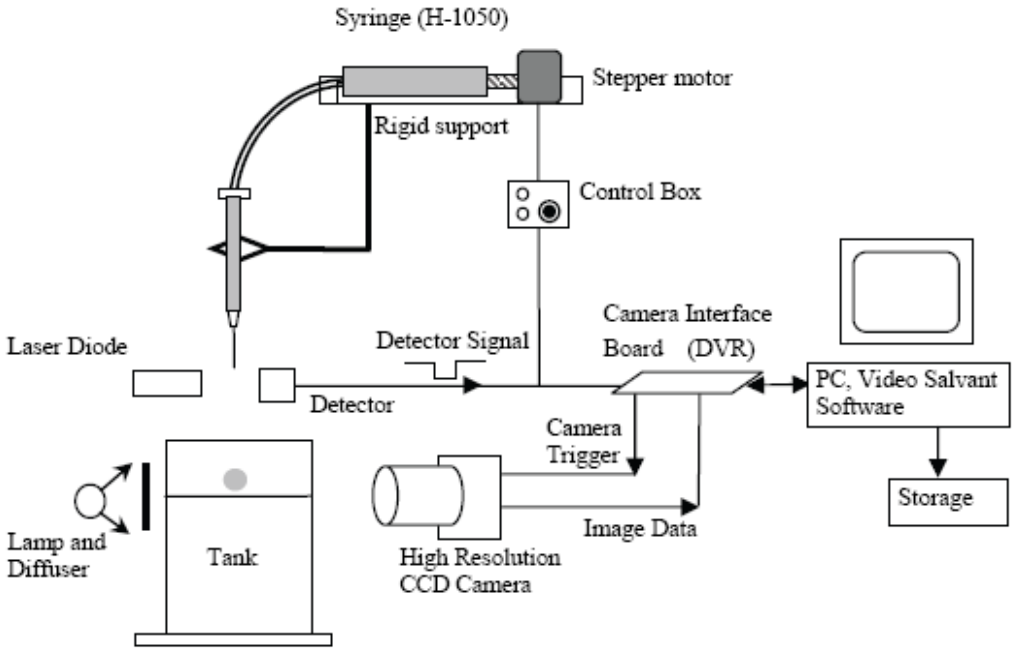

Figure 2.1. Schematic drawing of the experimental setup.

The diode-detector pair generates a timing TTL signal each time a drop pinches off from the tip and crosses the laser beam. Besides switching off the stepper motor, this signal is also sent to the camera interface board (DVR-Express, I/O industries Inc.) and suitably delayed before triggering the camera's electrical shutter. The control of delay time is achieved through the image acquiring software (Video Savant 4.0, I/O Industries Inc.). The delay period could be programmed in units of 25ns. For each run, a single frame was recorded and labeled with a time stamp of the delay period. By changing the delay time and repeating the same impact experiment, a sequence of frames with both high spatial and temporal resolution was generated. The frame on demand photographic system requires a very high repeatability of the drop size, and a high accuracy of the drop detecting signal. In order to improve the drop size repeatability, the needle tip was ground flat and a teflon (hydrophobic) coating was applied on the needle outer wall. The growing time for each drop before detachment is approximately one minute, which ensures that the internal flow disturbances during the drop growth are small. The timing uncertainty of the entire system has been evaluated to be about 0.08 ms.

Initial impact condition

The impacting drop size depends on liquid density, surface tension, and the outer diameter of the needle. In our experiments, 30G, 26G and 18G needles were used, with their outer diameters measured as 0.30 mm, 0.41 mm and 1.26 mm respectively. This gave drop sizes in the range 1.50 mm to 3.29 mm. The variation of drop size between different runs for the same size needle was evaluated to be less than 1%. This was ascertained by impacting a set of (about five) water drops onto a pool of oil and

photographing the slowly moving and non-oscillating drops. This method virtually assures an undistorted drop image, which was suitable for drop size calibration.

Due to the disturbances originating during drop pinch-off, the drop oscillates and thereby its impact shape is non-spherical. These oscillations are dampened by drop viscosity, and this effect is stronger for smaller drops. The oscillations themselves, however, occur over an equilibrium spherical shape, which is unaffected by the aerodynamic drag, owing to the short fall heights [103]. In the context of a water drop impact, the measured skew factor, which denotes the relative difference ΔR between two half-axes of an ellipsoid scaled by drop radius, reaches maximum of about 3%, while in most other cases the shape deviation is much lower. It is assumed that such low oscillation amplitudes will not affect the entrapment phenomenon. However, in the vortex ring regime, the vortex penetration has been observed to be influenced by the oscillation state of the impacting drop [71,104].

Different drop impact velocities are attained by changing the drop's free falling height, H, which is the distance from the tip of the needle to the surface of liquid pool. Considering the air drag force on the free falling drop, the drop impacting velocity can be calculated from the equation provided by [73]:

$$V = V_T \left[1 - \exp\left(-\frac{2gH}{V_T{}^2} \right) \right]^{\frac{1}{2}} \tag{2.1}$$

V_T is the terminal velocity determined by the drop diameter, and can be calculated by a polynomial fit to a set of experimental data shown in [105]. The actual impacting velocity was measured by multi-exposure method, with the aid of a stroboscope (GenRad

1539A). The agreement between the measured impact velocity and that through equation 2.1 is very good, as shown in figure 2.2.

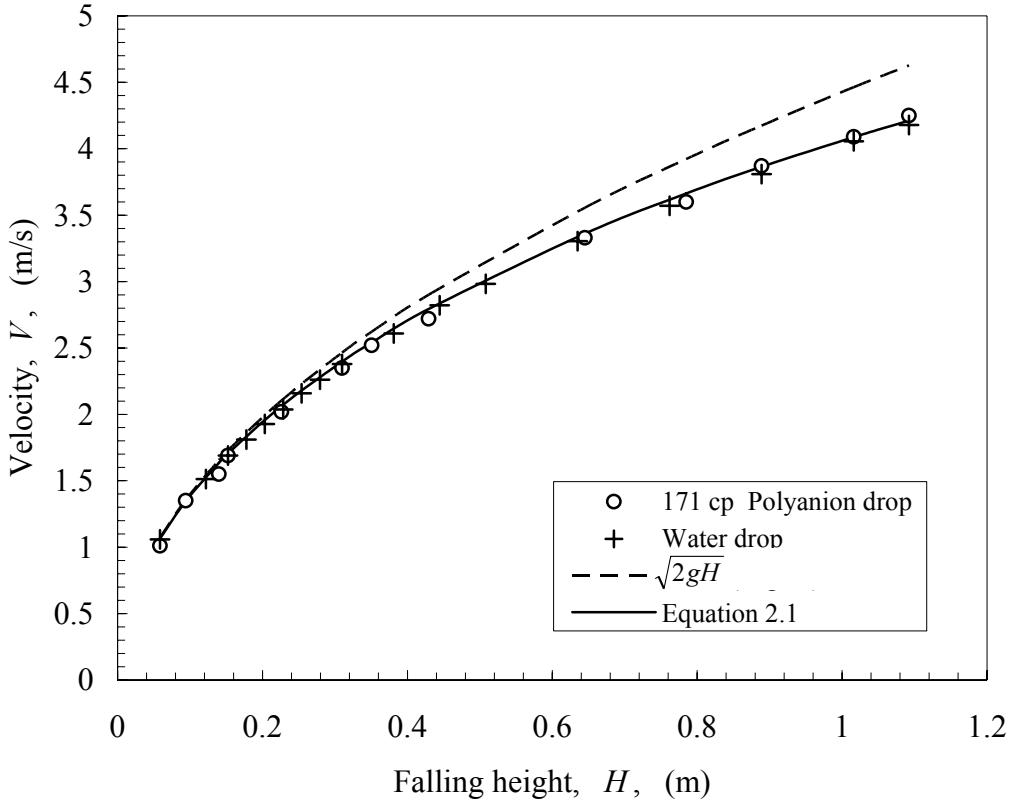

Figure 2.2. Measured impacting velocity compared with the theory.

The measured horizontal velocity at impact position was less than 0.5% of vertical velocity, which indicates that all drops impact relatively normally onto the surface. If the falling height is too long, even the small horizontal disturbance will change the position of impact, moving the impacting crater out of the field of view. With these concerns, the impacting velocity range was chosen between 0.9 m/s to 3.3 m/s. This experimental range guaranteed that the experiments encompassed the regular bubble entrapment regime.

Based on the measurements described above, the computed *We* and *Fr* numbers have been estimated to have errors of less than 3%.

Apparatus for making smaller drops

In order to obtain the bubble entrapment limits in *We-Fr* plane, parametric experiments with wide range of impacting drop size and velocity need to be carried out. However, the diameter of drop generated by free falling method is very limited; the smallest water drop has a diameter of 2.28mm, corresponding to the 30G needle. Hence, a piezoelectric actuator system is used to dislodge the drop from the needle tip before its size becomes too big. Figure 2.3.a shows the sketch of such a set up used for generating repeatable sub-millimeter sized water drops. Here the needle is mounted to a piezoelectric actuator. The syringe pump continuously pushes the drop liquid out of the needle at a constant slow speed to grow drops. The actuator is driven by a function generator and amplifier. Each time the actuator receives a wave signal, it generates a sudden vertical acceleration, which detaches the drop from a needle. With the pumping flow rate kept constant, a series of drop sizes can be achieved by adjusting the frequency of the driving wave, as shown in figure 2.3.b. The smallest drop diameter obtained is about 0.75 mm. The main shortcoming of this system is that the trajectory repeatability is not as good as in the free fall system, since the sudden movement of needle induces more horizontal disturbances. Hence most high resolution photographic study was carried using drop generated by the free falling drop dispenser.

(a)

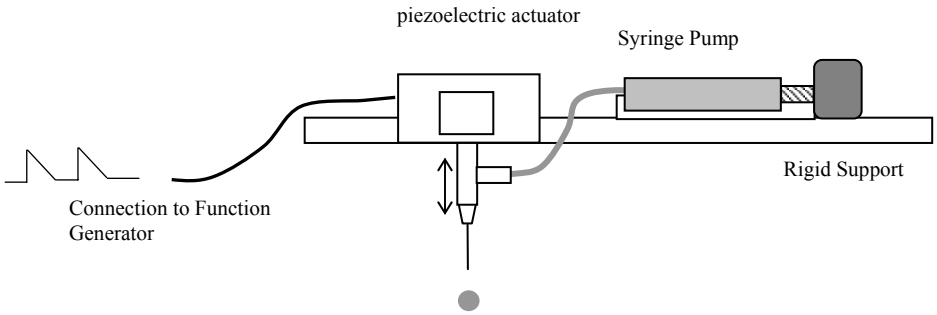

(b)

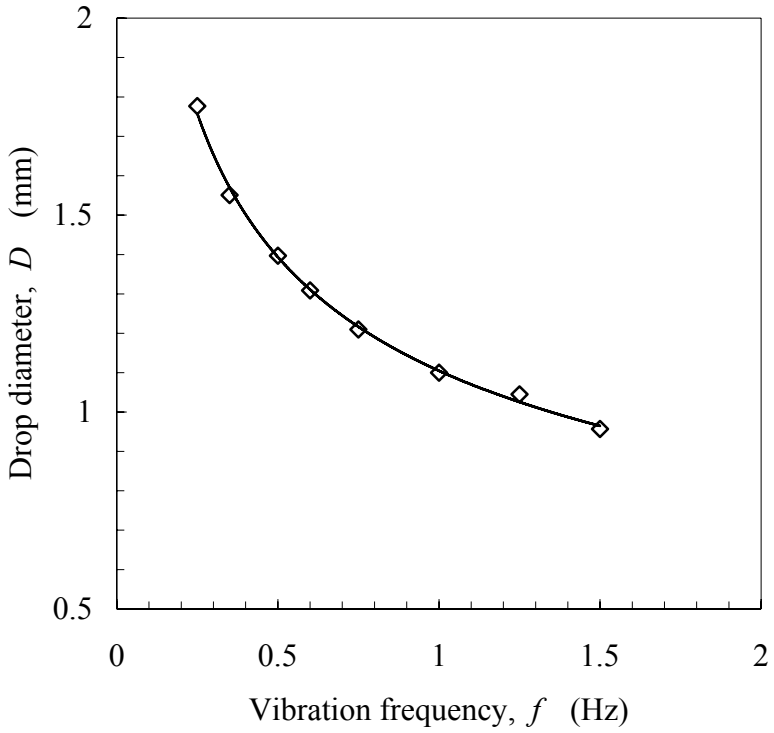

Figure 2.3. (a) Sketch of apparatus used to generate small water drops. (b) Water drop diameters measured against exciting wave frequency.

Image processing

Drop size, bubble size and crater cone angle and other basic geometrical parameters were measured directly from digital images (in bit-map format) through Paint tool in Windows XP. The spatial resolution of the each digital picture was calibrated via a standard line scale (200 lines per inch). Entrapped bubble size, *d*, is the averaged value of five measurements under same impacting condition. The minimum measurable bubble size is approximately 4 pixels, corresponding to a bubble size of 45 micron. The crater cone angle is obtained by calculating the slope of the crater side-wall.

An edge-detecting program was developed to extract accurate profiles of the main body of the high rising thin jet. This program was written and run in an easy-to-use

Figure 2.4. Free surface profile (white line) extracted from the original digital picture.

coding software (IDL Research System Inc). The process of the edge detection can be described as follows. First, for each horizontal line (vertical coordinate *Yc*), the edge is first crudely determined as the pixel coordinate (Xc_0) where maximum jump of pixel value in two consecutive pixels occurs. Then the edge position (horizontal coordinate) is further refined using center of mass method [106]. The center of mass difference can be calculated as:

$$\Delta Xc = \frac{\sum_{1}^{n} P(i) - n * P(n)}{P(1) - P(n)} - 0.5 \tag{2.2}$$

where P(i) is the pixel depth, n is the length of the short evaluating string centered with X_{c0}, usually n=5. The actual edge position will be ($X_{c0} + \Delta X_c$, Y_c). The resolution of the edge defined via this method can reach sub-pixel level. By repeating the horizontal edge detection in selected vertical direction, a set of coordinates representing the edge of the thin jet can be derived for each frame. Figure 2.4 shows that this edge detection method is accurate in extracting the thin jet profile from original pictures. These spatial coordinates together with time information of each frame were further processed through Polymath software for modeling purposes.

CHAPTER III

BUBBLE ENTRAPEMENT IN LIQUID DROP IMPACT HD ONTO A DEEP LIQUID POOL

Introduction

Bubble entrapment in encapsulation process, as described in figure 1.4, is very undesirable since it deteriorates the capsule surface quality and affects the sedimentation of gelled capsules. This bubble entrapment occurs during the dynamic drop impact process when a viscous poly-anion drop impacts onto an inviscid gelling solution. The front gelling reaction changes drop liquid and interface properties, and hence makes bubble entrapment phenomenon more complicated than that in the classical liquid drop impact. As a first step to tackle the viscous reactive drop impact problem, as in the encapsulation process, this chapter will examine the non-reactive liquid drop into the pool of the same liquid with emphasis on the role of viscosity and surface tension.

Many of the earlier studies on drop impact onto deep liquid pool have been carried out using pure water as the medium. Very few studies have investigated the effects of viscosity and surface tension, except Pumphrey & Elmore [73] who note that when a small amount of surfactant is added to the liquid, bubble entrapment is totally suppressed. To further understand the fluid dynamics involved in bubble entrapment phenomenon, it is necessary to include viscosity and surface tension in the experiments. Practically, impacting drops and bulk fluid may consist of different liquids of which the viscosity and surface tension may vary in a wide range. In cell encapsulation, the drop viscosity is

higher than 100 cp, and as gelation proceeds the viscosity continuously increases as the solid gel structure is formed.

Another aspect of interest of this chapter is to quantify the high-rising thin jet profile following bubble entrapment. Since the ejection of high speed thin jet always accompanies bubble entrapment, the analysis of the thin jet dynamics can convey useful information on modeling the dynamics near the bubble pinching moment. Similar thin jet singularity is also seen in other hydrodynamic situations like surface wave collapse [80,81] and collapse of surface voids [82.83]. In these contexts, the phenomenon is purely driven by fluid inertia, and is referred to as inertial focusing. To demonstrate this focusing effect, the surface geometries prior to collapse have been scaled as power law dependence with time [82,84-86]. A similar scaling approach in the drop impact problem could draw attention to the bulk flow focusing effects in bubble entrapment and thin jet formation.

Three liquids: distilled water, silicon oil, and glycerin-water mixture have been used as experimental fluids, allowing for the variation of both surface tension and viscosity. For each set of liquids, dynamic impacting conditions for bubble entrapments have been measured and expressed in dimensionless *We* and *Fr* numbers. Critical crater shape, which represents the crater shape right before the bubble pinch off, and entrapped air bubble size, has been examined in detail. A power law singularity with respect to time has been fitted from the experimental data. Later in this chapter, the experimental observations on viscous drop impact onto miscible non-reactive inviscid pool (asymmetric impact), which is the intermediate phenomenon between simple drop impact and capsule formation impact, are presented.

Preliminary result on water drop impact onto the surface of a deep water pool

The objective of the experiments with pure water system is to verify the results reported in the literature, and by so doing to justify the applicability of current experimental set-up to further study the new drop impact phenomena, involved in the encapsulation process. Also presented in this section are some observations regarding to the regular bubble entrapment which have not been reported in the literature.

Regular bubble entrapment limits

Figure 3.1 shows the comparison of the current experimentally determined regular bubble entrapment limits with those reported in [73]. In general, a very good agreement between the two sets of data is seen. The slight difference might be because of the different approaches in determining the event of regular entrapment. Oguz and Prosperetti's [74] theoretical analysis suggests the upper and lower limit for regular bubble entrapment follows as $We \sim Fr^{0.25}$, and $We \sim Fr^{0.2}$ respectively. These relationships are plotted in *We-Fr* plane, as seen by the solid lines in figure 3.1(b). It appears that the theoretical limits agree with the experimental data from both the data sets.

Figure 3.2 shows a series of pictures captured at the moment of crater collapse, with the impacting condition encompassing the lower and upper bubble entrapment limits. It is seen that as the impacting energy, represented by *We* or *Fr*, increases, the entrapped bubble size starts from a small bubble and increases to a peak (between $H = 8$ and 9 inch), and then decreases again due to the bottom reversal flow occupying a portion of the air pocket before pinch-off. A vestigial bubble entrapment is seen at H=12 inch of figure 3.2, where the local reversal flow distorts the air pocket into a complex bubble shell.

(a)

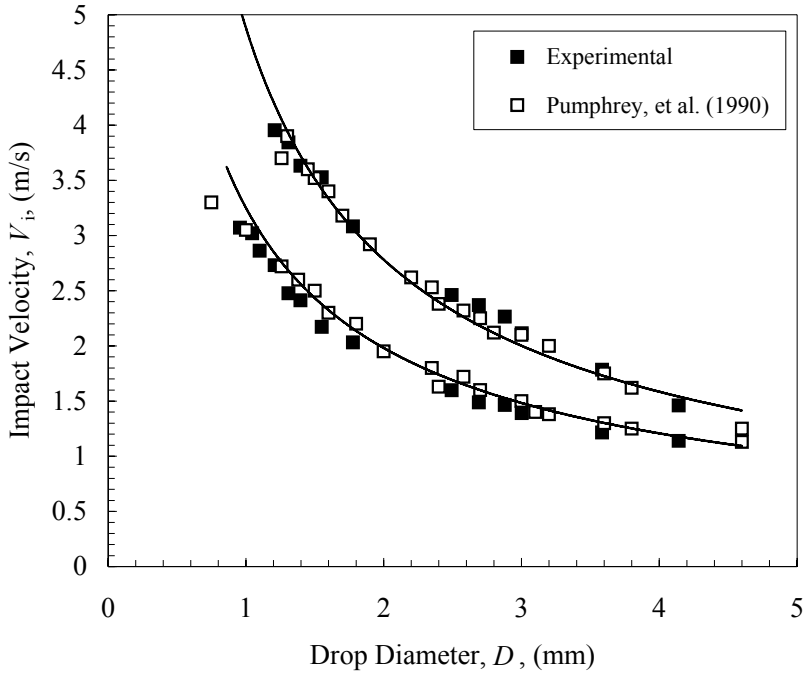

(b)

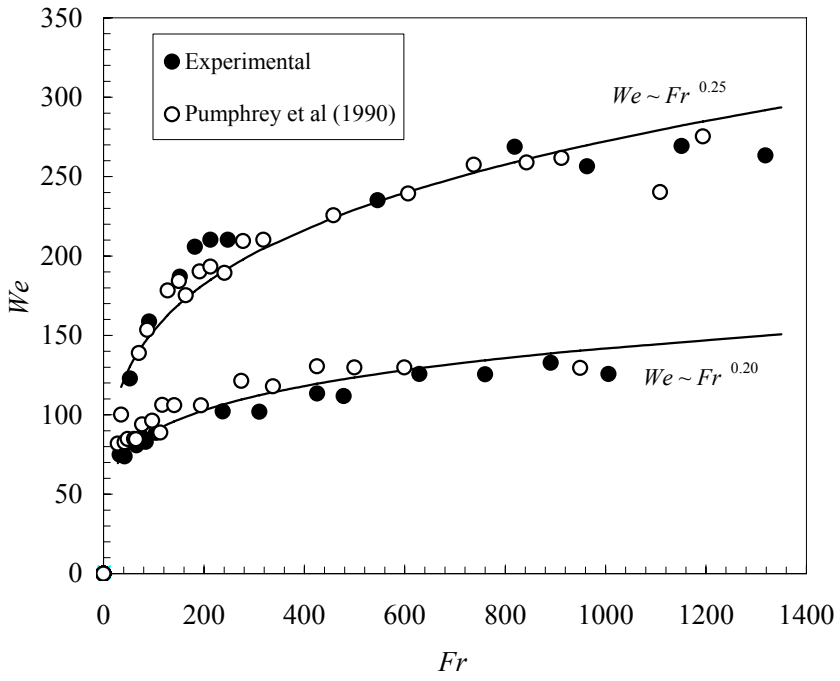

Figure 3.1. The regular bubble entrapment limits determined by water drop impact experiments. (a) Data showing the lower and upper limits of impacting velocity V for the occurrence of bubble entrapment, versus drop diameter, D. (b) Bubble entrapment limits plotted in *We-Fr* plane. The solid line is the predicted trend by [74].

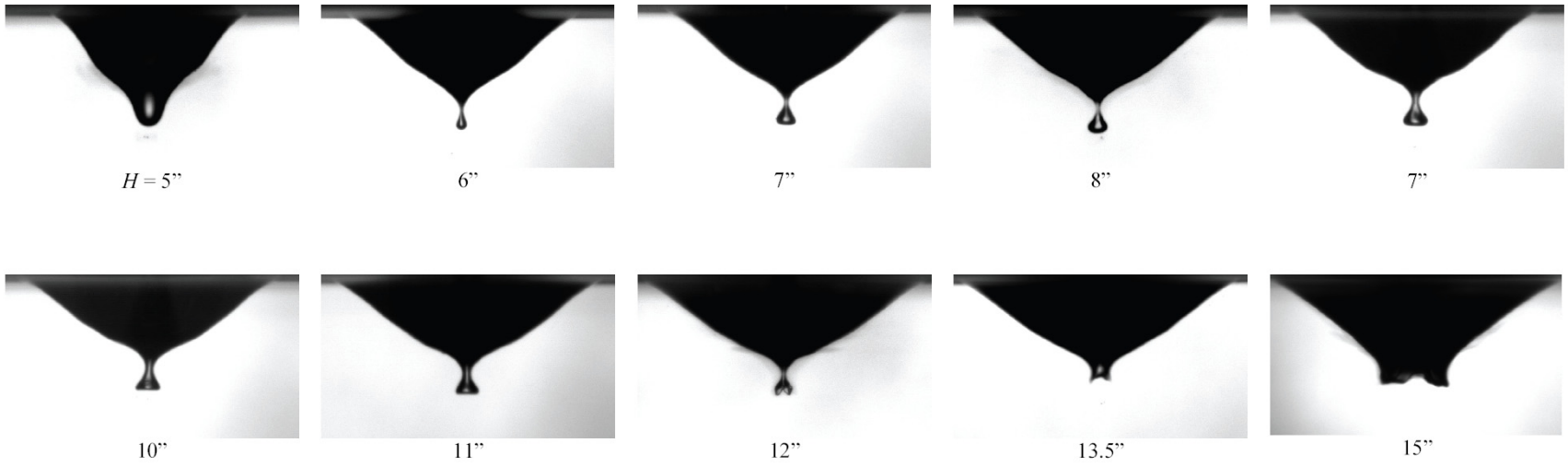

Figure 3.2. Comparison of the critical crater shapes observed during a 2.5mm water drop impact onto a water pool under different kinetic conditions. The impacting velocity is varied from low to high to ensure that the impacting condition encompasses the regular bubble entrapment limits. The label of each picture represents the free falling height, *H*.

This thin bubble shell is then pinched off and usually breaks into two bubbles instead of restoring into one single bubble. As the impacting energy further increases, (H=13.5, 15 inch) the reversal flow prevents the side wall pinch off, and no bubble entrapment is observed under these conditions. Based on these observations, it is clear that the upper limit of regular bubble entrapment is related to the timing of, and amplitude of, the central reversal flow. This argument differs from the one from those in [74], where they attribute the lower limit, not the upper limit, to the similar unsynchronized reversal of the crater wall.

Crater morphology

Figure 3.3 shows a sequence of pictures taken during a 2.5 mm water drop impact onto water pool. In figure 3.4.a the nondimensional crater depth, $R'=R/D$, is plotted versus time, $t'=t/(V/D)$. The crater grows spherically following the impact of the water drop, and the growth speed decelerates until the crater reaches maximum depth as seen in figure 3.4.a. Then the bottom maintains the position for a short period, meanwhile, the slope of crater side wall starts to decrease, indicating there is a radial inward velocity component in the flow field around crater. More specifically, the inward flow velocity must increase towards the crater base. This inward flow is driven by hydrostatic force [82,83,107]. When the inward flow reaches symmetry axis, there will be a high-pressure stagnation point, where the radial velocity component drops to zero. Since this collapse point is near the air-liquid surface, it can drive a high-speed thin jet upwards, as seen at t = 21.3 ms in figure 3.3.

A concentric traveling capillary wave along the crater wall is noticeable form the picture sequence. The front of the traveling capillary wave is indicated by arrows in figure 3.3. The depth of the wave is measured from each frame and plotted against time in figure 3.4.b. Unlike the crater bottom, the capillary wave front appears to move at a constant speed downward. The importance of traveling capillary wave to regular bubble entrapment is discussed as follows. In the absence of traveling capillary wave, the focusing flow will collapse at the bottom of the crater where the hydrostatic pressure is higher than other positions along the crater wall. Accordingly, the crater will represent a perfect cone shape at the moment of collapse and no air bubble will be entrapped following the collapse. On the other hand, the capillary wave acts as a disturbance to the cone tip and turns the local free surface into a typical hourglass shape, as seen in t = 17.2 ms (figure 3.3). Meanwhile, the wave crest, represented by the neck of the hourglass, is continuously pushed by the inertial focusing flow till collapse, leaving an air bubble entrapped. One should differentiate the regular bubble entrapment in liquid drop impact from that in solid object impact as reported in [82,107]. In the later case, since the bottom of the air cavity is restricted by a moving solid boundary, the cavity always collapses at a certain depth above the pinned cavity bottom and pinches off a large air pocket.

The nondimentional kinetic condition (Fr=151.7, We=129.8) of the water drop impact shown in figure 3.3 is selected to be very close to the case of 1cs oil drop impact shown in Figure 3.10.b. Despite the big difference in surface tension and impacting velocity, the two events share a great similarity in crater morphology, see figure 3.4. This confirms that the regular bubble entrapment in inviscid liquid system is regulated by the

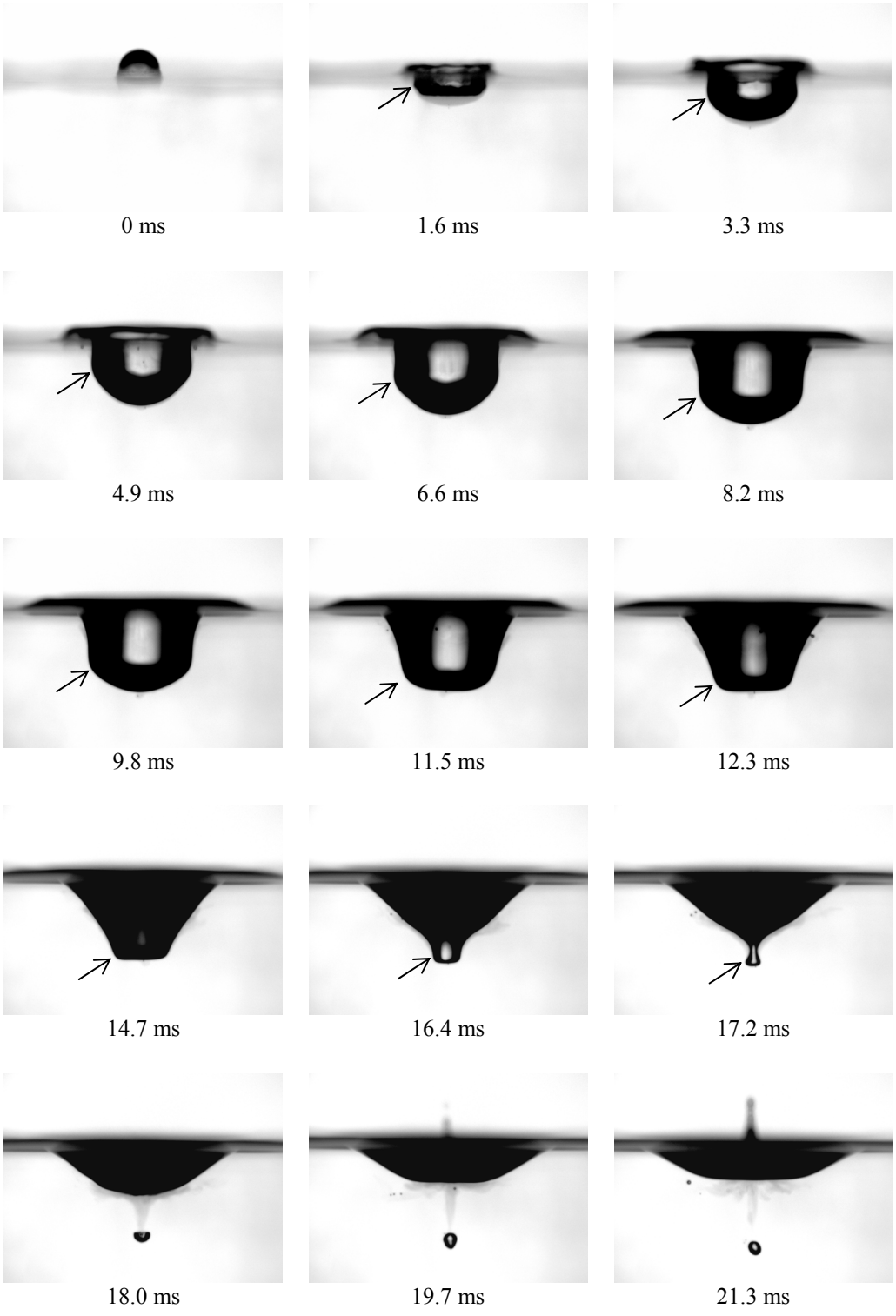

Figure 3.3. Pictures showing a typical sequence of crater formation and collapse following a water drop impact onto a water pool, with the impacting parameter located inside the regular bubble entrapment limits. (*Fr*= 151.7, *We*= 129.8)

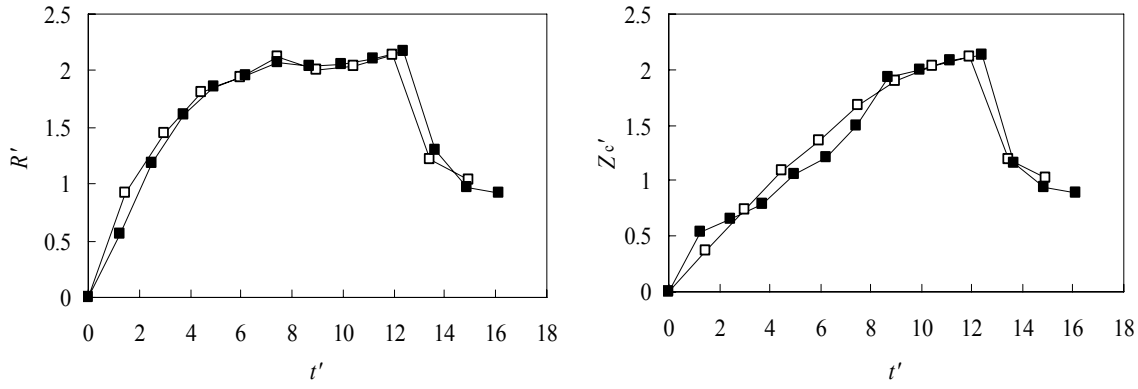

(a) (b)

Figure 3.4. The crater depth *R'*, and the vertical position of traveling capillary wave relative to the equilibrium surface, Z_c*'*, plotted against time, *t'*. (■) denotes water drop impact at *We*=129.8, *Fr*=151.7, as seen in figure 3.3; (□) denotes 1 cs oil drop impact at *We*=136.0, *Fr*=130.7, as seen in figure 3.10.b.

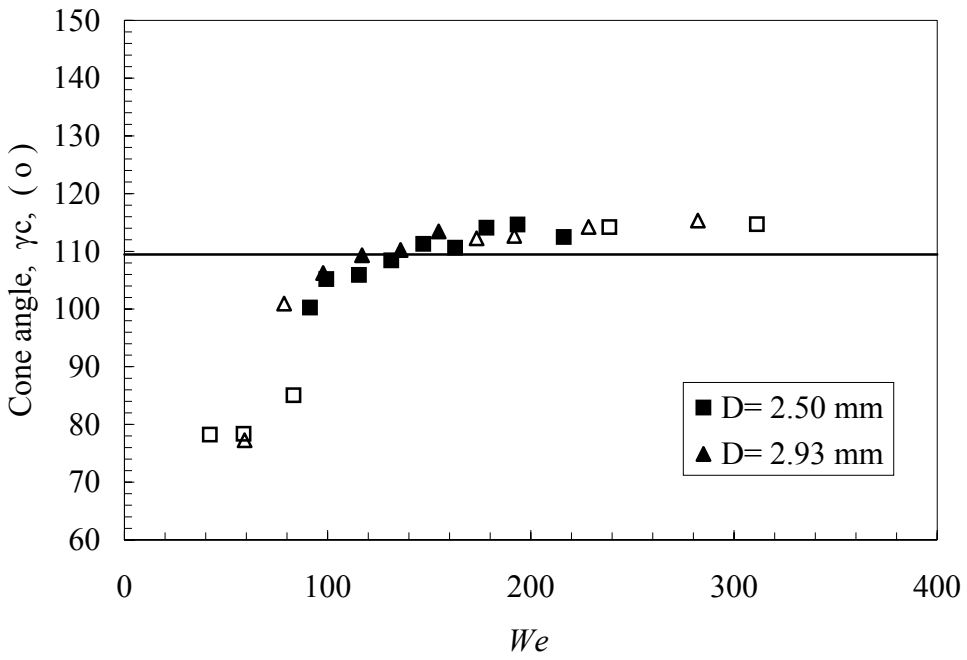

Figure 3.5. Critical cone angle, formed between the collapsing crater side-wall at the moment of bubble pinching (t=t_c) plotted against impacting *We*. The solid line is the constant of 109.5^o predicted by [79]. The solid symbols denote bubble entrapment observed after the crater collapse, and the open symbols correspond to no bubble entrapment. Data shown are from water drop impact experiments, with different drop size and impact velocity.

interplay of surface tension, inertia and gravity force, which can be completely captured by *We-Fr* combination.

Critical cone angle

Figure 3.2 shows that the disturbed water air free surface always represents a nearly conical shape at the moment of crater collapse. The cone angle is determined by measuring the slope of the straight line between the crater bottom corner to the cone base. Figure 3.5 shows the measurements to the critical cone angle, γ_c, observed at the moment of bubble pinching, as function of *We*. It appears that when bubble entrapment occurs, the critical cone angle is in good agreement with the theoretical prediction of 109.5^o [78,79]. The coincidence of this critical cone angle and bubble entrapment indicates that at the moment of crater collapse, there is a singularity in the local flow field near the crater wall. In the low *We* regime, the cone angle is much smaller, suggesting the collapse is less intense. In the high *We* (>100), although the cone tip is disrupted by the reversal flow, the angle measured according to the side wall slope is still close to 109.5^o, implying that in absence of reversal flow, entrapment has no upper boundary.

Another way to verify the development of singular conical flow during the bubble pinching is to measure the evolution of the cone angle with time. Usually when the crater reaches to maximum depth, the slope of side wall decreases so that he cone angle increases as it approaches to the critical value. Figure 3.6.a shows the comparison of the measured cone angle, γ , with the analytical solution provided by [79]. The time label τ is the nondimensional value obtained through linear interpolation/extrapolated according to the table 1 of [79]. There is a good agreement between the experimental data and the

(a)

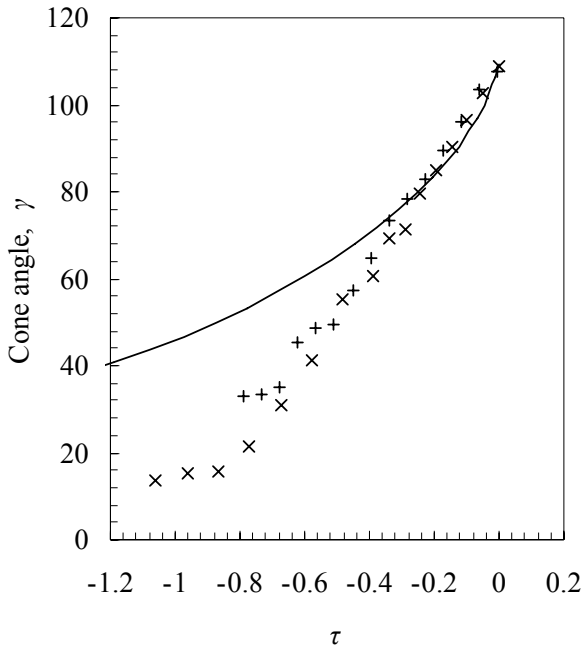

(b)

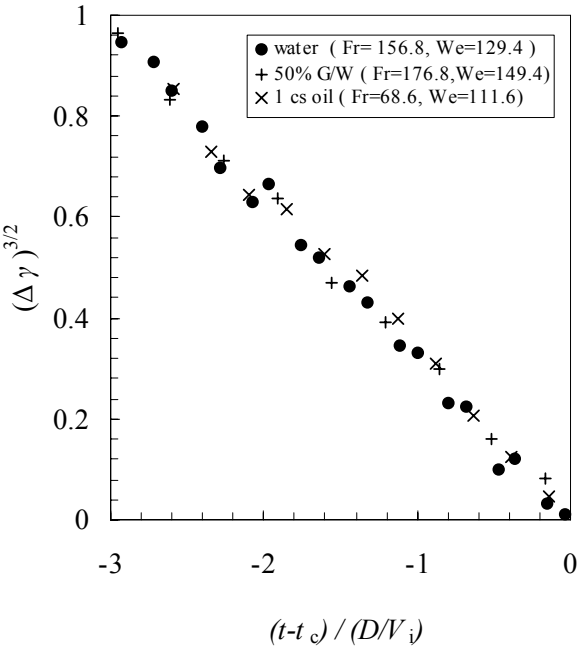

Figure 3.6. Plot showing the evolvement of the cone angle with time approaching crater collapse/bubble pinching moment. (a) Measured cone angle, γ, plotted against time τ. The data points are collected from the 2.50 mm water drop impact with Fr=68.6, We =111.6 (two experiment runs). The solid line is the predicted cone angle evolvement according to the analytical model from [79]. (b) Plot shows that $(\Delta\gamma)^{2/3}$ varies linearly with the nondimentional time, $(t-t_c) / (D/V)$, in agreement with the model.

model, only when the time is very close to the pinching moment, $\tau = 0$. In the left part of figure 3.6.a, the actual cone angle is much smaller than the model. This can be explained by the fact that the analytical model does not include the gravitational force, which is important in crater formation and collapse. However, when time is very close to singularity (pinching), the inertial force dominates over hydrostatic force, so in this small regime the theoretical model may be valid.

Longuet-Higgins also derived an asymptotic solution to the cone angle value as time approaches the critical moment, which is $\Delta\gamma^{2/3} \sim t$, where $\Delta\gamma = \arctan(2^{1/2}) - \gamma$ in radius unit. In figure 3.6.b the $\Delta\gamma^{2/3}$ is plotted against nondimentional time $(t-t_c) / (D/V)$. The data points in figure 3.6.b are obtained from three different liquid systems: water, 1cs oil and 5.9 cp G/W. The linear relationship is recovered very well for all three sets of data, and the slopes of the data trajectory for different systems appear to be a constant. The above quantitative analysis suggests that the universal global conical flow model can well capture the crater dynamics at the time close to crater collapse and bubble pinching.

Origin of the traveling capillary waves

Figure 3.7 shows a set of pictures taken immediately after the initial contact between the drop and pool surface. It is seen from the first picture from left (t=0.2 ms) that two circular ripples are formed above the connecting neck, as seen as two white lines in the picture. As the drop continuously falls down and therefore the neck area expands horizontally, the two ripples climb upward along the drop surface (t=0.4 ms). Meanwhile, strong azimuthal instability develops on the drop surface. The amplitude of the ripples seems to increase, as time elapses to t=0.6 ms. The ripple closer to the pool surface has a

higher amplitude than the one above it. Eventually, these ripples move downward as the impacting crater starts to grow. It is possible that the ripple with higher amplitude serves as the origin of traveling capillary wave which is responsible for the regular bubble entrapment.

The capillary ripple generated during a water drop impact onto a water pool has never been studied in detail in the literature. However, the experiments on momentumless drop coalescence does show the existence of a pair of ripples right after the rupture of film separating the drop and pool surface [107]. But in the liquid-liquid system the ripples do not climb up to the drop surface, unlike the current experiment. Dooley *et al.* [68] studied the momentumless drop coalescence problem in air media. Their photographs show that after the initial contact between drop and pool surface, some pool liquid climbs up to cover the drop surface, although no ripples are observed along the surface in their case. Martin [108] recently modeled this capillary phenomenon by balancing the energy between surface energy lost to the gravitational potential increase and the kinetic energy due to the upward motion of some portion of the pool liquid. His result shows a good agreement with the experimental data.

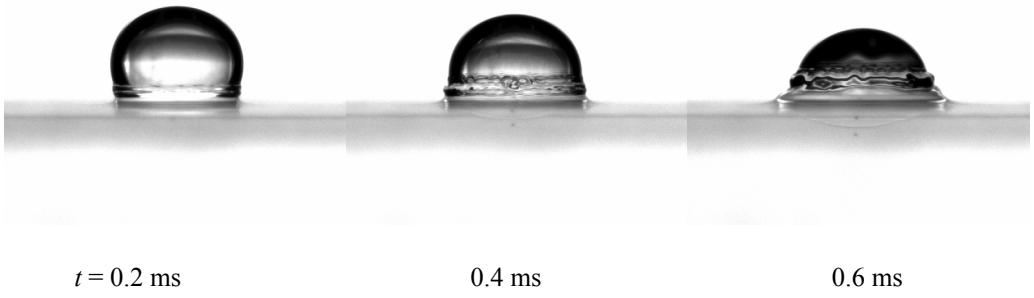

Figure 3.7. Pictures showing the capillary disturbance to the free surface due to the initial contact between water drop and the pool surface.

Effect of surfactant

Later in this chapter, it will be shown that the surface tension alone does not affect the phenomenon of regular bubble entrapment, as evidenced by the fact that the bubble entrapment limits in *We-Fr* plane for water and 1 cs oil are similar. However, Pumphrey and Elmore in their original paper mentioned when surfactant is added to the water pool, the bubble entrapment disappears under the same impact condition. One possible reason for this is that the addition of surfactant lowers the surface tension, and hence increases the effective *We* even though the impact velocity and drop size remain same. The increase of *We* may move the impact condition on the *Fr-We* plane above the upper bubble entrapment limit, so no bubble entrapment will be observed.

To further examine this issue, a small amount of soluble surfactant (Symperonic PE/L61, 1g/L) was added into the water pool, and the water drop impact experiments were repeated over the wide velocity range. Indeed there is no regular bubble entrapment in the whole *Fr-We* regime. Figure 3.8 shows the sequence of crater formation and restoration when surfactant is added. It is seen that during the growth phase, the crater wall is very smooth and close to semi-spherical, in direct contrast to figure 3.3, where the traveling capillary wave along the wall is obvious. The crater starts to restore after t=16.4ms. During the crater restoration, there are no sharp edges at the bottom, and no bubble pinch-off is observed.

The above phenomenon can only be explained by the effect of dynamic surface tension (DST), which is the result of uneven surfactant distribution along the free surface. When surfactant is present on the liquid-air surface, the surface tension is determined by the local concentration of the surfactant molecule. In the equilibrium state, the surface

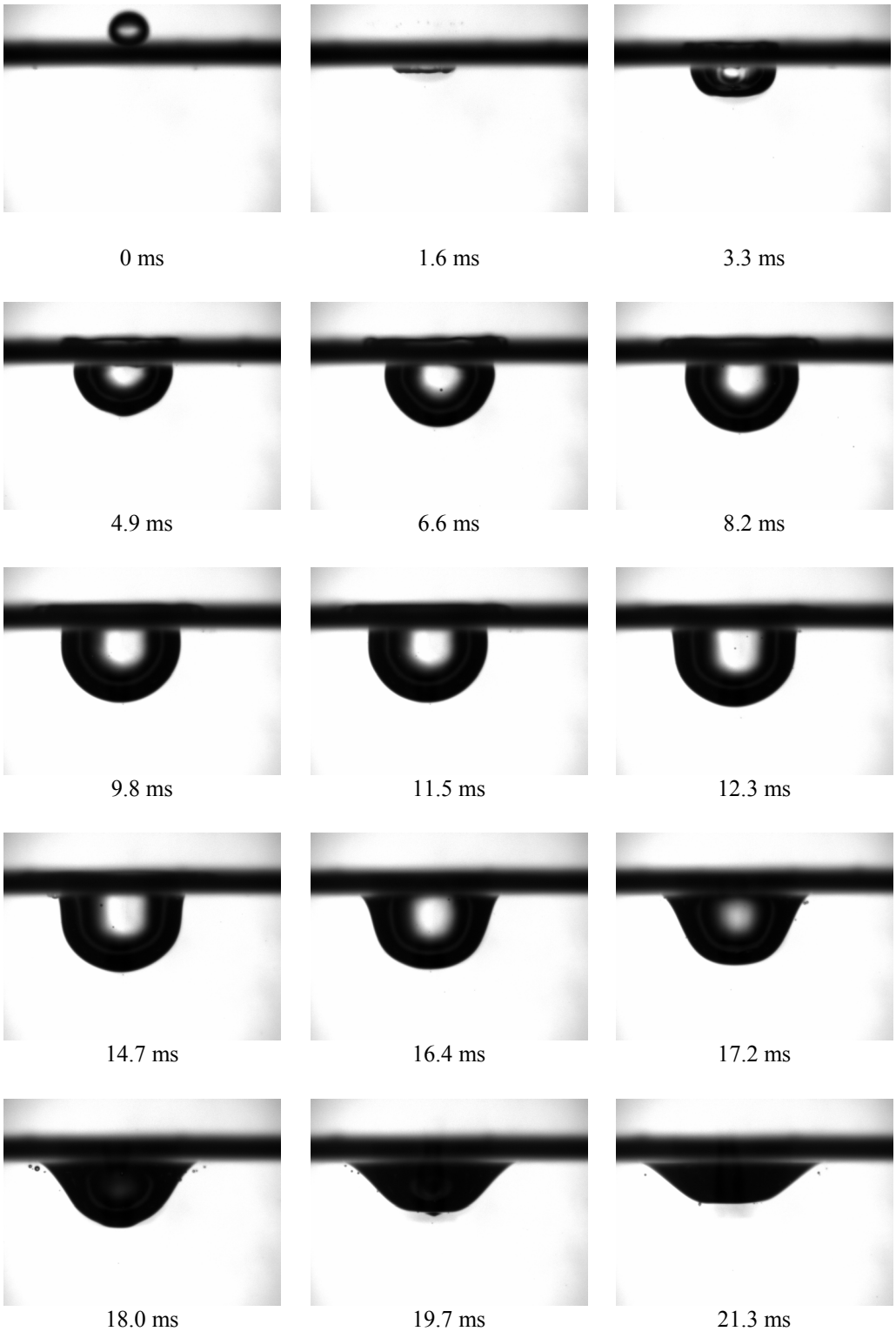

Figure 3.8. Pictures showing that the addition of surfactant to the water pool prevents regular bubble entrapment. The impacting drop size and velocity is same as the one shown in figure 3.3. (*Fr*= 151.7, *We*= 129.8)

tension is constant throughout the free surface (40.3 dyn/cm in present study). The capillary ripple promotes surfactant spreading, resulting in a surface tension gradient. The associated Marangoni effect opposes this surfactant spreading. In doing so, it opposes the ripple motion itself.

Inviscid oil drop impact: effect of lower surface tension

The main objective of the oil drop impact experiments with low viscosity was to corroborate the baseline results available in the literature, before examining the viscous effect of on bubble entrapment. A secondary objective was to work with silicon oil, in addition to water-based systems, as it is a well-characterized fluid, is readily available in various viscosity grades, and its surface tension is almost a quarter of that of water. Further, unlike water, the surface tension of silicon oil is insensitive to minor contamination, if any, and the working liquid does not require mixing, and can be stored in the syringe over long time.

The experiments with the low viscosity silicon oil were carried out using two different needles and with the drop impact velocity in the range of 0.90m/s to 1.69m/s. For each run, the impact condition was plotted as a point in the *We-Fr* plane, with appropriate symbols to denote the observed entrapment signature. As shown in figure 3.9, regular bubble entrapment in oil system occurs within the parameter regime, which is close to that established by Pumphrey & Elmore [73] and thre current study using water system. This suggests that the *We-Fr* combination is able to capture this capillary effect.

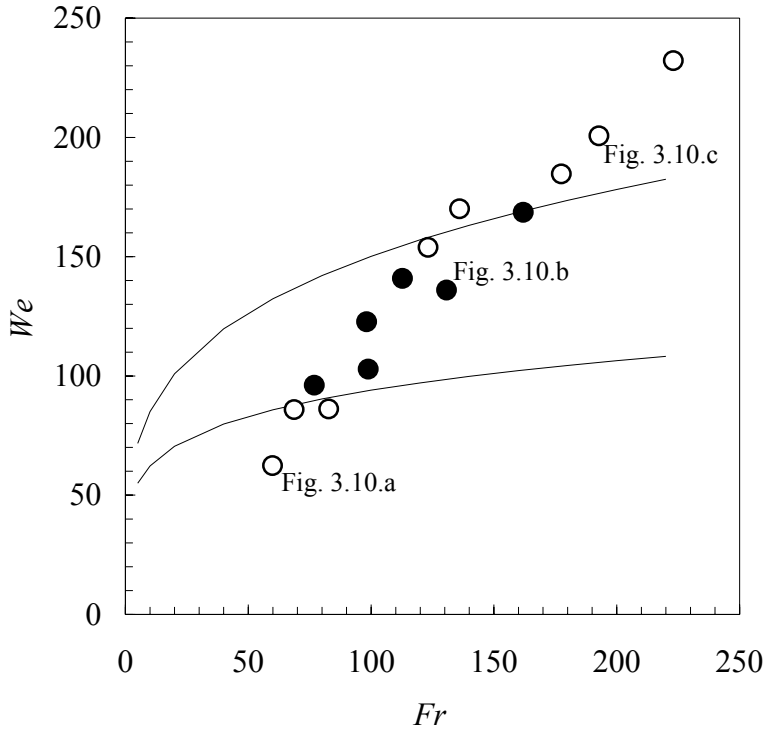

Figure 3.9. *Fr-We* plot showing the regular bubble entrapment regime for a low-viscosity liquid system. Solid lines are regular entrapment limits determined for water impact system by Pumphrey and Elmore [73]. Filled circles denote regular bubble entrapment for low viscosity (0.82 cp) oil drop impact, and open circles denote absence of regular bubble entrapment.

The crater profiles within and outside of regular entrapment regime for 1 cs drop (μ=0.82 cp) impact are shown in figure 3.10. Figure 3.10.a shows the crater profiles for the impact parameters below the entrapment regime (refer to the corresponding point in figure 3.9). The thick dark horizontal line at the top in each picture represents the oil-air interface. The evolving dark feature is the impacting crater. The dyed drop fluid can be seen as gray area around the crater bottom. Since the drop fluid and the pool fluid are identical, the drop fluid would be invisible, unless dyed. The drop fluid is flattened right after initial contact, followed by the growth of the impact crater. The drop fluid expands

as crater grows, then forms a circular blob near the crater side wall. When the crater starts to recede, the drop fluid aggregates at the crater bottom, and organizes itself into a vortex ring structure. At later time, the ring moves downward, with a filament extended to the free surface. A pair of small air bubbles about 0.05 mm in size, are seen at the bottom of the drop fluid (vortex ring). These air bubbles are caused by the sudden rupture and contraction of the air film, located between the drop and the bulk interface, and they are not formed by the regular entrapment process [64].

As the impacting velocity is increased, so that the impact parameters (*We* and *Fr*) are located in the regular entrapment regime (figure 3.9), a different crater evolution is seen**.** After the crater grows to its maximum depth, its bottom stays at the same position for a while and the sidewall starts to converge, transforming the crater shape from a hemispherical to a conical one. At the same time, a concentric capillary ripple travels along the crater sidewall, as shown by the arrows indicating the wave troughs in figure 3.10.b. The origin of this traveling capillary wave is related to the strong surface disturbance following initial contact of the impacting drop [76, 107, 109,110], as evidenced shown above in figure 3.7. Some of the concentric ripples emanate away from the impacting crater rim, while others travel along the crater wall toward the symmetry axis. When a capillary wave reaches the bottom of the crater at the right time its crest closes concentrically to trap an air bubble. After bubble pinch-off, a very high speed thin jet is ejected upward, as seen by a column of droplets in the inset (t = 14.7 ms, figure 3.10.b). The jet starts to thicken as the crater bottom begins to rebound. The thin grey filament from the bubble to the crater indicates that most of the drop fluid moves upward together with the bulk reversal flow.

Figure 3.10.c shows the evolving crater signatures on further increasing the impact velocity, whereby, the impact parameters are above the entrapment regime (figure 3.9). The early development of the crater profile resembles a growing hemisphere. The drop fluid is hardly seen from the pictures since it is evenly distributed along the crater and forms a thin film. In contrast to the bubble entrapment craters of figure 3.10.b, where a single concentric capillary ripple is involved, the crater inner surface here is disturbed by a series of concentric ripples. This changes the morphology of the crater and interferes with the effective closure of the crater wall as seen in the earlier scenario (figure 3.10.b). There is no dramatic crater closure and appearance of a thin jet; instead the crater rebound is through a thick jet. Since the impact parameters for figure 3.10.c is still close to the entrapment boundary, a vestigial capillary closure and entrapment effect can be seen in the time frame corresponding to 14.7 ms.

An unexpected observation in figure 3.10.c is that a vortex ring forms again at the condition above the upper limit for bubble entrapment. After t = 15.5 ms, the distributed drop fluid starts to concentrate itself again at the crater bottom and develops into a small vortex ring structure. The ring grows slowly and moves downward, leaving a filament behind. This vortex ring formation above the regular entrapment limit has not been observed experimentally in the water system. However, numerical simulations of Morton, Rudman & Leng [76] predict the vortex ring formation both below and above the regular entrapment limits. They state that at higher energy impact, vorticity is generated in the vicinity of the traveling capillary wave, whereas in the traditional low *We* vortex ring regime, vorticity is generated due to the initial contact between drop liquid and the bulk. This seems to agree with the current observations with the oil system (figure 3.10.c).

Vortex ring structure can only be seen if the vorticity can concentrate in a certain area. If the local convective flow is strong, vortex ring formation is affected. This is probably the reason why no vortex ring is observed in regular bubble entrapment, where the bulk flow convective effects are strong.

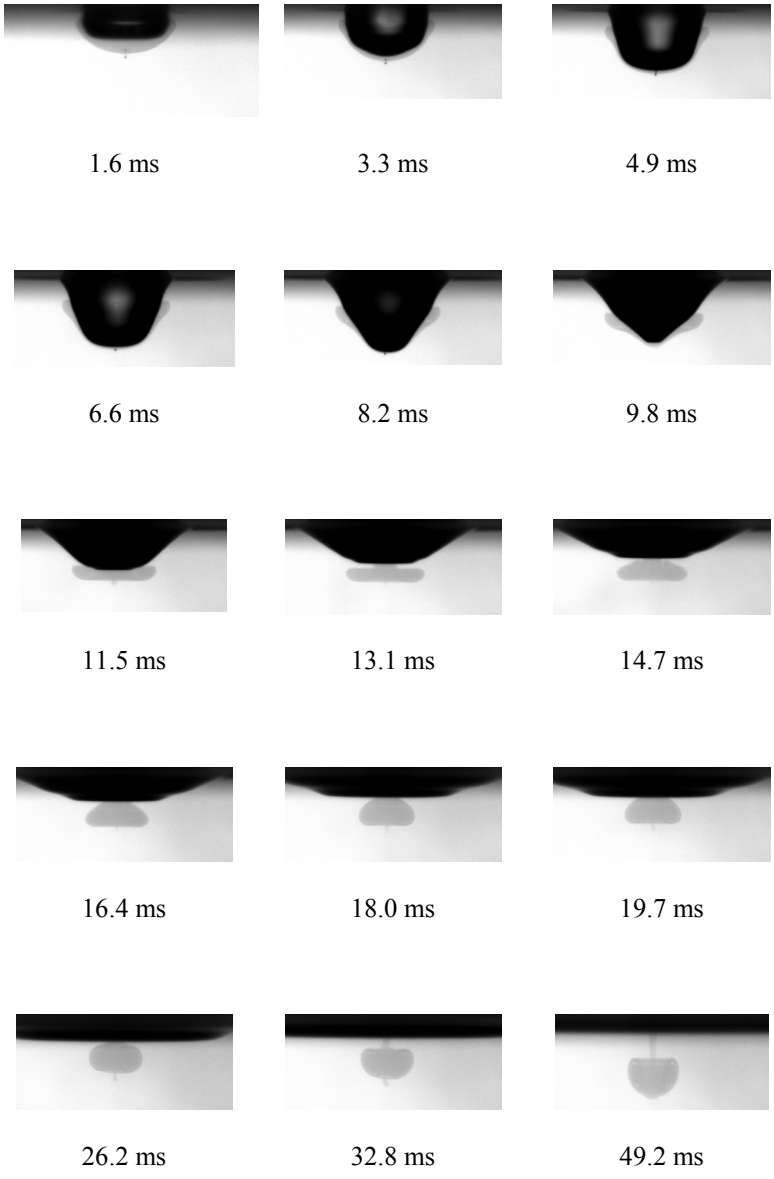

Figure 3.10. (a)

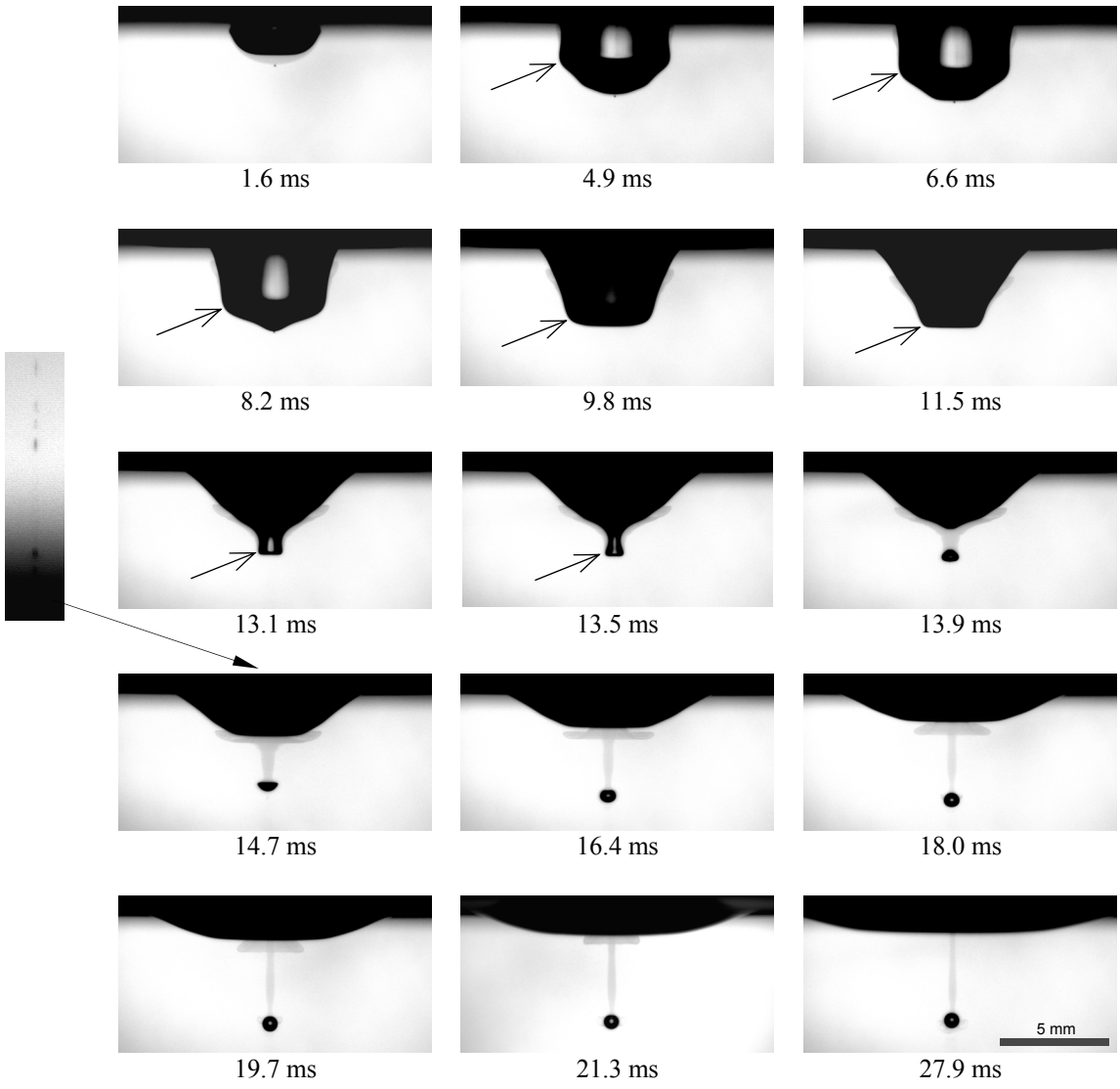
1.6 ms
4.9 ms
6.6 ms
8.2 ms
9.8 ms
11.5 ms
13.1 ms
13.5 ms
13.9 ms
14.7 ms
16.4 ms
18.0 ms
19.7 ms
21.3 ms
27.9 ms
5 mm

Figure 3.10 (b)

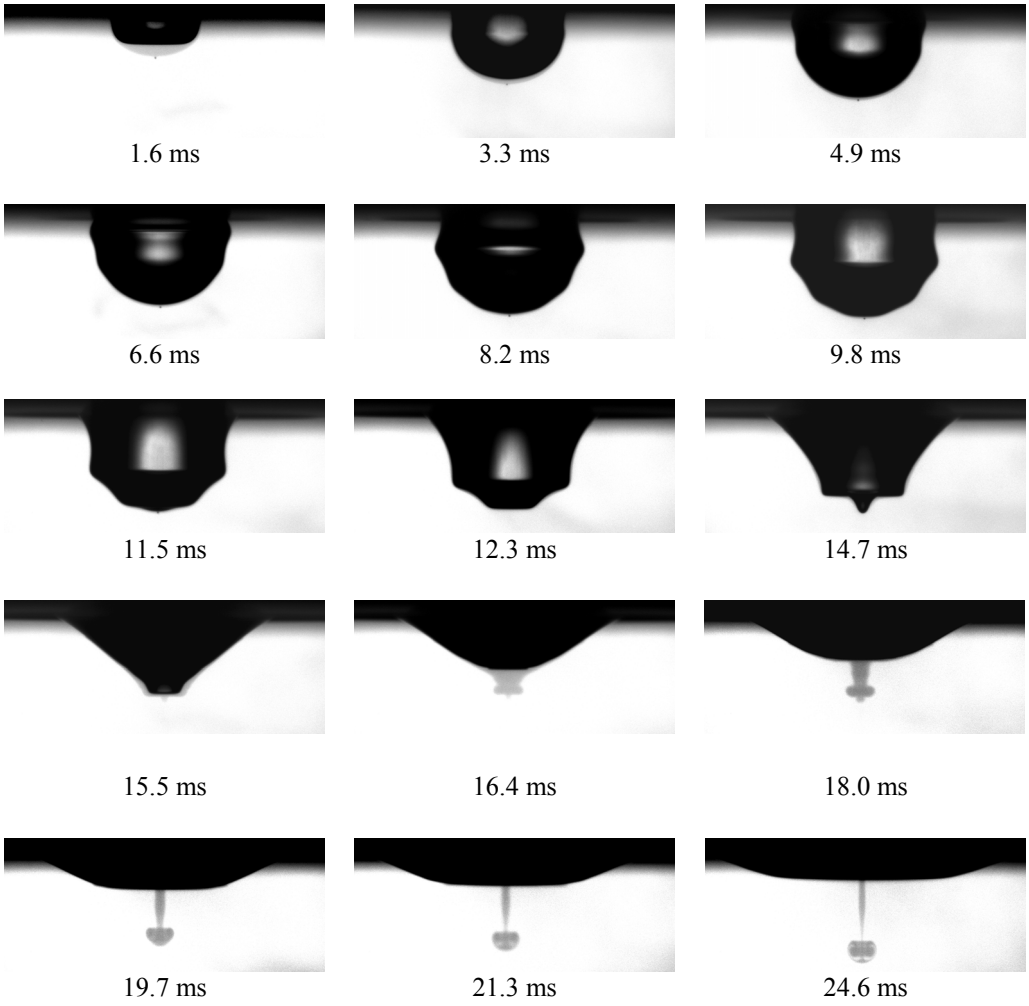

Figure 3.10. (c)

Figure 3.10. Pictures showing crater profile evolution for low viscosity oil drop (0.82 cp) impact onto a deep pool of the same liquid, with the impact parameters (*We, Fr*) located below (a), within (b), and above (c) the regular bubble entrapment regime; sequences 3.10.(a), (b), (c) relate to corresponding *We-Fr* locations in figure 3.9. The experiments have been conducted with 1.5 mm drops and the impact Reynolds number *Re* for the three cases are 1409, 2004, and 2434 respectively.

Viscous drop impact onto the same liquid pool

Previous study with low-viscosity liquid systems has established the importance of the timing of capillary wave arrival in trapping of the bubble. In this section, the role of viscosity on bubble entrapment will be examined; in particular the effect of viscosity on the capillary wave and on the crater rebound dynamics. Glycerin/water (G/W) mixtures of various viscosities have been used to investigate the viscous effect on regular bubble entrapment in drop impact.

Experimental results

The limits *aa', bb', cc'* in figure 3.11.b represent the entrapment boundaries for the 1cp, 5.9cp and 10.2 cp glycerin/water systems respectively. As a general rule, the impact energy requirements for bubble entrapment are higher as the viscosity increases. The detailed crater morphology at the critical moment when the crater tip rebounds, is shown in figure 3.11.a through the picture series A, B, C, with the subscripts '0' representing below, '1' representing inside, and '2' representing above the respective bubble entrapment regimes. The picture series D corresponds to the system with 14.7 cp viscosity, where no bubble entrapment is observed.

From the first group of pictures A_0, B_0, C_0 (figure 3.11.a), which represent impact conditions below the respective regular entrapment limits, the effect of viscosity can clearly be noticed as a damping effect on the amplitude of the traveling capillary wave. From the next group A_1, B_1, C_1 which represent impact conditions within the respective entrapment limits, it is observed that the size of the entrapped bubble decreases as viscosity increases, to the point where there is no entrapment at the highest viscosity of

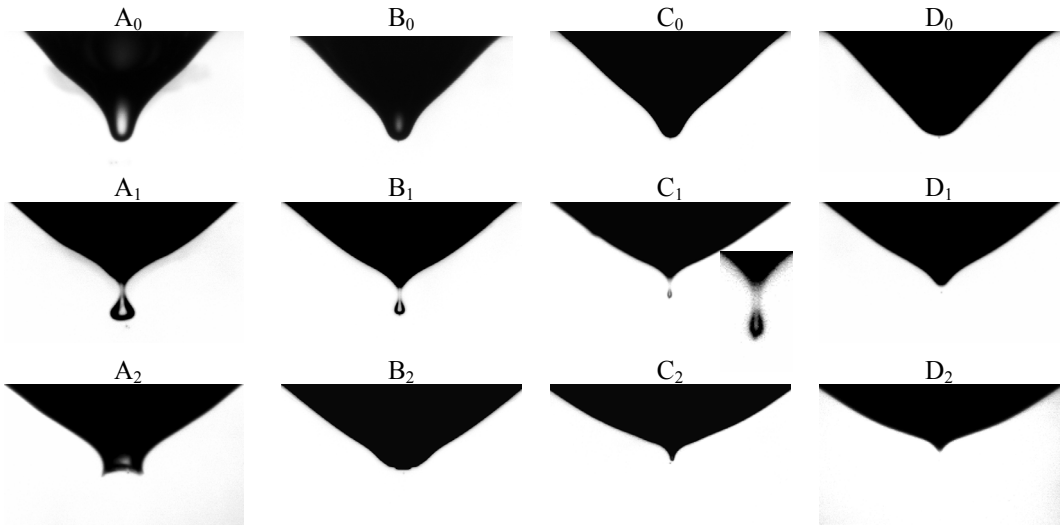

(a)

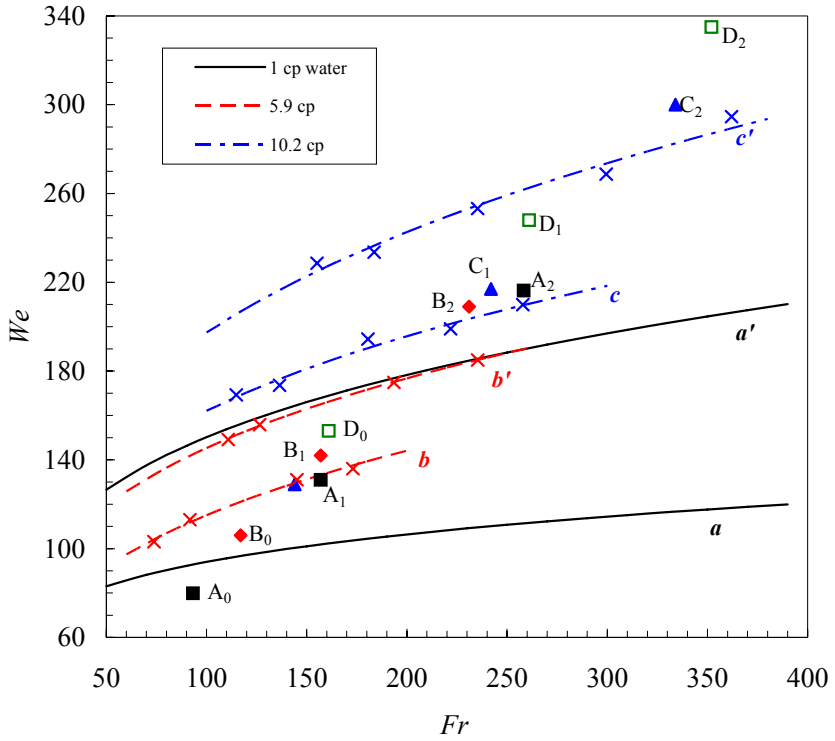

(b)

Figure 3.11. Comparison of the critical crater shapes and entrapment regimes for test liquids with different viscosities using the glycerin/water system. (a) critical crater shapes corresponding to specific locations in figure 3.11.b; subscript '0' represents below, '1' within and '2' above the corresponding entrapment regimes; (b) entrapment regimes *a-a'*, *b-b'*, *c-c'* for systems with viscosities 1cp, 5.9 cp and 10.2 cp respectively.

14.7 cp (picture D_1). This can also be reasoned as a typical damping effect. The third picture series A_2, B_2, C_2 which represent conditions above the respective entrapment limits, shows the crater bottom's dynamics in competition with the capillary pinching. Clearly, in A_2, the low viscosity case, the crater bottom has reversed direction, before capillary crest arrival, thereby, preventing bubble entrapment. Similar effect is seen as the viscosity is increased to 5.9 cp, where the crater is in reversal before capillary pinch off. However, here, the crater base is rounder and the rebound process is weaker. As the viscosity is further increased, the effect of viscous damping is stronger both on the intensity of capillary wave and on the intensity of crater cusp reversal, complicating, but yet preventing, the entrapment process.

Role of viscosity

The global role of viscosity is seen as a change in the lower and upper regular entrapment limits, as shown in figure 3.11.b. In general, the impact energy requirement for bubble entrapment is increased with viscosity. The entrapment limits represent the subtlety of the timing in the bubble entrapment scenario: the capillary crest has to be at the right place at the right time, i.e. before crater reversal. If the sole effect of viscosity is to dampen the capillary ripple, then the entrapment limits should shrink. This appears to be the predominant effect as seen for the 5.9 cp case. However, viscosity also weakens the crater cusp reversal mechanism, to the point where the latter is no longer in competition with capillary pinching. This effect effectively broadens the entrapment regime again, as seen for the 10.2 cp system. In other words, the viscous effect can be interpreted as weakening of the capillary wave, and weakening of the crater reversal

dynamics. The size of the entrapped bubble, however, progressively decreases with viscosity as seen in the A_1, B_1, C_1 picture series of figure 3.11.a. For a viscosity of 14.7 cp, there is no bubble entrapment and the crater reversal process is weakened, resulting in the formation of a thick jet during rebound.

In general, viscosity affects the intensity of both the capillary ripple, responsible for bubble entrapment, and the crater cusp curvature. This indicates that when viscosity plays a role in drop impact, the *Fr-We* combination alone is not sufficient to describe the bubble entrapment phenomenon. In this case, there is a need for an additional dimensionless number that captures the interaction between the capillary ripple and the viscous damping effects.

It is suggested that the dimensionless capillary number:

$$Ca = \frac{\mu V_i}{\sigma} \tag{3.1}$$

can capture this interactive effect.

Figure 3.12 shows the change in entrapped bubble size with capillary number. The diameters of entrapped bubbles were measured directly from the digital pictures. Bubbles, which pinched off from the crater tip and were repeatable in occurrence, were considered as regularly entrapped bubbles in our experiments. Only bubbles greater than 4 pixels (about 0.04 mm) in size were used in our studies, owing to the limitations in optical resolution.

It is noted that the entrapped bubble size varies over a span between the lower and the upper entrapment limits with a peak in the middle; the peak progressively getting less sharp with increasing *Ca*. The results show that the peak bubble size decreases from about 0.98 mm to about 0.19 mm as viscosity increases from 1 cp to 10.2 cp in

glycerin/water system, with the corresponding capillary number varying from *C*a = 0.04 to *Ca* = 0.37. Experiments with 14.7 cp glycerin/water mixture (67% weight percent) show no bubble entrapment in the Weber regime from 98 to 452. Figure 3.12 also includes bubble entrapment data for silicon oil drops, with different viscosities, showing that the capillary number is suitable to characterize the bubble entrapment phenomenon.

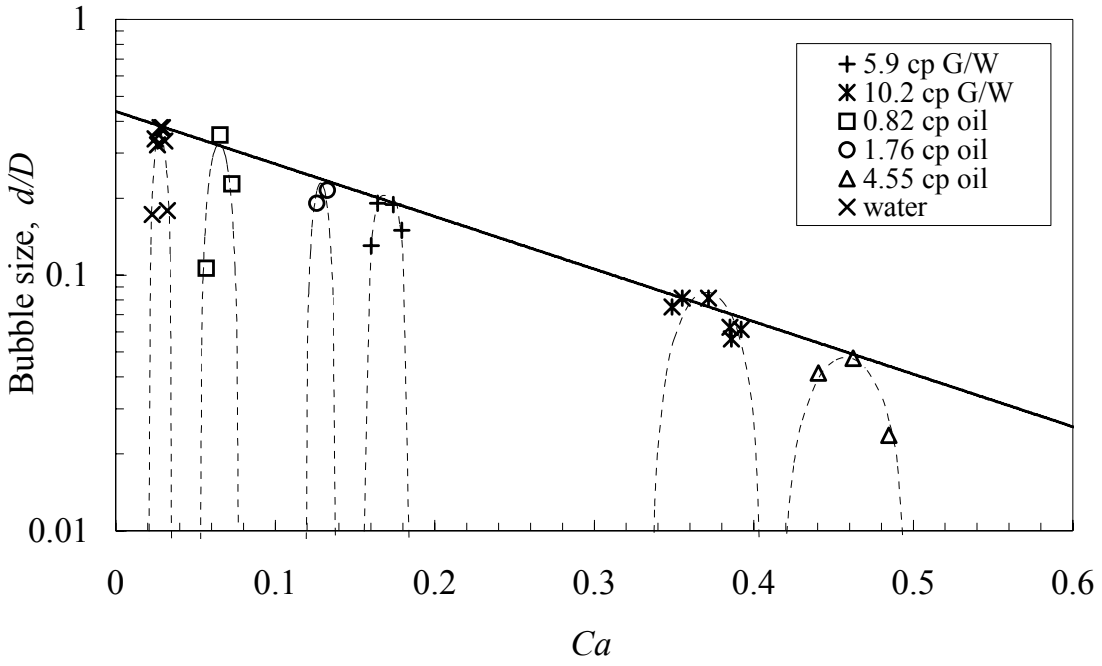

Figure 3.12. Variation of entrapped bubble size, for different drop impact conditions, as a function of capillary number *Ca*.

When viscosity is involved in free surface flow, it sets up a viscous stress that opposes the capillary pressure; the latter being proportional to the curvature of the interface. From Figure 3.11.a (A_1, B_1, C_1) it is seen that the entrapped bubble size is

related to the curvature of the crater tip, right before pinch off. As *Ca* increases, the viscous effect dominates, and the capillary curvature at the cone tip must increase to balance the increased viscous force on the free surface, and thereby, the entrapped bubble size decreases. This trend is clearly shown in figure 3.12. Figure 3.12 also indicates that the cut-off *Ca* number for bubble entrapment is around 0.6. This behavior seems to agree with Jeong and Moffatt's [111] prediction. In their work, they studied the cusp formed between two counter-rotating cylinders below a free surface at low Reynolds (*Re*) number. Their analytical solution suggests that the tip radius of curvature on the line of symmetry decreases as $e^{-32\pi \cdot Ca}$. In the present 3D context, it is reasonable to equate the radius of curvature at the crater tip to the entrapped bubble size, when bubble entrapment occurs. Although the current external flow field is different from Jeong and Moffatt's [111] two dimensional rotating-cylinder case, the measured peak entrapped bubble sizes fit well into an exponential line with *Ca*, as seen by the data in figure 3.12. In our three-dimensional problem, the prefactor of *Ca*, which is 4.7, is much smaller compared to about 100 from Jeong and Moffatt's solution for the two dimensional case.

The viscous effect during the drop impact process can also be examined from an energy standpoint. Generally, there are two effects that need to be considered in this situation. The first is the viscous dissipation in the bulk during crater growth and rebound. The second is the viscous dissipation of the traveling capillary wave along the crater wall.

First, the energy dissipated due to viscosity during the crater growth phase is estimated here. The viscous dissipation energy, W_d, associated with the drop impact crater is given by Engel [92], as:

$$W_d = 8\pi\mu \int_0^t R\left(\frac{dR}{dt}\right)^2 dt \tag{3.2}$$

where μ is the dynamic viscosity, R is the crater depth as a function of time t. Equation 3.2 assumes that the crater grows hemispherically, which is close to the observation. For a water drop 2.5 mm in diameter and impacting at 1.93 m/s, the viscous dissipation energy during crater growth phase is approximately 1.4% of the original kinetic energy of the impacting drop. This indicates that the viscous damping effect on crater formation is negligible, for the low viscosity drop impact system. In other words, the maximum crater depth is not affected by liquid viscosity in the low viscosity range. In fact, when Pumphrey and Elmore [73] and Leng [65] modeled the maximum crater depth by comparing energy transformed in the impacting system, they neglected the viscous dissipation term altogether, and yet got satisfying results.

In the second instance, for the role of viscosity in drop impact, viscosity can dampen the capillary wave energy and thereby weaken the entrapment process. If viscosity has significantly dampened the capillary wave before crater grows to maximum depth, then bubble pinch-off should not happen. On the other hand, if the viscous effect on the capillary wave is not strong, then bubble entrapment may happen. Here, the viscous effect can be evaluated by the damping time constant τ. A requirement for bubble entrapment occurring could be expressed as:

$$t_{c\max} < \tau \tag{3.3}$$

t_{cmax} is the crater growth time evaluated from drop-bulk initial contact to the moment when crater reaches its maximum depth. Since crater growth is a process through which the kinetic energy from the impacting drop transfers into potential energy stored in the crater, t_{cmax} should be related to the impacting kinetic energy. The viscous damping time constant τ for capillary surface waves is given as [112]:

$$\tau = \lambda^2 / 8\pi^2 \nu \tag{3.4}$$

where λ is the capillary wave length, and ν is the kinematic viscosity of the liquid. This expression is valid for all the drop viscosities used in our experiments [112,113].

Using this equation to estimate the viscous effect on the traveling capillary wave, and by taking $\lambda \sim D$ = 2.5mm, one can calculate a viscous dissipation time constant τ = 79 ms for the 2.5 mm water drop impact (ν = 1.0 cs). From the current experiments, $t_{c\max}$ ranges from about 13 ms to 18 ms for all cases of a 2.5 mm water drop impact, within the regular entrapment regime. This suggests that viscous dissipation of the capillary wave is not dominant before bubble pinch off in the low viscosity water system. However, if the liquid is 67% glycerin/water mixture, the corresponding kinematic viscosity is increased to 12.6 times that of water's, and the corresponding dissipation time scale τ becomes 6.3 ms. Since the overall crater formation process is negligibly affected by the viscosity increase, as the impact energy is proportionately increased, $t_{c\max}$ still remains within 13 ms to 18 ms. Thus, for the 12.6 cs glycerin/water case, τ is less than $t_{c\max}$, implying that viscosity will damp out the capillary wave and thereby suppress bubble entrapment.

Critical cone angle

As reported in the literature, and confirmed by our experiments, the phenomenon of regular bubble entrapment is always associated with a conical crater shape and a high rising thin jet. The gravitational potential-induced crater shape recovery starts when the impact crater reaches its maximum depth (figure 3.10.b). During the recovery, the sidewall slope decreases with time, thereby, indicating that there is a radial inward velocity component in the bulk flow which is progressively stronger at the crater bottom.

From the picture series A_1, B_1, C_1 of figure 3.12.a, it is seen that the cone-shaped crater profiles take on an hour glass shape at the bottom, just before bubble pinch off. This shape is a direct consequence of the timely arrival of the capillary ripple at the crater bottom, which sets up the conditions for bubble entrapment. The capillary crest facilitates the radial focusing of the bulk flow, leading to the dual events of bubble pinch-off and high speed thin jet formation. In this sense, the focusing of the bulk flow, which follows the shape disturbance of the capillary ripple, appears to be different from pure inertial focusing as observed by Bergmann *et al.*[82].

Longuet-Higgins' [78,79] analytical model predicts that there is a critical cone angle associated with the so-called conical flow. He pointed out that when the crater cone reaches this critical cone angle, the global velocity and acceleration fields tend to infinity as $t^{-1/3}$ and $t^{-4/3}$ respectively. This model does not include the surface tension term, so it cannot predict the bubble entrapment event as seen in the experiments. However, since the bulk flow diverges at the critical cone angle of 109.5°, the bubble pinch-off, which is the local phenomenon, will most probably occur at this point.

In figure 3.13, the cone angles measured at the moment of bubble pinch-off, for different test fluids have been plotted as a function of the capillary number. The critical cone angle has been determined by measuring the slopes of the straight lines connecting the pinch-off point to the cone base, as shown in the inserts of figure 3.13. The data spread for each liquid system represents the traverse from the lower entrapment limit to the upper entrapment limit, with the bubble size showing a peak in the middle. The dotted line connects the critical cone angle data, corresponding to peak bubble entrapment, for different liquid systems. The arrows represent the data points

corresponding to pictures A_1, B_1, C_1 in figure 3.11.a. From figure 3.13, it is apparent that the critical cone angle for peak bubble entrapment varies weakly with the capillary number, and in the inviscid limit (low *Ca*) it agrees well with Longuet-Higgins' prediction.

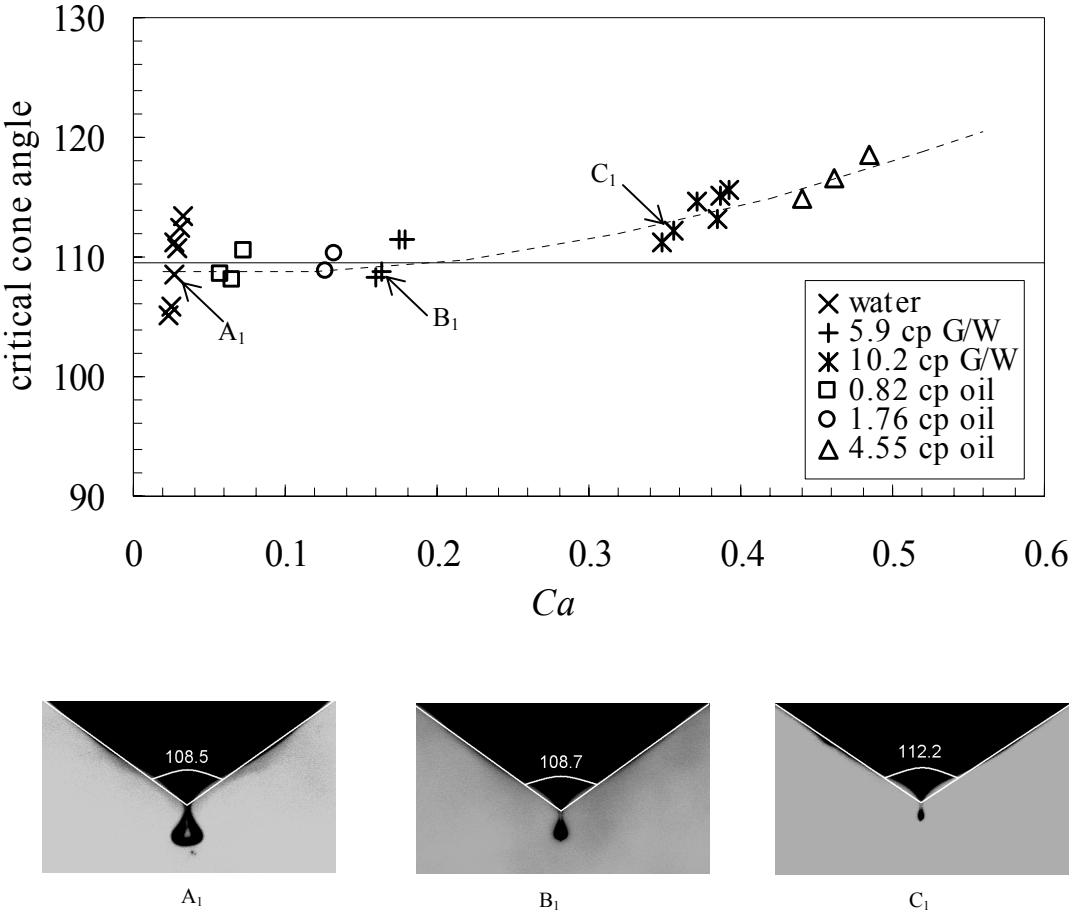

Figure 3.13. Variation of critical cone angle, measured right at the moment of bubble pinch-off, as a function of capillary number *Ca*. The solid line represents the critical cone angle prediction of Longuet-Higgins [78,79]. Data points A_1, B_1, C_1 correspond to the respective crater profiles of figure 3.12.a (inserts show the critical cone angle measurement).

Power law singularity of the thin jet

Figure 3.14 shows the evolution of a high rising thin jet, following bubble pinch-off, for a 5.9 cp glycerin/water drop impact. The labeled time for the individual pictures of figure 3.14 corresponds to the elapsed time following the moment of bubble pinch-off. In the first picture the thin jet is visible above the crater rim, 1.1 ms after crater collapse. At that time the jet is very thin, and the Rayleigh capillary instability disintegrates the upper portion of the jet into minute droplets. The speed of the jet is so high that the droplet image is blurred despite a short exposure time of 50μs. From this picture, it is estimated that the jet upward velocity is about 15 m/s. As time elapses, the major part of thin jet grows thicker and taller, and the upper portion of the jet develops a corrugated profile but does not pinch off into droplets. Later, as gravity effect dominates, the jet stops growing in vertical *z* direction, and finally collapses onto the equilibrium surface.

The high speed thin jet is the consequence of the high pressure stagnation resulting from the radial focusing of the bulk flow during bubble pinch-off. By characterizing the jet's growth profiles, using power law scaling, one could potentially derive useful information about the dynamics of the bulk flow at the pinch-off moment. Here, the jet profiles for the short time regime (t < 10 ms) have been analyzed, where gravity has a very minimal role in the growth of the thin jet ($1/2gt^2/h << 1$; h : height of the jet). Further, only the undistorted side wall profile of the jet has been examined, and the tip which is strongly affected by the capillary instability was excluded from data analysis.

The construction of the fitting function for the jet profile has been motivated by the general solution form for the kinetic free surface problem: $z = at^{\lambda}(rt^{\eta})^{\nu}$, derived by Hogrefe et al.[81]. Here *z* and *r* are the coordinates of a point located on the jet side wall

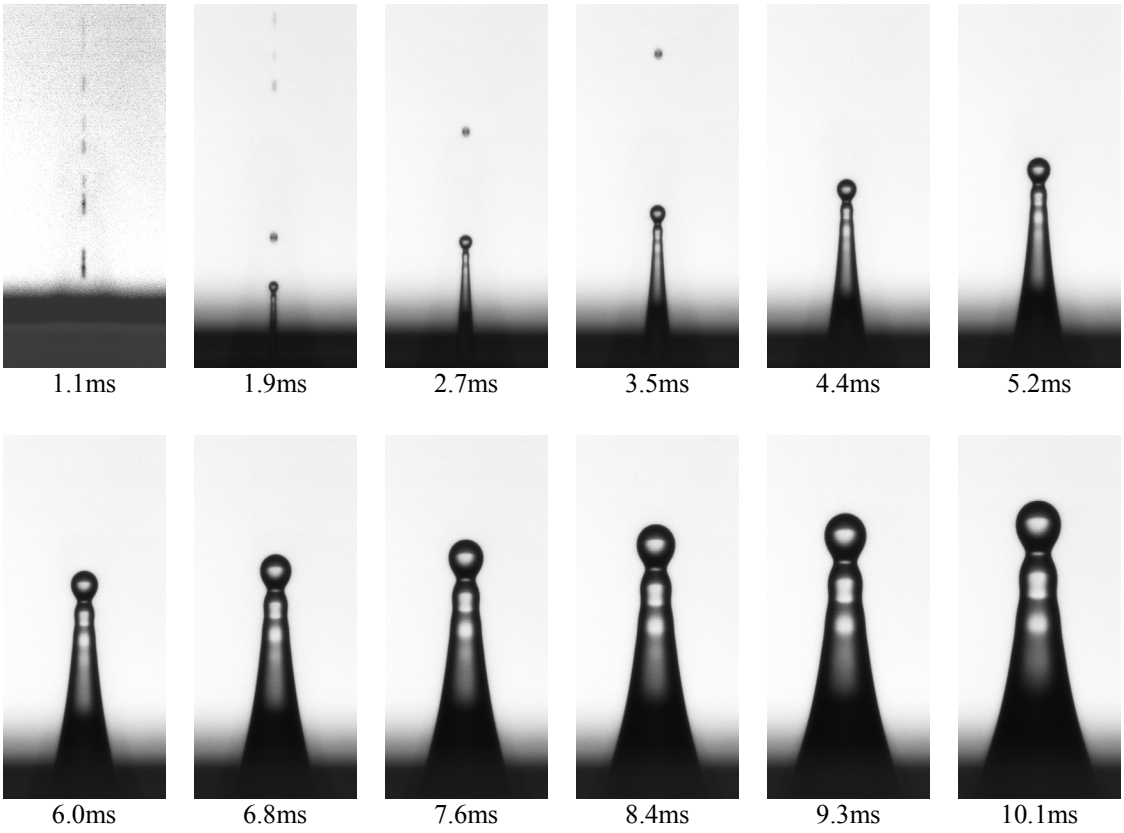

Figure 3.14. Pictures showing the high-speed thin jet and the main body of the reversed flow following bubble entrapment, during the impact of a 5.9 cp glycerin-water drop at *We*=117, *Fr*=68 (refer figure 3.11.b). Time label shows the elapsed time following bubble pinch-off.

in a cylindrical coordinate system, originating at the bubble pinch-off point. The original frame analysis data (z, r, t) has been non-dimensionalized (z^*, r^*, t^*) by scaling z and r with D, and t with D/V. For convenience, the objective fitting function is defined as:

$$z^* = b t^{*\alpha} r^{*\beta} \tag{3.5}$$

The nonlinear data regression has been done on *Polymath* software. If the fitting is good, then the data points of $(z^*/t^{*\alpha}, r^*)$ should collapse into one power law curve of the form $z^*/t^{*\alpha} = br^{*\beta}$. This is shown by the main portion of figure 3.15. The inserts in figure 3.15 represent the original *r* and *z* coordinates, obtained from the sequence of selected pictures shown in figure 3.14. The fitting constants, α and β shown in figure 3.15 are 0.656 and -0.435 for the 5.9 cp glycerin/water jet. The same fitting process has been implemented for data from water and 10.2 cp glycerin/water jets. The corresponding α and β values are 0.613 and -0.432 for water jet, 0.686 and -0.540 for the 10.2 cp glycerin/water jet. The jet analysis data does not show any strong effects of viscosity on α, for viscosities up to 10.2 cp.

According to Equation 3.5, the vertical velocity and acceleration at the jet surface can be scaled as:

$$\dot{z}^* \sim t^{*\alpha-1} \qquad \ddot{z}^* \sim t^{*\alpha-2} \tag{3.6}$$

In the case of α = 0.656, the velocity scales as $t^{*-0.344}$ and the acceleration scales as $t^{*-1.344}$. Consequently, at the time of origin, which is the pinch-off moment, both velocity and acceleration tend to approach infinity. This implies singularity on the jet profile, as proved by the exceptionally high upward speed of the jet (figure 3.14, *t* = 1.1 ms). The degree of singularity can be evaluated by the α value. Considering α is positive and smaller than 1, at time very close to collapse (*t* = 0+), the velocity is higher for smaller α (Equation 3.6), which indicates higher degree of singularity for the smaller α values.

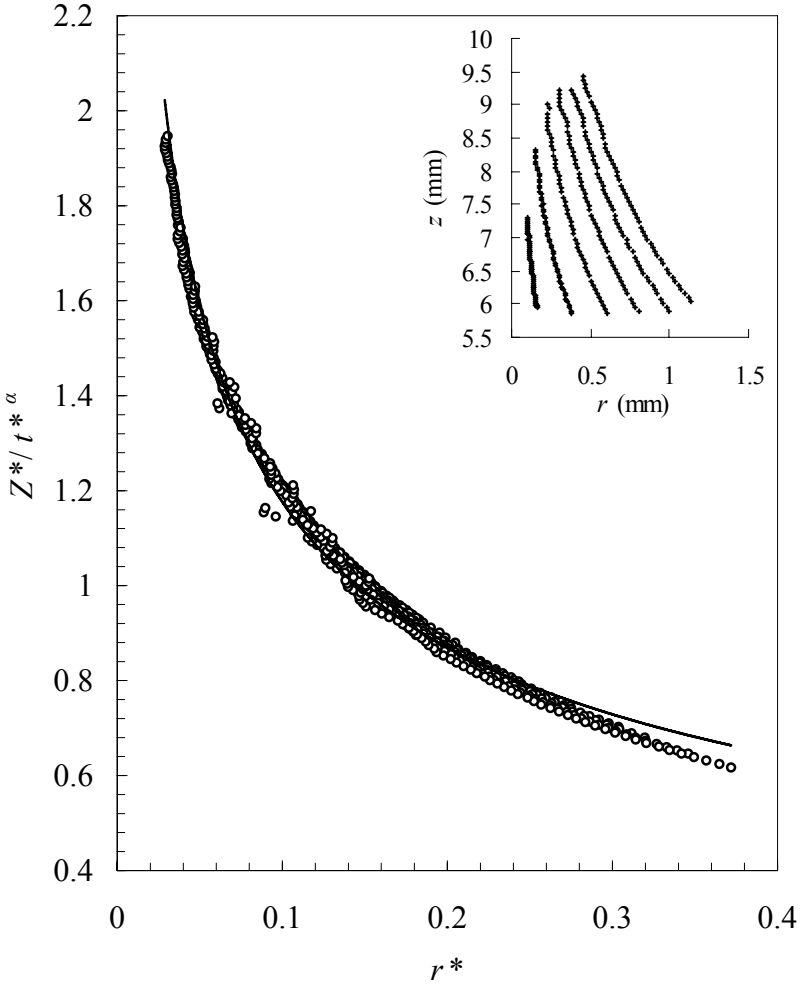

Figure 3.15. Plot showing a sequence of jet profiles collapsing into a power law curve of the form: $z^* / t^{*\alpha} \sim r^{*\beta}$, for 5.9 cp glycerin/water jet $\alpha = 0.656$ and $\beta = -0.435$. The insert plot represents outlines of the jet extracted from pictures shown in figure 3.15, with the far left curve corresponding to $t = 2.7$ ms; the time interval between consecutive curves is 1.64 ± 0.04 ms.

The power law scale of singularity for the jet profile has been reported for a wide range of free surface flows, when the surface flow collapses at a certain point. It is valid for the hydraulic free surface jets arising under conditions such as overdriven standing wave [81], for cavity collapse inside a liquid body [114] and for onset of an

electrohydrodynamic spout [115], with the α values varying between 0.4 and 0.667 in these different situations. Figure 3.16 shows the temporal growth of the thin jet from the current experiments, with the slope of each data set representing the constant α. It appears that the experimental fitting constant α in each case is very close to the theoretical prediction of α= 2/3 by Zeff *et al.* [80].

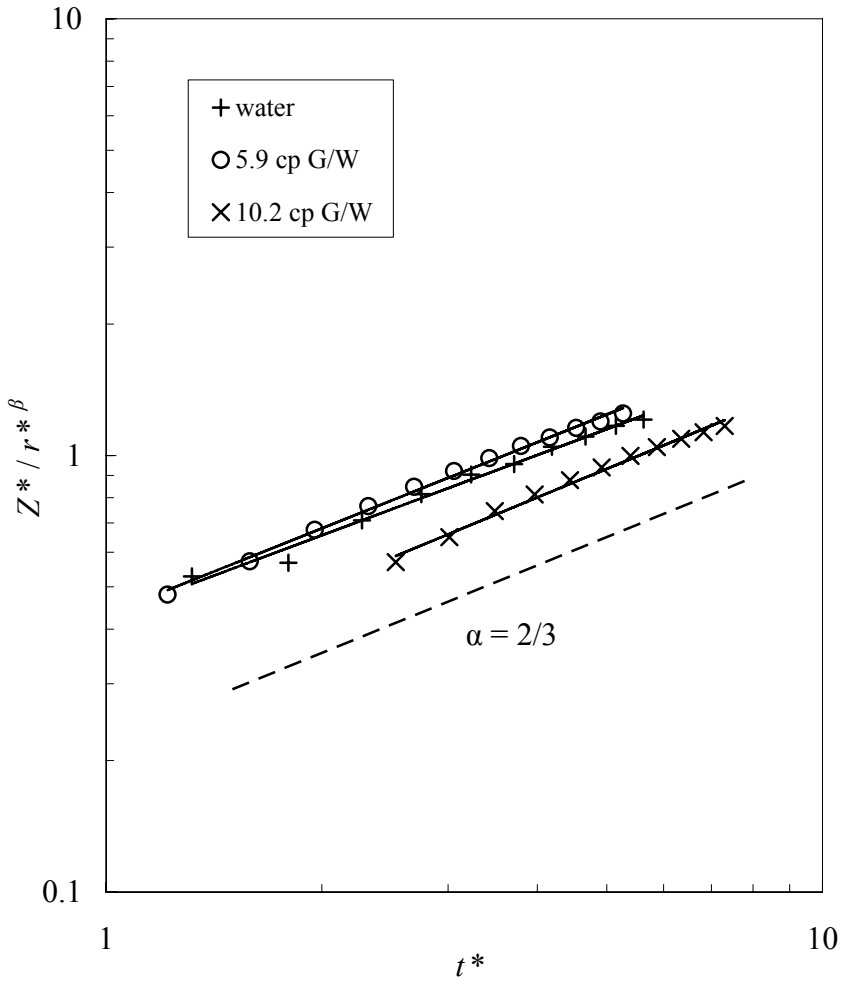

Figure 3.16. Plot showing the temporal growth of jet profiles for three different thin jets. The solid lines are the best fit lines for each data set; the dashed line is a visual guide with exponential constant $\alpha = 2/3$.

Asymmetric drop impact phenomenon

The study of the phenomenon of liquid drop impact onto a deep pool of the same liquid has shown that viscosity can damp out the traveling capillary wave and hence suppress bubble entrapment. Before studying the bubble entrapment issues in chemically reacting drop impact, a series of asymmetric drop impact experiments were carried out. The asymmetry here refers to the situation where the drop liquid and the pool liquid are of different viscosities; with the drop viscosity being generally higher. The primary objective of these transitional studies is not the local issues of miscibility and diffusivity, which can arise in such asymmetric systems, but the examination of the physical processes responsible for bubble entrapment using a global perspective.

For the asymmetric drop impact experiments, the drop and pool liquids were selected from different weight ratio of glycerin and water, and different viscosity grades of silicon oils. First, the low viscosity regime (μ < 30cp) has been examined, where the regular bubble entrapment (ripple induced bubble pinching) is expected to happen. Figure 3.17 shows a typical crater evolution for impact of a 14.7 cp G/W drop impact onto water pool. Generally, the crater formation is similar to the low viscosity symmetric liquid drop impact system, including the presence of the traveling capillary ripple. During the initial growth of the crater, the drop liquid spreads all over the crater wall as a thin layer, and is not visible in the pictures. The initial spread of the drop liquid may facilitate the mixing of the two liquids, which complicates the problem. After t=16.4 ms, the drop liquid starts to accumulate itself again at the crater bottom, and the drop-pool liquid interface can be tracked, without need for dye, owing to the difference in refractive index between the two liquids. The crater shape at the moment of bubble pinching appears very similar to the

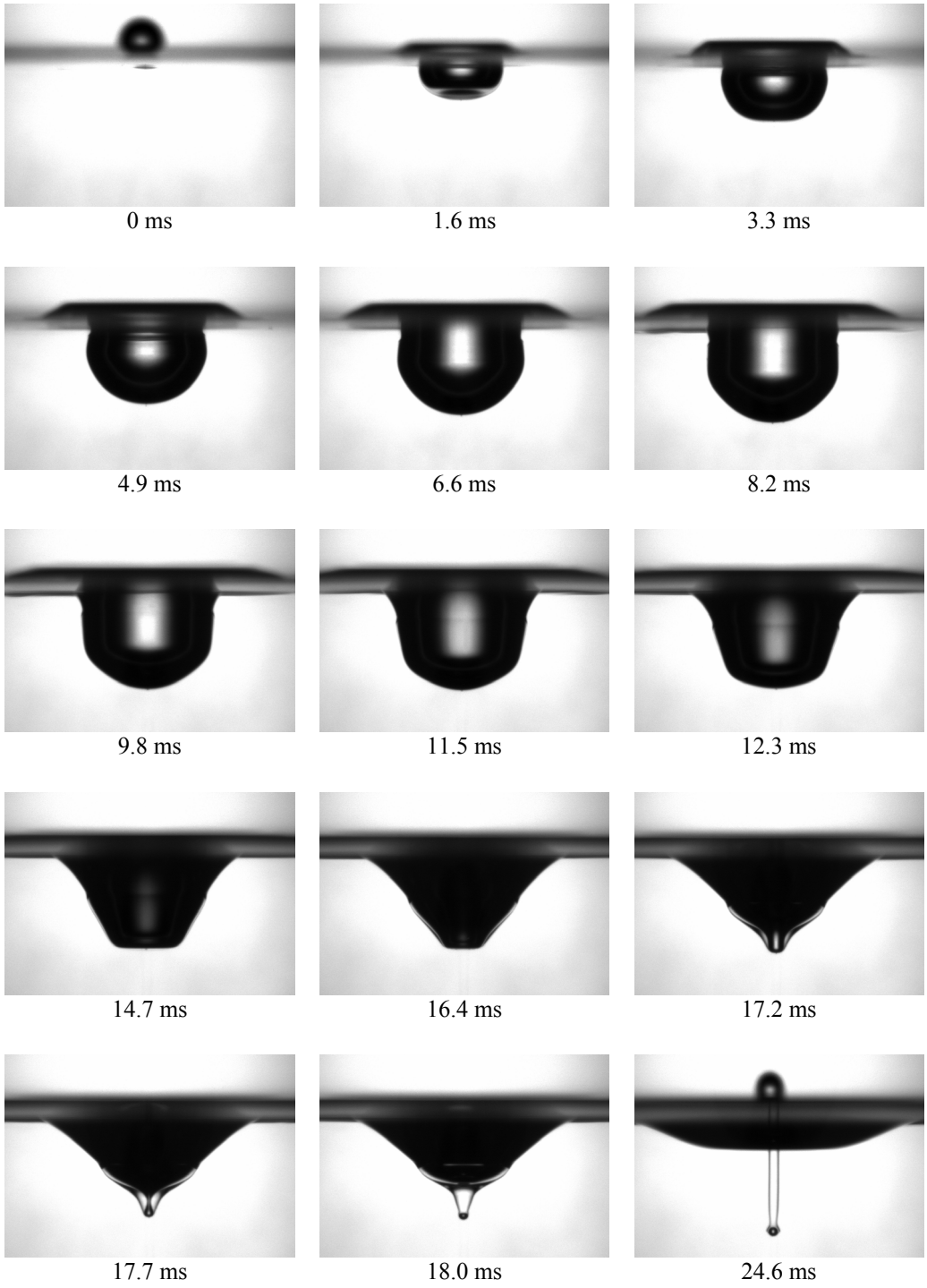

Figure 3.17. Pictures showing a typical sequence of crater formation and collapse following the impact of a 14.7 cp G/W drop impact onto a water pool (We_d= 190, Fr_d= 218).

case of simple (symmetric)drop impact system. As in symmetric drop impact, the regular bubble entrapment for asymmetric system also occurs in a limited regime, although the boundaries of this regime move according to the combinational properties of both drop and pool liquids (see figure 3.18).

The liquid property, in particular the viscosity around the crater wall, which governs bubble-pinching, must have an intermediate value between the drop and pool liquid as both liquids seem to participate in the entrapment process. When it comes to data analysis, an important question to answer is which fluid properties (drop or pool) should be used in *Fr*, *We*, and *Ca* estimation? A possible approach is to use either the mean value or the square root average value as the liquid system's material property. This can be expressed as $\sigma=(\sigma_d+\sigma_p)/2$, $\mu=(\mu_d+\mu_p)/2$, or $\sigma=(\sigma_d \cdot \sigma_p)^{1/2}$, $\mu=(\mu_d \cdot \mu_p)^{1/2}$, where subscript *d* refers to the drop and *p* refers to the pool liquid. In figure 3.19 (a) and (b), the maximum entrapped bubble size from all the regular bubble entrapment experiments are plotted against the modified *Ca*. It appears that the square root average may provide a better fit for the viscous damping versus bubble size data, as seen in figure 3.19.b. Figure 3.19 also suggests that the bubble entrapment in asymmetric drop impact system still depends closely on viscosity as represented by *Ca*. When the drop viscosity is increased to 30 cp while keeping the pool at 1 cp, no bubble entrapment is observed in all the kinetic energy range.

(a)

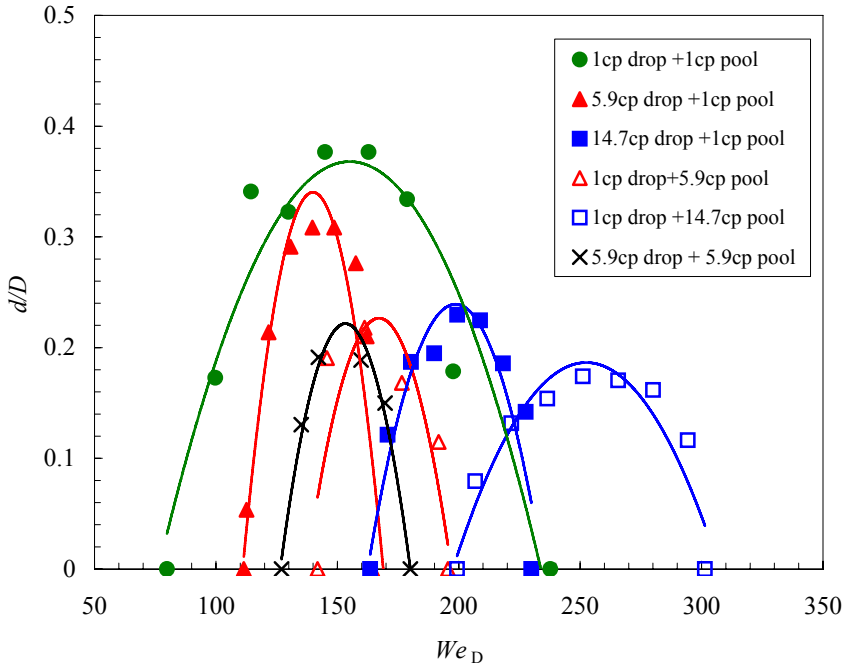

(b)

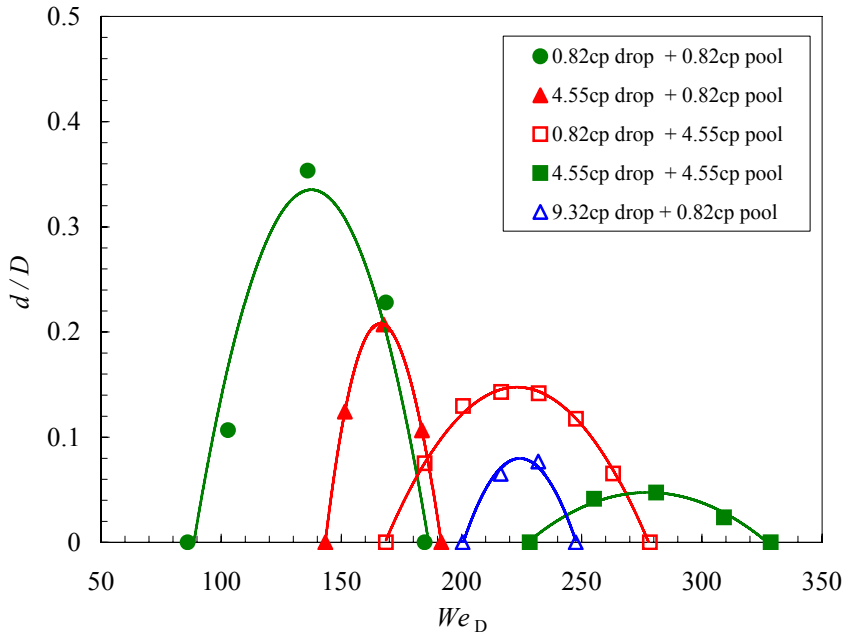

Figure 3.18. Entrapped bubble size plotted against *We* (determined by drop liquid properties). Data points are from asymmetric drop impact experiments with glycerin water system (a), and silicon oil system (b).

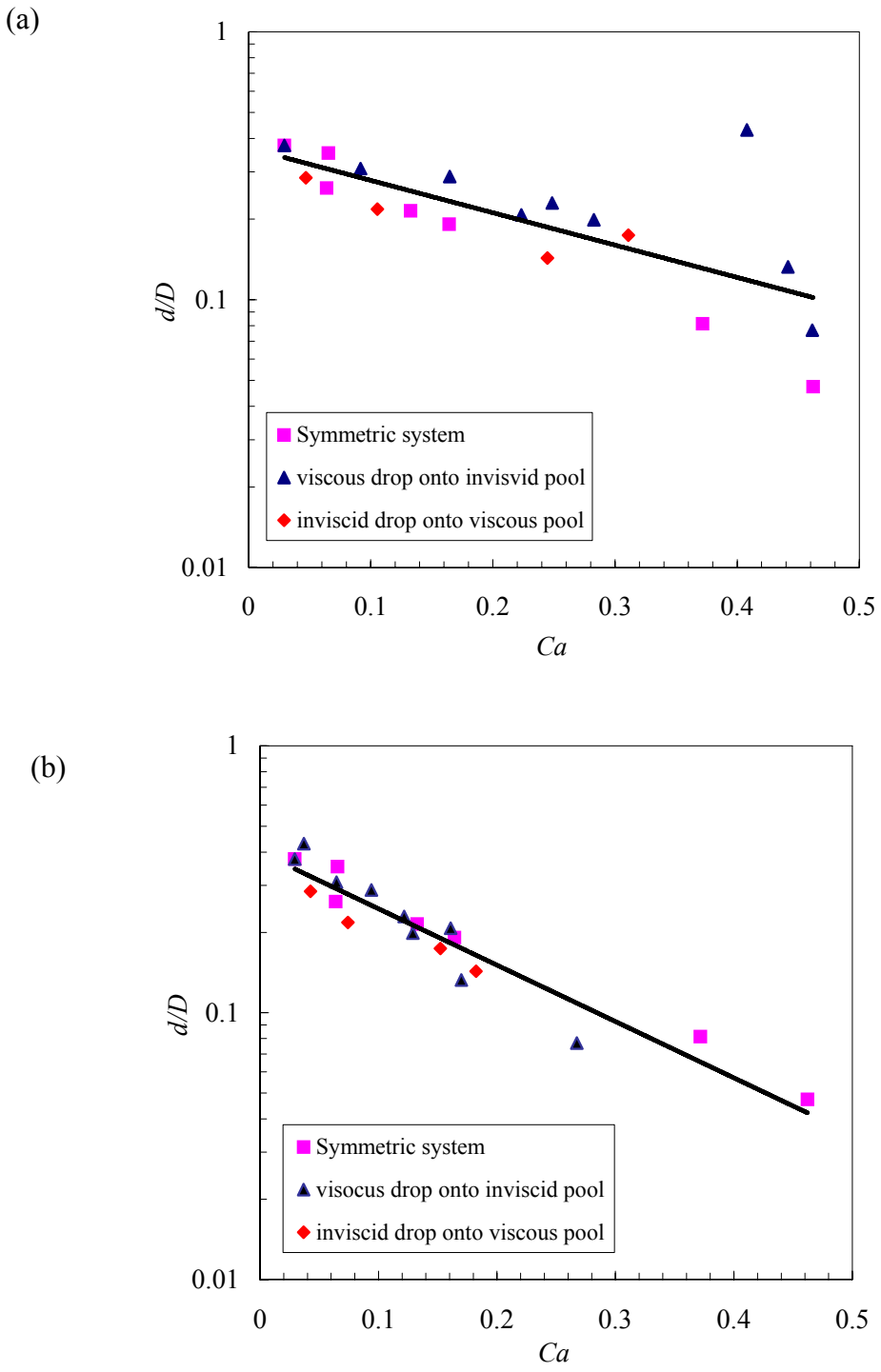

Figure 3.19. Entrapped bubble size plotted against the impact capillary number, determined by (a) mean and (b) square root average of the properties of drop and pool liquids. Solid line is the exponential fit for the data from both symmetric and asymmetric systems.

Figure 3.20 shows the measurements of the critical cone angle as a function of capillary number for asymmetric drop impact, when bubble entrapment occurs, in glycerin/water systems. The different data sets have been obtained by changing the viscosity of the liquid (drop and/or pool), and the *Ca* increases as viscosity increases. Generally, the critical cone angle value does not vary much from 109.5^{o}, the value for the inviscid system. For the cases of viscous G/W drop impact onto water, the angle appears a little lower than the symmetric system, yet finally it approaches 109.5^{0} as *Ca* increases. The decrease of cone angle may be related to the fact that the crater bottom, prior to entrapment (figure 3.17), is surrounded by the more viscous drop liquid, in the form of a vortex, which will result in stretching the crater bottom. Eventually, as the impacting drop viscosity becomes very high, approaching infinity as in the case of a solid bead, the entire bulk flow is above the drop and the pinching occurs above the drop, which hardly spreads. Here, with the focusing of the inviscid pool liquid above the drop, the critical cone angle of 109.5^{o} is again observed at high *Ca*, as seen as the dotted line in figure 3.20. Also, there is no capillary wave presence or involvement with the pinching process here.

For the opposite scenario, when water impact impacts onto a viscous G/W pool, the critical cone angle is a slightly higher than symmetric situations in the low *Ca* regime, probably due to the weaker vortex stretching effect. The crater is shallower and wider as pool viscosity increases, thereby higher critical cone angle is observed as *Ca* increases. The overall trend of the critical cone angle in this case is to approach 180^{o} as *Ca* (or pool viscosity) becomes infinity, which corresponds to the scenario of a liquid drop impacting onto a solid surface.

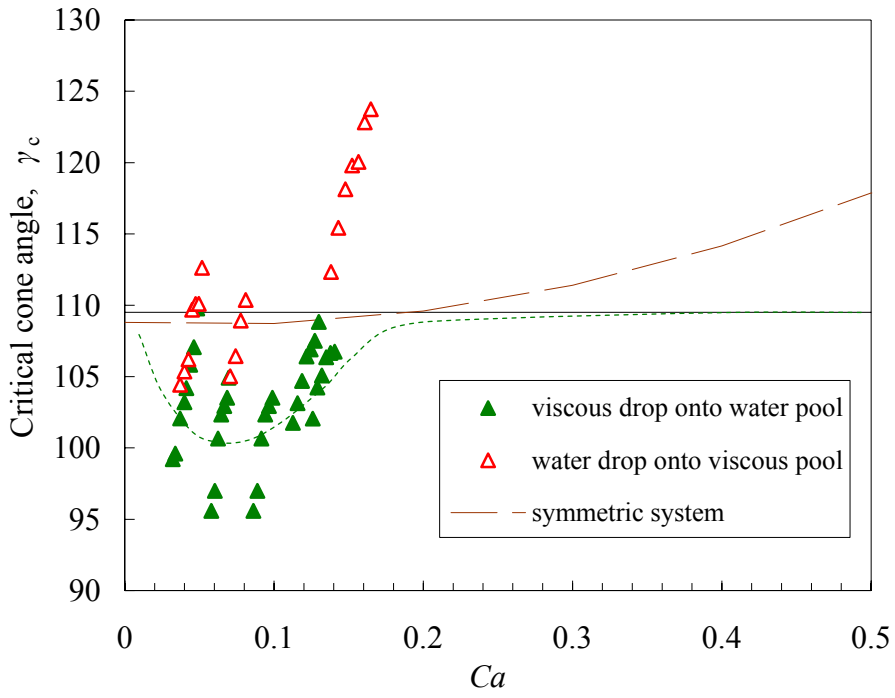

Figure 3.20. Critical cone angle for asymmetric drop impact system as a function of *Ca* (determined by square root average properties of drop and pool).

To further investigate the asymmetric drop impact problem in a wider viscosity range, the drop viscosity was changed from 1 cp to 200 cp and higher, till the extreme case of a solid sphere, while keeping the pool liquid always water. Here, the drop size varied slightly in the range of 2.28 to 2.5 mm, and the velocity range is 0.9 to 3.6 m/s. In figure 3.21 all the data points of entrapped bubble size are plotted against the viscosity ratio of the drop to the pool liquid. Apparently, there exist two regimes of bubble entrapment, separated by a no-entrapment zone. The first bubble entrapment regime has been discussed above, where the bubble entrapment mechanism is similar to the symmetric drop impact problem, and is a traveling capillary wave enabled phenomenon. As the drop viscosity increases, the capillary wave is dampened so that the entrapped bubble size continuously decreases. To the limit of viscosity ratio near to about 30, the

traveling wave is totally damped out and no regular bubble entrapment occurs, no matter the impacting kinetic condition. However, when a 161 cp glycerin/water drop is the impact object, the bubble entrapment emerges, again located at the base of impacting crater, see insert (b) of figure 3.21. The picture sequence of this asymmetric drop impact is shown in figure 3.22. Here the crater walls are smoother, showing no capillary wave involvement. The drop liquid spreads, and forms a circular vortex while re-aggregating at the crater bottom. This miscibility complicates the overall crater morphology. The crater side wall does not form a cone shape during retraction as in regular bubble entrapment, and the bottom of the crater already reverses (since t = 11.9 ms) its direction during bubble pinch-off. In case of pure glycerin drop being used as drop liquid, bubble entrapment similar to that in figure 3.21.b is observed. When a plastic sphere is used as impact object, the crater also collapses above the top surface of the sphere, leaving a very small bubble entrapped. Here again, at the moment of bubble pinching, the crater represents a cone shape with cone angle close to 109.5^{o}, in agreement with the trend shown in figure 3.20 (dotted line). In all these bubble entrapment cases at higher drop viscosity, no traveling capillary wave development prior to the pinch-off was observed. It is proposed this bubble entrapment is solely due to the focusing of bulk flow during the crater collapse, and drop liquid itself serves as a high flow impedance region with the surface collapse occurring above the drop.

In cell encapsulation experiments, the drop/pool viscosity ratio increases greatly as the gelling reaction proceeds during the impact, and this can easily put the parametric condition in the second bubble entrapment regime of figure 3.21. Thus it is reasonable to expect that the bubble entrapment observed in encapsulation process probably is similar

to that of the solid bead case of figure 3.21.c; in contrast with the classical *low viscosity bubble entrapment* caused by capillary ripples. This phenomenon will be a major focus of the next chapter.

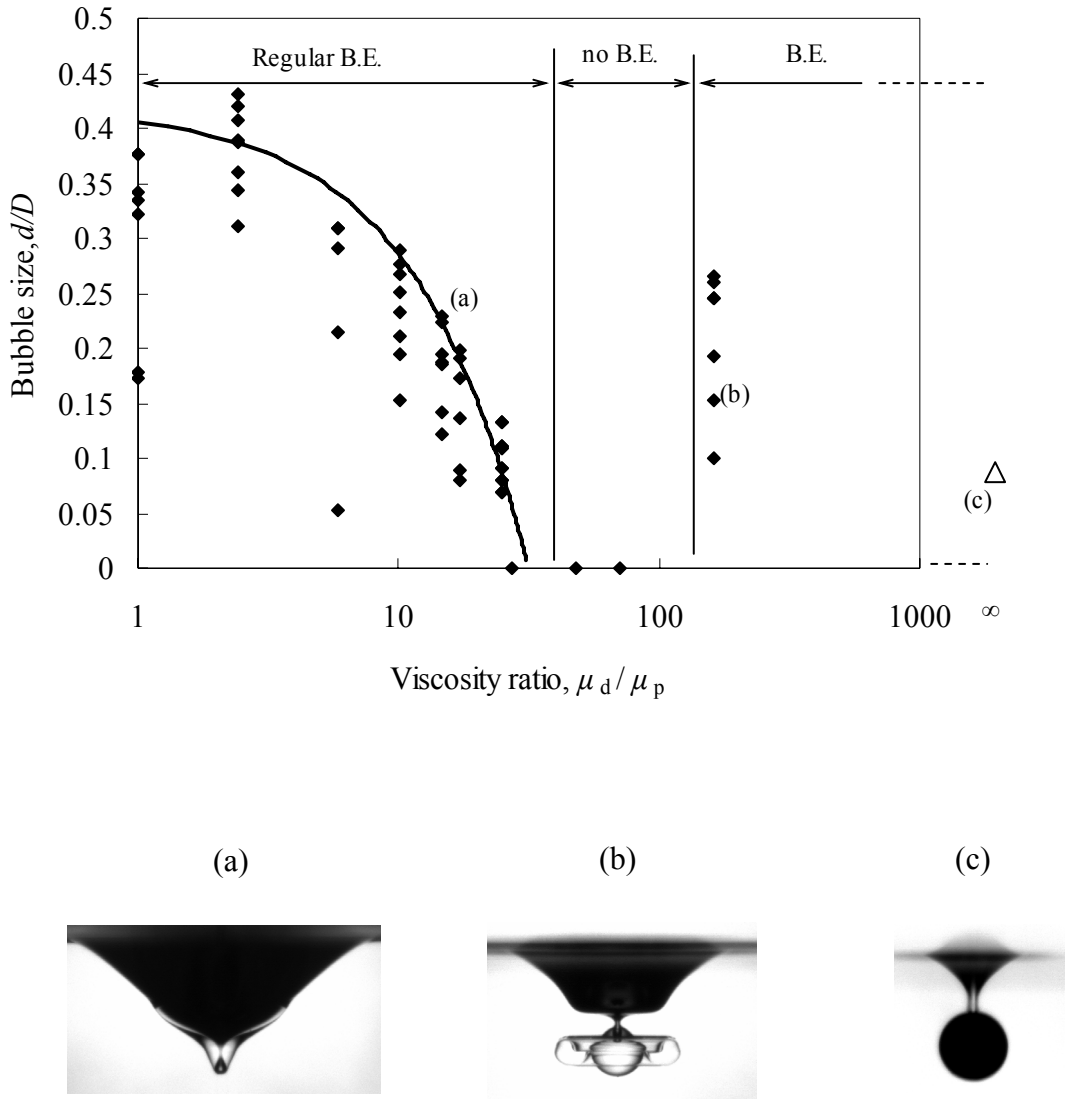

Figure 3.21. Plot showing two different regimes of bubble entrapment established by asymmetric drop (viscous drop onto water pool) impact experiments. The inserts show three snapshots of critical crater shape immediately prior to bubble pinch-off for: (a) 14.7 cp G/W drop impact onto water, (b) 161 cp G/W impact onto water, and (c) solid sphere impact onto water, respectively.

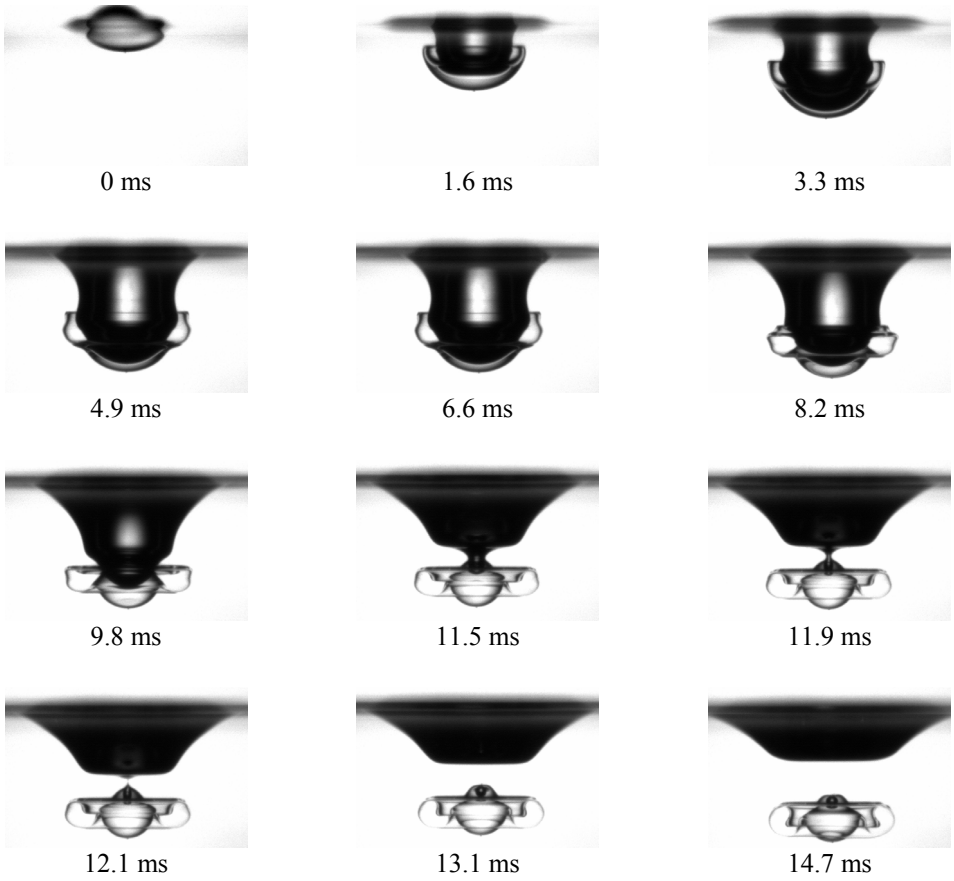

Figure 3.22. Pictures showing a sequence of crater formation and collapse following the impact of a 161 cp G/W drop impact onto a water pool (We_d= 122.3, Fr_d= 133.7).

Conclusions

In this chapter, the details of the bubble entrapment and associated crater signatures observed during drop impact onto the deep liquid pool in absence of chemical reaction have been examined. In order to obtain a complete understanding of the physical mechanism of bubble entrapment, experiments in a wide parametric range were carried out to study the individual effect of impact velocity, surface tension and viscosity. The experimental result from inviscid liquids of both low and high surface tension verifies the classical regular bubble entrapment limits in *We-Fr* plane. This suggests that the regular bubble entrapment in inviscid system results from the interplay between inertia and surface tension only. The photographic study shows that bubble entrapment depends on the timely arrival of the traveling capillary wave at the bottom of the impacting crater bottom during its concentric collapse.

The event of regular bubble entrapment is found to be very sensitive to the liquid system's viscosity. Globally, the classical inviscid entrapment limits are shifted with viscosity, implying a stronger impact energy requirement for entrapment. Locally, the capillary wave crests are weakened by viscous damping so much so that the peak entrapped bubble size progressively decreases with viscosity. Since the capillary wave is surface tension-based, and the damping is viscosity based, the effect is well captured by an additional dimensionless number, the capillary number. As the capillary number increases, the peak impact bubble size decreases exponentially, and for a capillary number greater than about 0.6 there is no bubble entrapment.

The measured critical crater cone angle for peak bubble entrapment weakly increases with the capillary number and the measured value is in agreement with Longuet-Higgins'

theory in the inviscid limit. The growth of the main body of the high-speed thin jet, formed immediately following bubble pinch-off, has been fitted into a power law model and the temporal exponent, α, has been found to be smaller than 1. This suggests that the radial focusing of the bulk flow during bubble entrapment leads to a free surface singularity, and the resulting thin jet is in the same genre of free surface hydraulic jets as in surface wave collapse.

Finally, the phenomenon of viscous drop impact onto miscible inviscid pool is briefly discussed. This serves as a transit to the current study of the reactive drop impact, as in encapsulation. In viscous drop impact, bubble entrapment appears to be solely caused by the bulk flow focusing effect when the drop viscosity increases to higher than 100 times of that of the pool. This might be the same type of bubble entrapment observed in encapsulation operations.

CHAPTER IV

REACTIVE DROP IMPACT IN ENCAPSULATION

Introduction

In cell encapsulation, capsules are made by dispensing liquid poly-anion drops into a pool of cation or gelling solution. Upon drop impact, the capsule formation /gelation proceeds immediately at the surface and eventually inwards. This process is complicated by the dramatic drop shape deformation and recovery associated with the impact energy, the crater rebound, and the surface-energy-induced drop rebound. In the context of encapsulation, it is desired to make smooth and perfect spherical capsules; however, some morphological defects are usually observed on the gelled capsule surface. One example of the defect, shown earlier in figure 1.4 and discussed in chapter III, is related to the bubble entrapment during drop impact, and will be the major focus of this chapter. A secondary defect is the well-organized wrinkles present on the equatorial region of the completely gelled capsule surface, as discussed in appendix B.

In the previous chapter, the bubble entrapment in non-reactive drop impact has been discussed. It has been established that the bubble entrapment is caused by bulk flow focusing at the capillary crest, located near the impact crater bottom; the phenomenon being referred to as capillary wave pinching. The experiments also suggest that for the asymmetric drop impact (viscous drop impacting onto inviscid pool), the capillary wave-dependent bubble pinching is suppressed when the drop viscosity is higher than 30 cp. However, when the drop viscosity is further increased to above 100 cp, a different type of bubble entrapment occurs. Here the bubble entrapment occurs without the capillary wave

involvement and is due to the bulk flow focusing occurring above the viscous impacting drop. These findings have direct relevance for understanding bubble entrapment in reactive drop impact, as in encapsulation, where the drop viscosity is normally much higher than that of the pool.

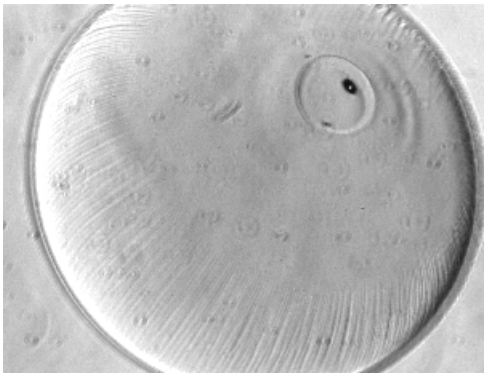

Figure 4.1. Microscopic picture showing surface wrinkles and defects due to bubble entrapment. The capsules are collected and stored in the same cation solution to ensure that the osmotic effect does not erase any surface defects once the capsule is formed. Additional observation is conducted within 30 minutes after the collection.

The primary objective of this chapter is to study bubble entrapment phenomenon in the context of capsule formation, and compare it with that observed in the classical simple liquid drop-pool impact studies. The impact crater shape during the bubble pinching is measured and analyzed, with the pinching process simplified as the one dimensional thinning process of the air void. The experimental data indicates two dynamic regimes for the pinching process, both in agreement with the theoretical predictions. Finally, the result of current study on bubble entrapment, together with the miscelleous discussions on capsule's morphological defects as presented in the appendix, provide simple guidelines for the optimization of the encapsulation process.

Bubble entrapment in capsule formation process

Experimental procedures

The reacting drop/pool pair chosen for the experiment is the MVG (FMC BioPolymer) and cellulose sulfate (Acros Organics) in phosphate buffered saline (PBS, contains 0.9 wt% NaCl, Baxter Labs) for the poly-anion drop, and the $CaCl_2$ (Fisher Chemicals) in PBS solution for the cation pool. This combination represents a typical chemical reacting system, and the chosen concentrations for these solutions are listed in Table 4.1 with the measured liquid properties shown.

The same frame-on-demand photographic technique, described earlier (chapter II), has been used to capture the free surface (crater shape and drop profile) evolvement during the poly-anion drop impact onto a reactive cation pool. Drop size used in this study ranges from 1.06 mm to 3.15 mm, and the impact velocity ranges from approximately 0.7 to 2.5 m/s.

Table 4.1. Material properties of chemical solutions used in the experiments.

	Density (10^3 kg/m^3)	Surface tension (dyne / cm)	Viscosity (cp)
Poly-anion I (0.8/0.8 wt % MVG/CS)	1.013	73.0	171.0
Poly-anion II (0.6/0.6 wt % MVG/CS)	1.010	72.5	59.1
Poly-anion III (0.4/0.4 wt % MVG/CS)	1.006	73.6	19.5
Cation solution (0.76/0.9 wt % $CaCl_2$/Nacl)	1.011	73.6	1.0

Results

The kinetic conditions for the drop impact experiments are plotted in the conventional non-dimensional *Fr*-*We* plane, as shown in figure 4.2. The solid symbols in figure 4.2 denote bubble entrapment observed during impact, while the open symbols correspond to no bubble entrapment being observed. Here, the drop liquid's (0.8/0.8 wt% MVG/CS) properties (surface tension and density) are used in calculating *We* and *Fr* number, which are close to that of pure water. However, the viscosity of the drop liquid is 171 cp, while the reactive pool liquid viscosity is around 1 cp. Figure 4.2 shows a much lower bubble entrapment limit than that determined from water system (dotted lines in figure 4.2), and the upper parametric limit for bubble entrapment as seen in the low viscosity system does not exist in current reactive drop impact system.

Three typical sets of picture sequence taken during reactive drop impact experiments are shown in figure 4.3, with the corresponding impact conditions denoted by data points a,b,c in figure 4.2. Figure 4.3.a shows the phenomenon of low energy impact. Throughout the observation, the boundary between the dyed drop liquid, which appears darker in the picture, and pool remains clear. This observation can be explained by the longer diffusive time scale of the poly-anion molecules compared with impact time scale. More importantly, the chemical reaction (gelation) at the interface bonds the poly-anion molecules almost immediately upon the drop-bulk contact, additionally preventing any diffusion. The picture sequence shows that as drop liquid expands quickly to its maximum width in the horizontal direction, a very shallow impact crater grows below the equilibrium surface. At t =10ms, the impact crater grows to its maximum shape,

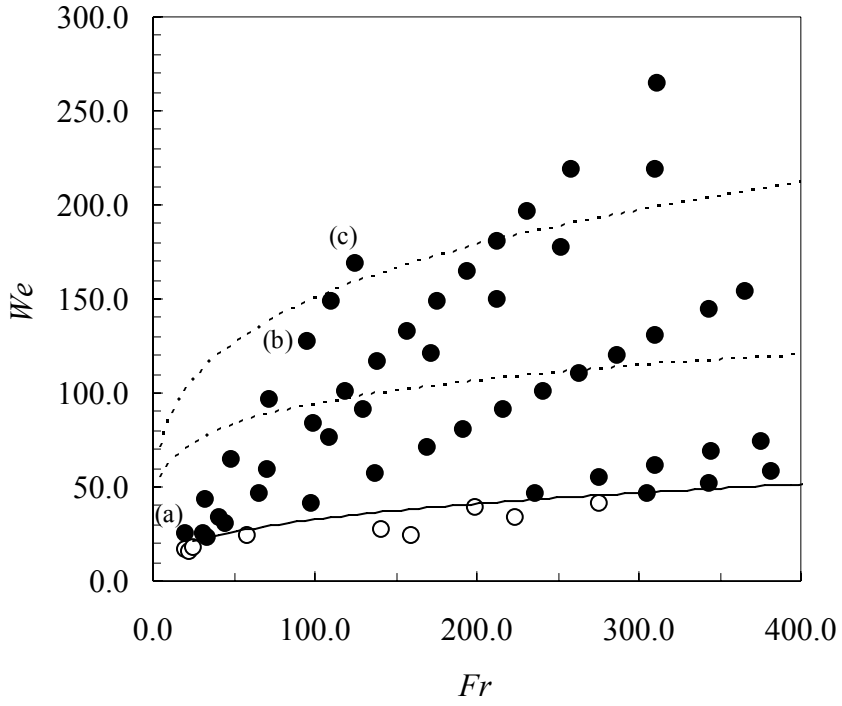

Figure 4.2. The bubble entrapment conditions plotted in *Fr*-*We* plane for the reactive drop impact system (drop: 0.8/0.8 wt% MVG/CS; pool: 0.76 wt% $CaCl_2$ in PBS). The filled circles denote bubble entrapment event, while open circles denote no obvious bubble entrapment. The dotted lines show the regular bubble entrapment limits for pure water drop impact system, determined by Pumphrey and Elmore [73]. The data points a,b,c correspond to figure 4.3.a,b,c respectively.

following which the crater starts to collapse inwards. The process of crater collapse is accomplished by the drop-pool interface continuously replacing the drop-air interface, in a smooth process, at the crater bottom. As a result, at t =19.4 ms, the drop liquid almost neatly separates from the bulk-air interface and fully immerses into the bulk. Here, only a very small air bubble is entrapped on the north pole of the top drop surface after the separation, and the bubble is not discernable in the picture resolution shown in figure 4.3.

Figure 4.3.b shows the crater evolution as the impact kinetic energy level increases so that the impact condition is located inside the classical inviscid bubble entrapment regime

(figure 4.2). During its growing phase, the impact crater appears to be a smooth elongating cylinder, with the drop liquid located mostly at the cylinder bottom in a nearly pancake shape. In this sense, the crater formation appears more like the case of solid disk impact on to a deep liquid pool [82]. In the current reactive drop impact system, the crater wall is free of the traveling capillary wave, originating at the equilibrium surface, which is an important requirement for bubble entrapment in inviscid drop impact system (figure 3.3 and 3.10.b). Owing to the high viscosity of the drop, the potentially inward traveling capillary ripple is damped out on the drop surface, or is non-existing at high viscosity. After t = 12 ms, the crater opening starts to widen while its lower half contracts radially, leading to a cone shaped impact crater, signaling the crater restoration process similar to the observations in the inviscid system. The sudden change in the curvature near the pinned bottom (t = 16 ms) represents a capillary resistance to the bulk focusing flow. The picture of t = 18.3 ms shows that the actual location of crater wall collapse is above the drop surface, and an air bubble is entrapped and attached to the drop. This entrapped bubble blocks local gelling reaction, and gives rise to the morphological defect shown in figure 4.1.

As the impact energy level increases to above the inviscid bubble entrapment limit, bubble entrapment in reactive drop impact system is still observed, as seen in figure 4.3.c. Here the impact crater grows deeper at the bottom and wider at the top before it starts to collapse, owing to the higher kinetic energy associated with the impacting drop. However, the local pattern of the bubble pinching event at the crater bottom appears similar to the one in figure 4.3.b, except that the profile is more cylindrical. Here, the entrapment can be described as radial pinching of the sub-cylindrical surface extended from the cone

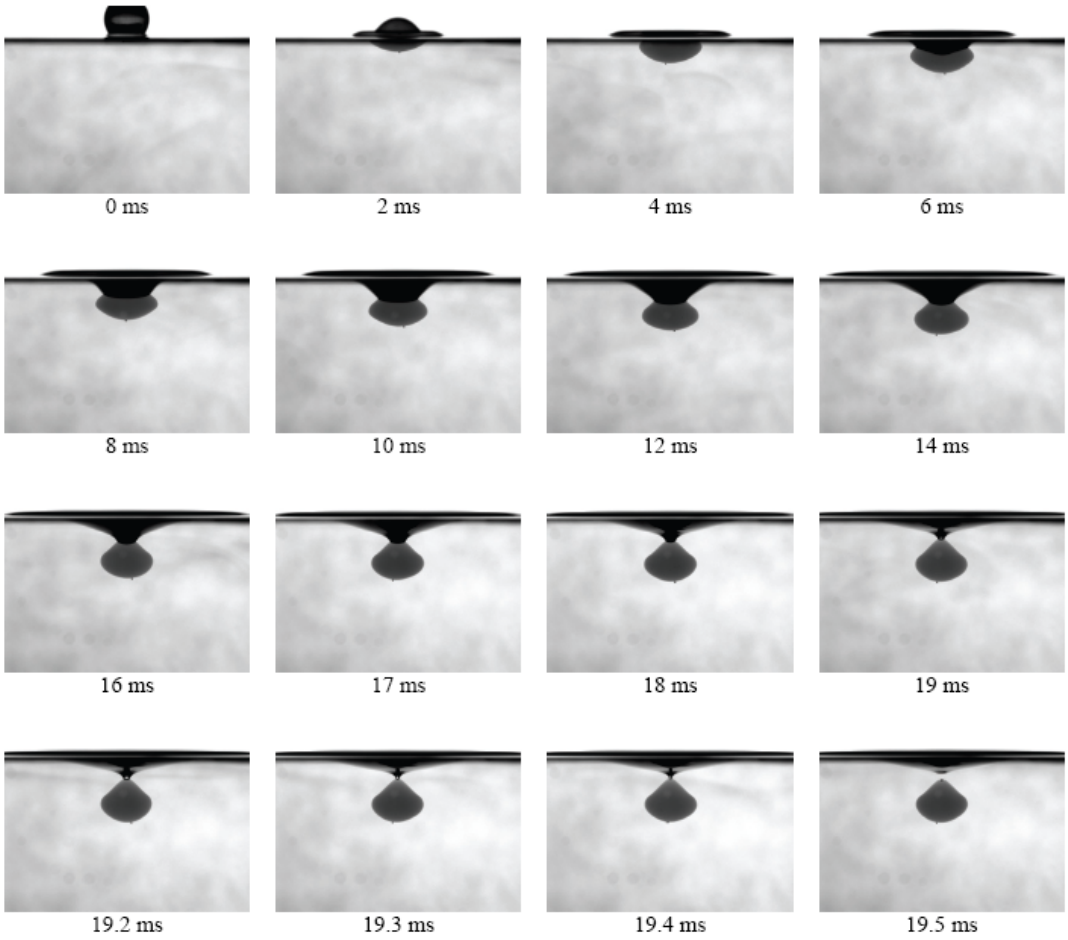
0 ms
2 ms
4 ms
6 ms
8 ms
10 ms
12 ms
14 ms
16 ms
17 ms
18 ms
19 ms
19.2 ms
19.3 ms
19.4 ms
19.5 ms

Figure 4.3 (a)

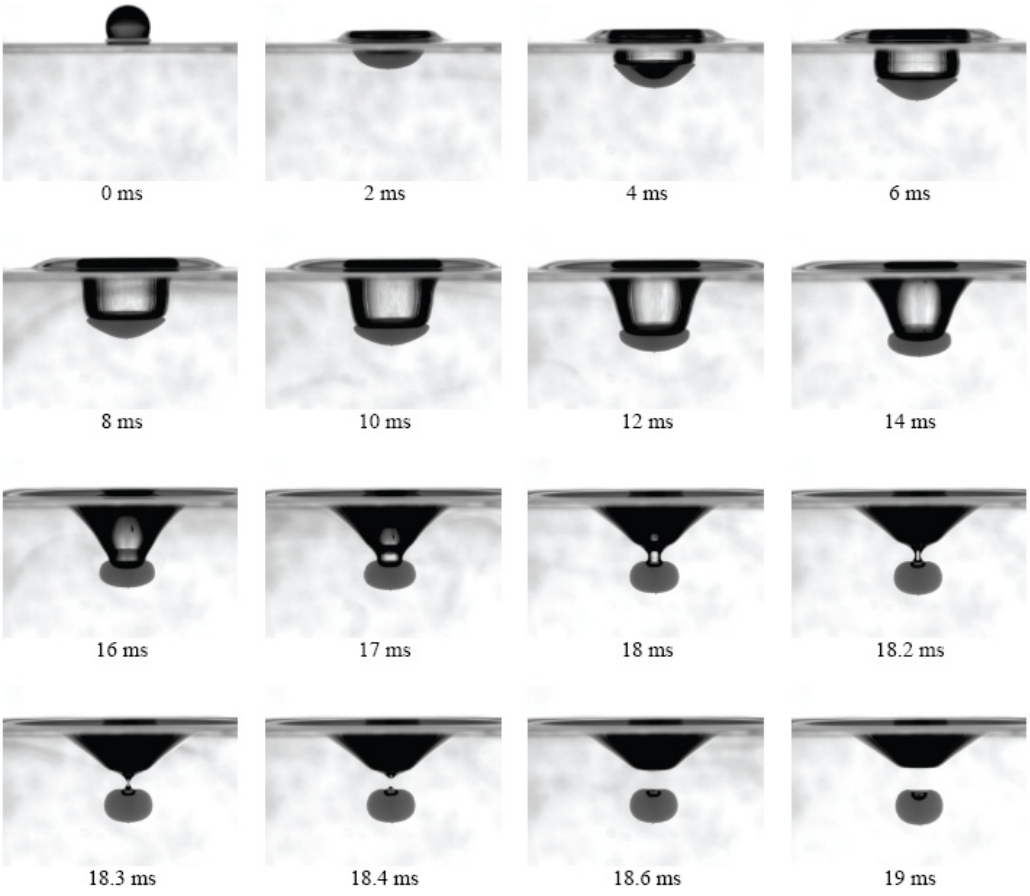
0 ms
2 ms
4 ms
6 ms
8 ms
10 ms
12 ms
14 ms
16 ms
17 ms
18 ms
18.2 ms
18.3 ms
18.4 ms
18.6 ms
19 ms

Figure 4.3 (b)

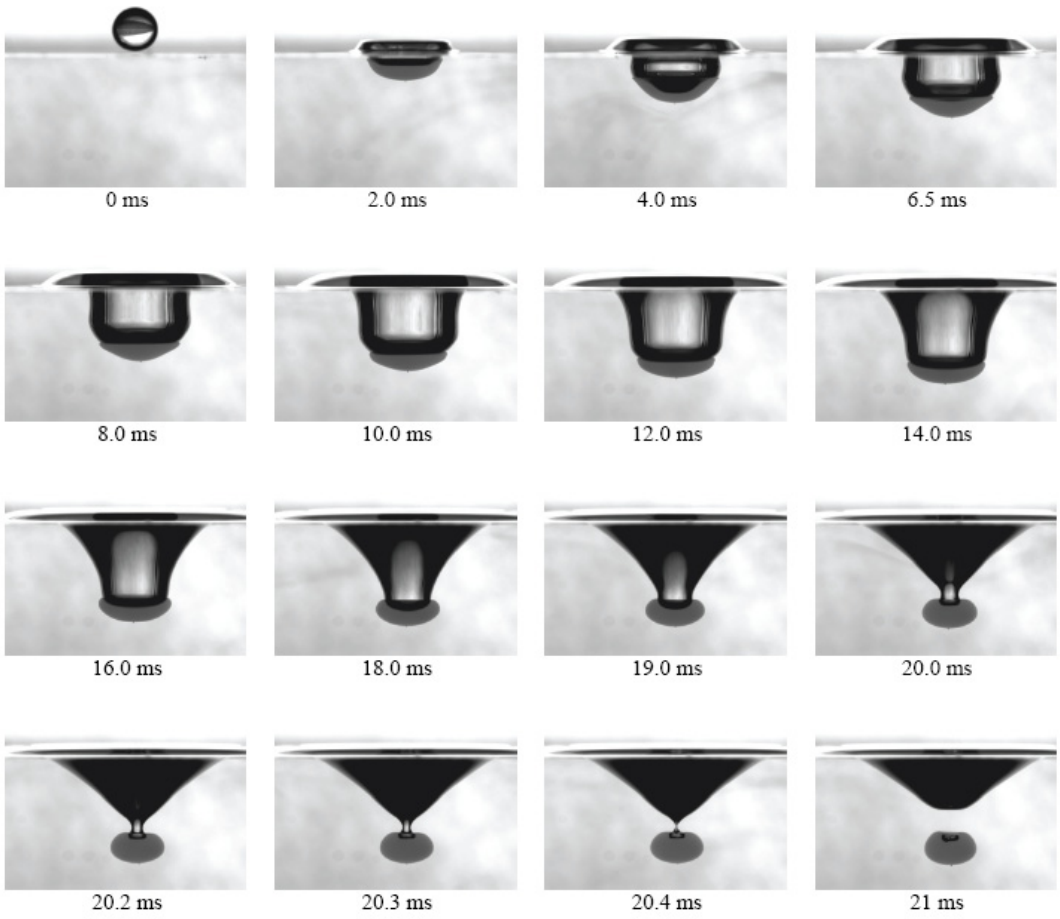

Figure 4.3 (c)

Figure 4.3. Picture sequence showing impacting crater and drop deformation following a 3.15 mm poly-anion drop (MVG/CS, 0.8/0.8 wt%) impacting onto gelling pool ($CaCl_2$ 0.76 wt% in PBS) at three different kinetic conditions: (a) *Fr* = 19.3 , *We* = 26.0; (b) *Fr* = 94.6 , *We* = 127.7; (c) *Fr* = 125.3 , *We* = 169.9. The corresponding impact *Fr, We* data points are shown in figure 4.2.

shaped crater tip. Again, the development of the impact crater shows no signs of the capillary wave traveling downward along the crater side wall, indicating that the bubble entrapment phenomenon is activated by a different mechanism from the inviscid system. The dynamics of this bubble entrapment will be investigated in this chapter by comparing the present experimental results in reactive viscous drop impact with those obtained from inviscid drop impact systems.

It is also noted that although the radius of curvature on the transverse section (neck radius) uniformly decreases to zero during bubble entrapment process, the curvature change on the longitudinal section (picturing plane) is different for the three cases as shown in figure 4.3. Near the moment of pinching, the longitudinal curvature is highest for the low *We* drop impact case (figure 4.3.a), and lowest for the high *We* case (figure 4.3.c). This observation suggests that the surface tension effect, represented by the capillary curvature, becomes weaker as the impact energy level, or *We*, increases and vice versa.

Figure 4.4 shows the measurement of entrapped bubble size as function of impact Weber number (*We*) for different drop sizes. The scaled entrapped bubble size (*d/D*) is independent of the original drop size, as all the data points collapse into one curve. The bubble is non-detectable as the impact energy is decreased to below a critical value. An empirical limit delineating the parametric regime of bubble entrapment and non bubble entrapment in *Fr*-*We* plane is plotted in figure 4.2 (solid line). The measured maximum entrapped bubble size is about 30% of the diameter of the impact drop size. At very high impact velocities (*We*>300), more than one bubble will be entrapped after the crater collapse, probably due to the strong capillary disturbance along the circumferential

direction. This unstable phenomenon limits the selection of parametric range. In general, the data spread in figure 4.4 shows two regimes of bubble entrapment: (I) low *We* regime (*We* < 100), the entrapped bubble size increases rapidly as *We* increases, and (II) high *We* regime (*We* > 100), the bubble size approaches a constant value. In other words, the measurement of entrapped bubble size implies that the bubble entrapment event in regime (I) shows effects of capillary curvature changes, whereas, regime (II) is independent of it. This result is in agreement with the observation from figure 4.3. The detailed quantitative analysis of this bubble entrapment process and the governing forces will be discussed in this chapter.

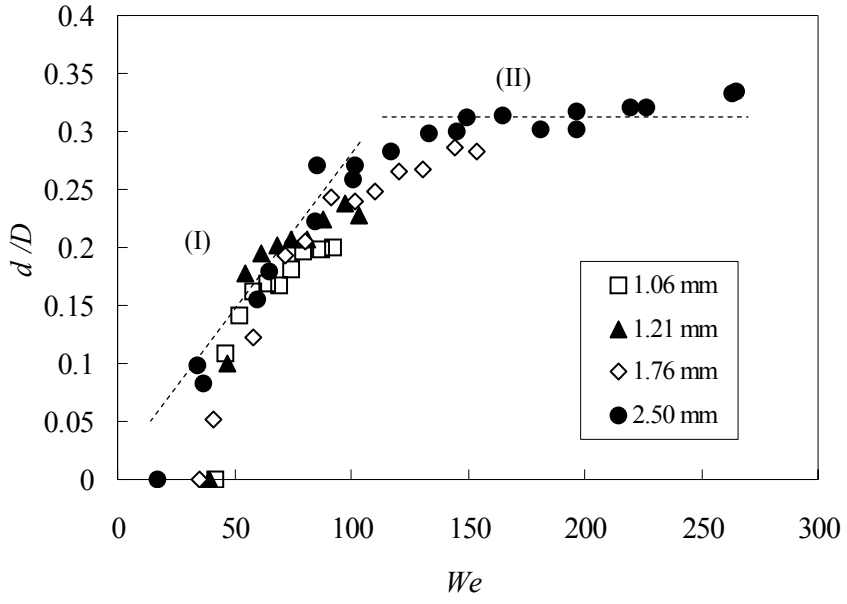

Figure 4.4. Measured entrapped bubble diameter, scaled as *d/D*, versus *We*; Poly-anion drop: MVG/CS 0.8/0.8 wt%, gelling solution: 0.76 wt% $CaCl_2$ in PBS.

Flow characteristic of the impact crater

Picture sequences in figure 4.3.b and c show that the bubble entrapment in reactive drop impact occurs at the moment of impact crater collapse, and the bubble pinch-off is driven by the bulk fluid flow around the crater. Therefore, in order to reveal the flow characteristics associated with bubble entrapment, it is helpful to first examine the dynamics of the impact crater formation and collapse.

The formation of impact crater is the result of the energy transformation from the kinetic energy of impacting drop to the potential energy (gravitational and surface energy) stored in the impact crater. The amount of the potential energy stored in the crater can be calculated using the crater profiles captured in each frame. Figure 4.5 shows the result of the crater potential energy analysis, in absolute units, for three different drop impact experiments: (1) low energy reactive impact, (2) high energy reactive impact and (3) high energy water impact, with the same impact drop size (D = 3.15 mm).

The peak in the potential energy profile shown in figure 4.5 corresponds to the time when the impact crater grows to its maximum shape and begins to rebound. Here the crater-pool system behaves like a mass-spring system, where the potential energy and kinetic energy exchange after the initial disturbance (i.e. drop impact). Upon initial contact, the impact crater first stores the potential energy, and after reaching its maximum shape, the crater releases this energy as kinetic energy of the bulk liquid flow, driving the restoration of the impact crater. Despite the bulk liquid being inviscid, the drop viscosity plays a role in dissipating some of the impact energy and thereby less energy is available to the crater for the case of viscous drop impact, under the same impact conditions (figure

4.5). For the case of low energy impact, less crater energy is available to begin with and it is less likely that there will be a dramatic crater rebound.

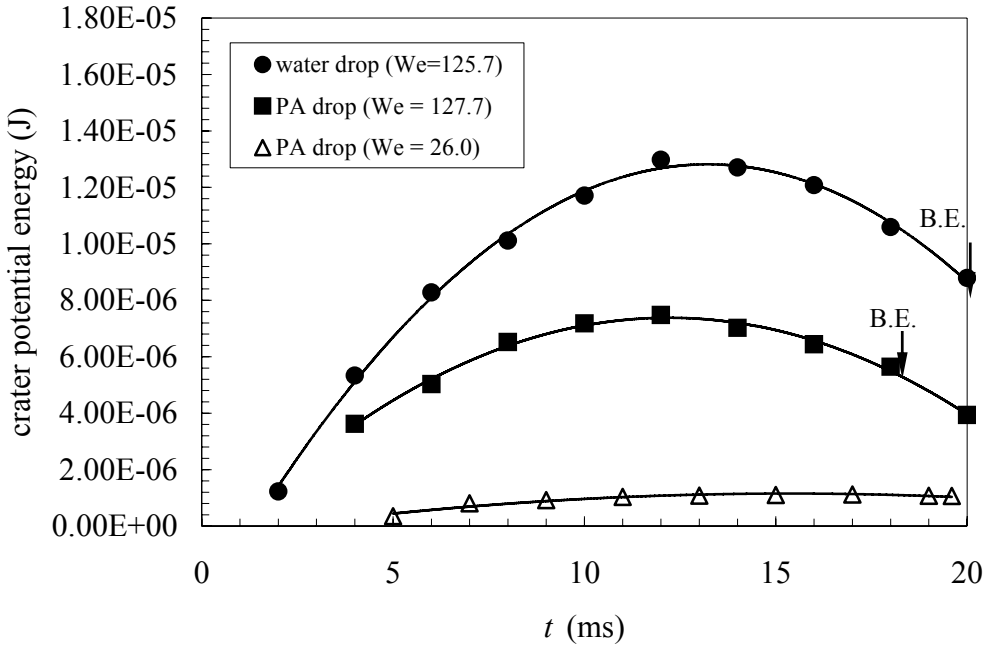

Figure 4.5 Comparison of crater potential energy evolution for three different impact conditions: (●) poly-anion drop (0.8/0.8 wt% MVG/CS) impact onto gelling pool at *Fr*=19.3, *We*=26, corresponding to figure 4.3.a; (■) poly-anion drop (0.8/0.8 wt% MVG/CS) impact onto gelling pool at *Fr*=94.6, *We*=127.7, corresponding to figure 4.3.b; (Δ) water drop impact onto water pool at *Fr*=94.2, *We*=125.7.

It has been established in the last chapter that the radial focusing of the bulk flow around the capillary crest drives the bubble pinching in the inviscid drop impact system. Here in reactive system, the pinching of the air bubble is also accomplished by the radial focusing of the inviscid pool liquid, as seen from pictures of figure 4.3. In drop impact

system, the kinetic energy source of the bulk flow is the potential (both gravitational and surface tension) stored in the impact crater. Accordingly, the intensity of the bulk flow depends on the maximum potential energy available from the crater, which further depends on the original drop kinetic energy. For the axially symmetric flow system as in drop impact, the bulk movement must be mostly in form of radial focusing in order to achieve the system's equilibrium state, and the focusing flow must be strongest at the crater bottom, where the hydrostatic potential is the highest. This explains the observation that the crater always evolves from a cylindrical shape to a conical one during the restoration. As will be shown later, the bulk focusing flow developed during the crater restoration provides the necessary flow condition for the bubble entrapment to occur in drop impact.

Another important characteristic of the impact crater is the critical crater cone angle: the cross angle of the impact crater side wall observed at the moment of crater collapse. It is known that the bubble entrapment in inviscid system always coincides with the critical cone angle of 109.5^{o}, the global singularity point predicted by L-H's theory. The singularity means the flow velocity diverges at this free surface flow configuration. Therefore the bubble entrapment, or collapse of bulk flow at the capillary crest, most probably occurs at this moment. Figure 4.6.a shows this relationship between bubble entrapment and the singular value of the critical cone angle, in the water impact system. For the reactive drop impact system, however, the bubble entrapment appears to not necessarily require the occurrence of the singular cone angle of 109.5^{o}, as seen in figure 4.6.b. The experiments show that at low impact energy level (We<100), the entrapped bubble size is smaller and the corresponding critical cone angle is higher than 109.5^{o}.

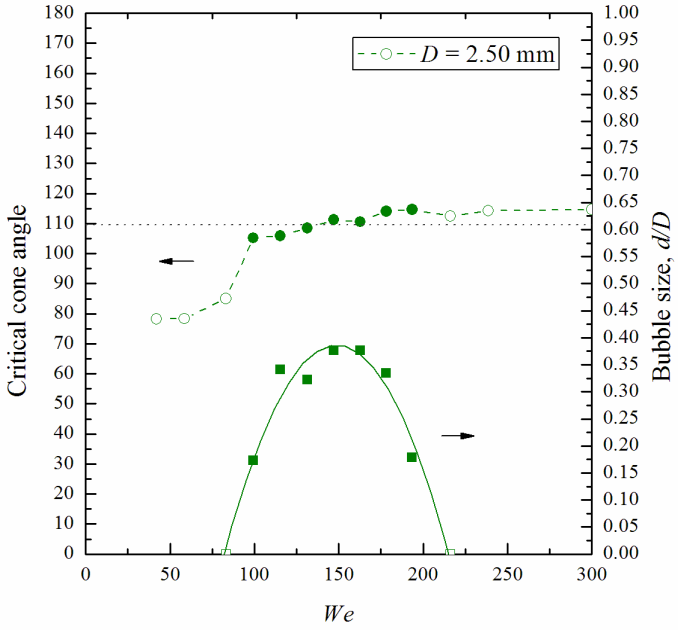

(a)

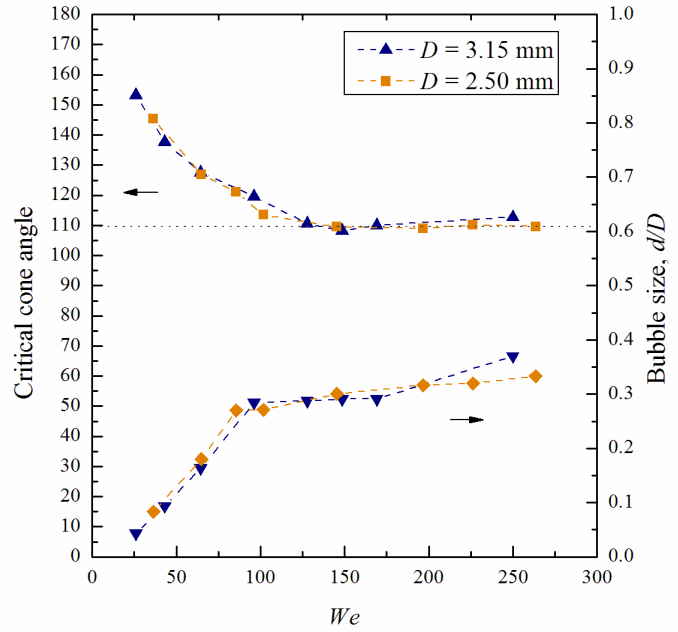

(b)

Figure 4.6. Plot showing the correlation between critical cone angle and bubble entrapment observation. The dotted line is the singularity cone angle of 109.5° as predicted by Longuet-Higgins[79]. (a) Water drop impact onto water pool; (b) Poly-anion drop (0.8/0.8 wt% MVG/CS) impact onto a cation pool.

However, as the *We* increases so that the condition is within and beyond the inviscid bubble entrapment regime, the singular 109.5 ^{o} cone angle is observed in a wide parametric regime, and the entrapped bubble size appears no longer dependent on the initial impact condition.

The upper parametric limit for bubble entrapment in inviscid drop impact system is caused by the crater bottom reversal occurring before the side wall collapse, as discussed in chapter III. Here in the reactive system, the crater bottom always attaches to the semi-gelled drop complex, which effectively blocks the reversal flow, and hence eliminates the upper bubble entrapment limit.

Local boundary conditions for bubble entrapment

Previous studies on drop impact with low viscosity liquids in chapter III found that the collapse of the impact crater does not necessarily lead to bubble entrapment. In order for the free surface flow to entrap air bubble, the bulk flow must be able to focus above the lowest point of the free surface, and therefore a certain form of surface disturbance is necessary at the crater bottom. This is true for the low viscosity drop/pool impact system, where the traveling capillary wave along the crater wall serves as this surface disturbance. It has been established that bubble entrapment in symmetric simple liquid impact system depends on the traveling capillary wave, and its timely arrival at the impacting crater bottom when the crater collapses [73-76,110]. The capillary wave crest facilitates inertial focusing flow at the position above crater bottom, resulting in the so called regular bubble entrapment. The experimental result discussed in chapter III further suggests as the viscosity of the liquid system is increased to about 15 cp for the symmetric system, or

30 cp for asymmetric system, the traveling capillary wave is damped out by viscous effect, and the regular bubble entrapment is not observed, no matter what the impacting condition is. Here in the reactive viscous drop impact system, as shown in figure 4.3, the impact crater wall throughout the crater growth phase is smooth and free of traveling capillary ripples. As indicated by figure 3.7, the inward traveling capillary ripple first appears at the drop surface during the initial contact between drop and pool surface, and eventually propagates inwards during the crater formation process. Here, since the drop liquid has high viscosity of 171 cp, this capillary disturbance is probably damped out before the crater formation. However, the bubble entrapment still occurs, thereby this event must be related to some other local free surface phenomenon.

Figure 4.7.a shows a detailed sequence of the local free surface profiles during bubble entrapment in a reactive drop impact experiment. At the time very close to collapse, the drop/pool/air three phase contact line located at the crater bottom is pinned, while the free surface above it is pushed inward by the bulk focusing flow. As a result, the region near the crater bottom represents an hourglass shape, with the neck continuously thinning till it breaks up and separates an air pocket. After the pinch-off, a downward liquid jet penetrates into the newly enclosed air pocket, indicating the vibrant dynamics in the local flow regime associated with the pinch-off. Generally, the whole bubble pinching process is similar to regular bubble entrapment in water drop impact onto a deep water pool, as seen in figure 4.7.b, except that the profile is more symmetric due to a well defined (stiff) crater bottom. In other words, the entrapment in encapsulation represents a more ideal bubble entrapment profile caused by the inviscid pool liquid.

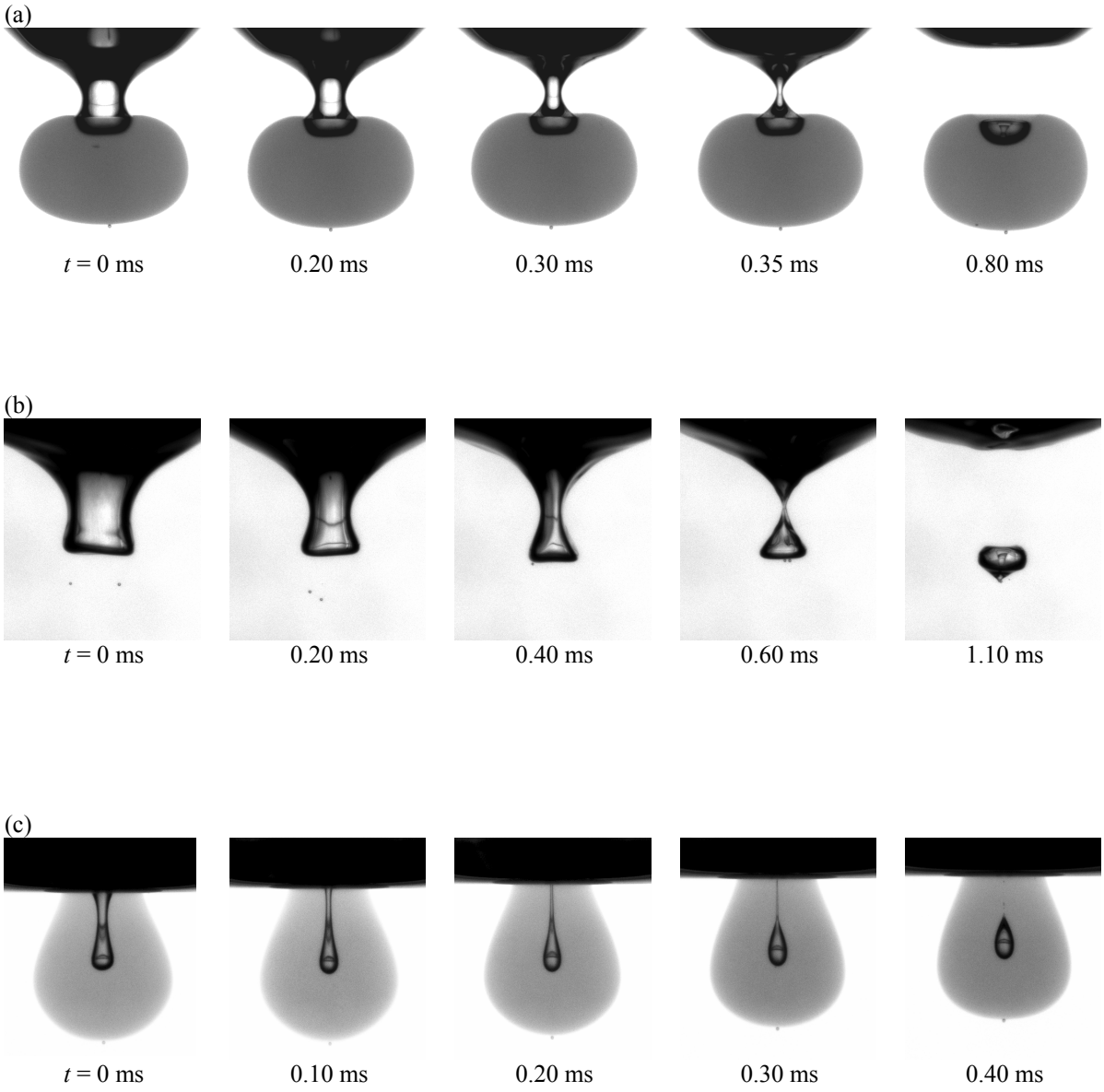

Figure 4.7. Picture array showing the free surface evolution immediately prior to bubble pinch-off for different liquid systems: (a) PA drop impact onto gelling pool, (b) water drop impact onto water pool, and (c) PA drop impact onto water pool. The kinetic impact conditions for all three cases are similar (*Fr*=95, *We*=127).

Figure 4.7.c shows the snapshots of a very different bubble pinching process, when the same poly-anion drop impacts onto a non-reacting water pool. Here the bubble pinch-off occurs as the viscous drop liquid encloses the impact crater bottom, unlike in the reactive system. The pinching process is slowed down compared to the other two cases, as the pinching is caused by the slow internal vortex flow in the viscous drop. The necking thread is much elongated, which later breaks into several micro-sized bubbles, as seen in the last panel of figure 4.7.c, and no downward jet is observed after the break of the thread, suggesting a less violent break-up. Through the comparison between figure 4.7.a and 4.7.c, it is clear that the gelling reaction has strong effect on bubble entrapment phenomenon. This reaction happens very fast so that it changes the drop/capsule surface property and the impact crater morphology, hence interfering with the bubble entrapment process.

The proposed mechanism of this particular bubble entrapment in encapsulation is shown in figure 4.8. As the poly-anion drop material contacts the cation pool, the surface gelling reaction proceeds immediately and imposes a membrane tension, $\sigma_{12,}$ along the drop surface. The value of σ_{12} should continuously increase with time as the reaction proceeds and the membrane thickens. At the air, bulk and drop three phase contact line, this gelling reaction-induced interface stress counteracts the bulk-air surface tension(σ_{23}) and drop-air surface tension(σ_{13}), preventing the full immersion of anion drop the and pinning the crater bottom. At time close to surface collapse, the multi-phase contact line is actually pinned (see figure 4.8.b) owing to the existence of the membrane, with a small portion of drop surface remaining un-wetted by the cation solution. At this stage, the bottom of the impact crater starts to contract inward rapidly, driven by the bulk focusing

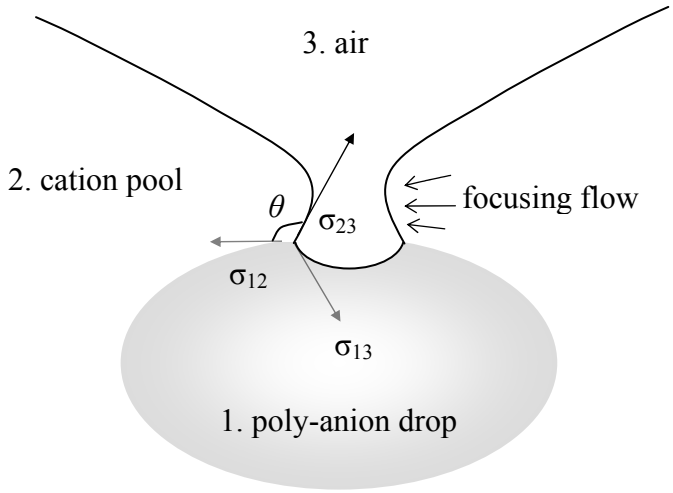

(a)

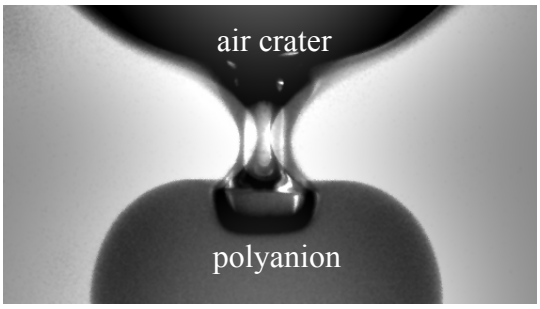

(b)

Figure 4.8. (a)Sketch showing the mechanism of bubble entrapment occurring at the north pole of the newly formed capsule. (b) Double exposure picture showing the pinned crater bottom and thinning of the air cylinder extruded from impact crater. The duration between the two flashes is 0.2 ms.

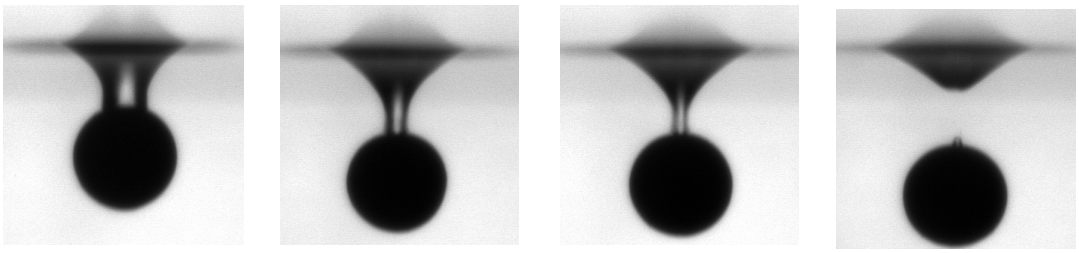

t = 0 ms 0.41 ms 0.82 ms 1.02 ms

Figure 4.9. Picture sequence showing bubble pinch-off during a solid bead (D=2.5mm) impact onto a water pool (V=1.70 m/s).

flow. The focusing flow initiates a typical dynamic wetting process along the newly gelled drop surface. Given the dynamic contact angle, θ, formed during the wetting process is greater than 90^o, the collapse of the bulk focusing flow must lead to an air pocket being enclosed and embedded on the capsule's north pole. In this sense, the non-wetting boundary condition of the capsule surface aids in the radial focusing of the free surface flow and sets up the condition for bubble entrapment. A very similar situation is observed in solid bead impact onto water pool, as shown in figure 4.9, where the impact solid bead traps an air bubble on its top surface after it penetrates through the pool surface. Here the impact crater is also smooth and free of capillary ripples.

From the above observation, the key criterion for bubble entrapment to occur in reactive drop impact system appears to be whether the dynamic contact angle, at the surface collapse moment, is greater than 90^o or not. The dynamic contact angle in a typical wetting problem is usually determined by the moving contact line velocity and the molecular interactions at the solid/liquid interface. For an advancing contact angle, the

higher contact line velocity is associated with greater contact angle, with an upper saturation limit as flow rate continuously increases [116]. More recently, the observed actual dynamic contact angle has further been found to be complicated by the flow characteristics in the vicinity of the wetting boundary [117]. In the context of capsule formation drop impact, the wetting is solely driven by the bulk focusing flow with a quasi-steady solid substrate (capsule), so that the contact line velocity will not vary much from flow velocity. The latter is related to the amount of potential energy associated with the impact crater, which is transformed from the initial kinetic energy of the impacting drop. Hence the higher impact energy causes stronger focusing flow, and accordingly greater contact angle. Figure 4.10 plots the measured contact angle development from two typical drop impact experiments with low and medium impact energy. The result shows that the contact angle at the pinching moment reaches 149^{o} for the high energy impact where bubble entrapment is observed (insert 1 of figure 4.10). For the low energy impact, the advancing contact angle reaches to only around 90^{o}, and the collapse of contracting free surface is relatively smooth, occurring at drop surface with almost no air bubble entrapment afterwards (insert 2). This suggests that in order for the bubble entrapment to occur, the focusing flow must be strong enough to generate a contact angle greater than 90^{o}. It further explains the observation that the bubble entrapment in reactive system requires a minimum impact energy level, as plotted as a solid line in figure 4.2. Figure 4.11 shows the measured contact angle on the drop complex surface as a function of focusing flow velocity, the latter determined as the contracting velocity of the neck surface. The observed contact angle profile is in agreement with general contact angle dynamics as described above.

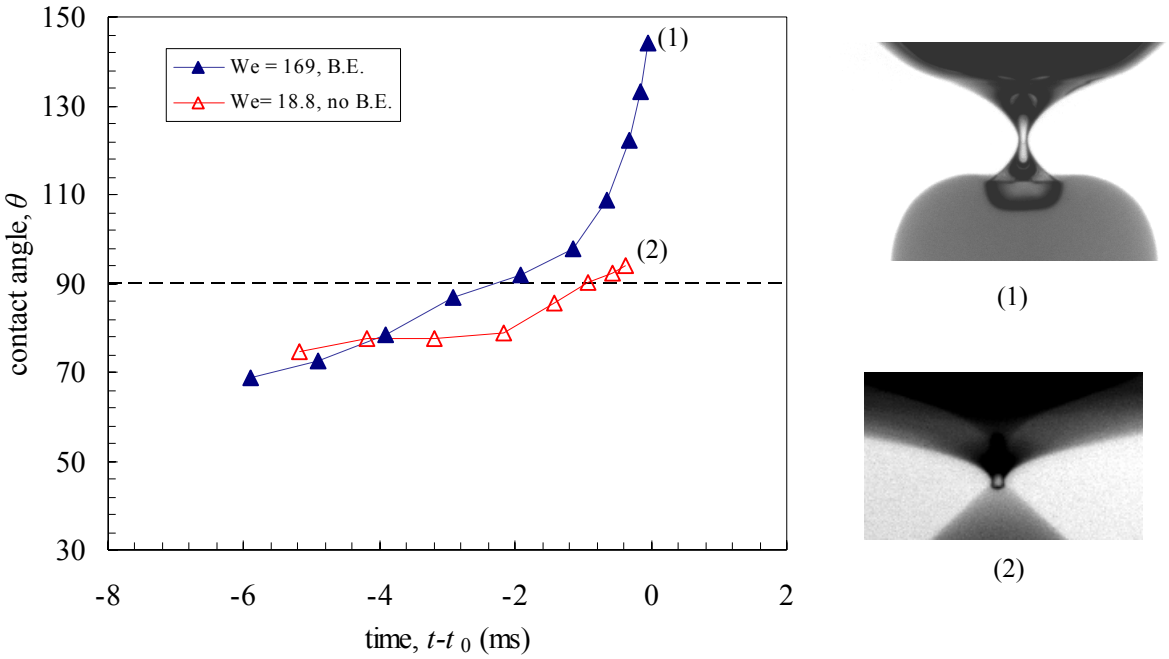

Figure 4.10 Comparison of contact angle evolvement for two impact experiments with and without bubble entrapment. (t_o is the bubble pinching moment).

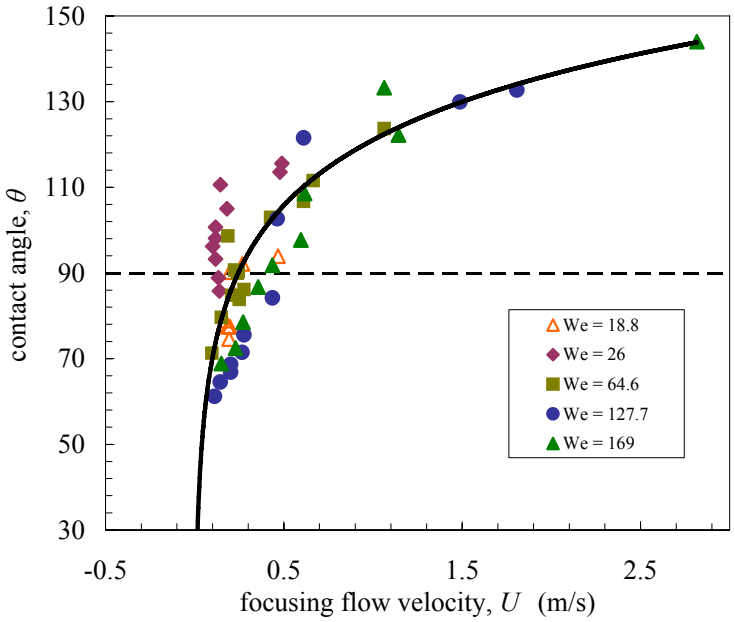

Figure 4.11.Dynamic contact angle (θ) on the capsule surface as a function of the bulk focusing flow velocity (U).

Discussions

It is shown through the experimental study that the bubble entrapment in reactive system is related to the dynamic process of the cation solution wetting the poly-anion drop/capsule complex surface. The wetting characteristic, contact angle, on one side is determined by the focusing flow velocity. This may explain the observation that when the singularity cone angle (109.5^{o}) of the impact crater is reached, the bubble entrapment will inevitably occur, as indicated by figure 4.6.b. On the other hand, the wetting process is determined by the material properties of the interface, which is further related to the chemical component of the gelling system. The experiments with lower concentration poly-anion drop impact shows smaller entrapped bubble size under the same impact condition, as seen in figure 4.12.a. This is probably because the intermediate membrane tension σ_{12} is lower for lower concentration gelling system, thereby the pinning effect of the contact line is weaker, and the contact angle is smaller. Figure 4.12.b shows the effect of surfactant on the bubble entrapment. Similarity, the surfactant molecules affect the molecular interactions on the solid/liquid interface, probably in the way favoring the wetting process, resulting in a weaker bubble entrapment phenomenon. The experiments with 0.4/0.4 w% MVG/CS poly-anion (μ = 19.5 cp) show no bubble entrapment under the same impact condition. This is because the membrane complex is weak and thereby unstable to fluid dynamic forces. The capsule membrane is unable to provide the stiffness necessary for the bulk flow to radially focus above the drop. With no pinned contact line between drop and bulk liquid, the drop complex follows the convective flow, viz. bulk focusing and later, reversal flow during the crater restoration (an example can be seen in figure 4.13).

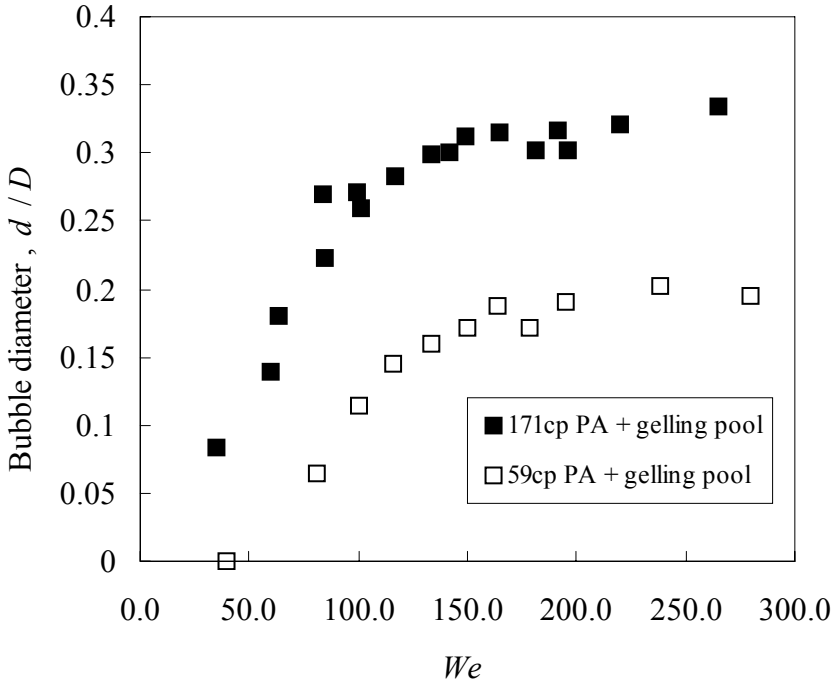

(a)

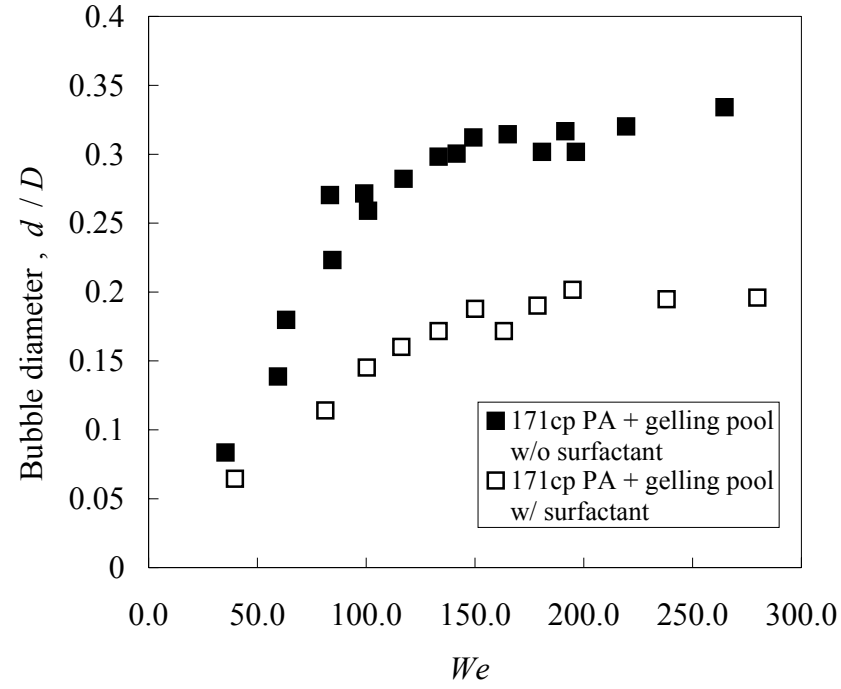

(b)

Figure 4.12. Bubble size measurement showing the effect of (a) poly-anion concentration, and (b) surfactant addition on bubble entrapment in reactive drop impact.

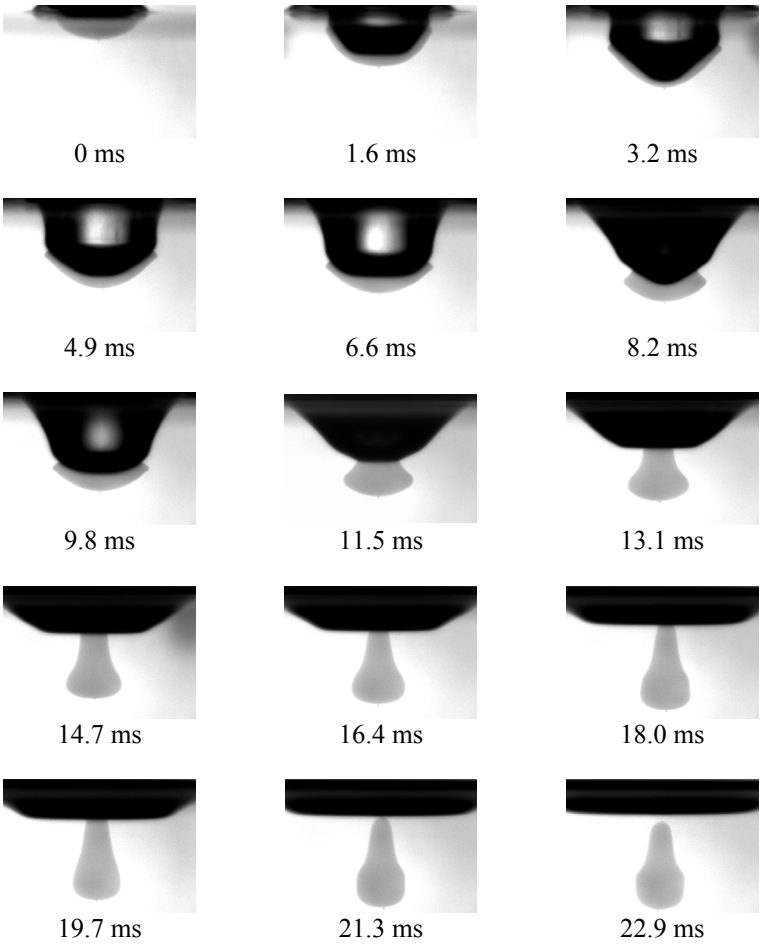

Figure 4.13.Picture sequence showing impact crater and drop deformation following the impact of a 2.50 mm poly-anion drop (MVG/CS, 0.4/0.4 wt%, μ=19.5 cp) onto the gelling pool ($CaCl_2$/NaCl, 0.76/0.9 wt%) at V=1.71 m/s. (Fr = 119.4 , We = 99.9)

Dynamic model for bubble pinching

It is concluded from above study that the pinned crater bottom and vibrant radial focusing flow initiate the bubble entrapment in capsule formation drop impact. In this session, the discussion will focus on the local free surface dynamics involved in the bubble pinching process. The bubble pinch-off observed in present drop impact study is physically quite similar to the surface collapse phenomenon as in solid disk impact [82] and air bubble breakup inside a liquid body [84,85,118]; however, owing to the small scale of the problem, capillary effects cannot be ignored in the current system.

All of these surface pinching processes can be simplified as a radial thinning process of a gas filament between two gas pockets. Recently, power law scale method has been found to be very useful in characterizing free surface collapse problem and revealing the physics involved in this problem. For the inertia dominated pinching process, the neck radius, h, can be scaled to time, t, as $h \sim t^{1/2}$ [5-8], or with a logarithmic correction, $h(-\log h)^{1/4} \sim t^{1/2}$ [82,85]. Numerical simulations from Leppinen & Lister [9] suggest $h \sim t^{2/3}$ if the surface tension slows down the process, and this result is sensitive to the density ratio of inner and outer fluid. Similar 2/3 power law is obtained from analytical modeling of [80] where the surface tension is also included. If the external liquid viscosity is high, the pinching process will be slowed down and the neck radius is shown to decrease linearly with time [84,119].

The collapse of a one dimensional slim air cylinder is governed by a modified Rayleigh-Plesset equation [77,82,84]:

$$(\ddot{h}h + \dot{h}^2)\log(\frac{h}{h_\infty}) + \frac{1}{2}\dot{h}^2 - \frac{\sigma}{\rho h} = gz \tag{4.1}$$

where h_∞ is the radius where the flow is quiescent, which would be the radius of crater opening on the equilibrium pool surface. Z is the depth of the neck below the equilibrium surface. Since the bubble entrapment occurs very fast, both h_∞ and Z remain approximately constant throughout the bubble pinching process in the experiments. The first two terms on the left side of equation 4.1 denote the inertia force, and the third term represents the surface tension force. The right side of the equation represents the constant hydrostatic force, which does not affect the exponent value of the power-law scale. Equation 4.1 indicates that the phenomenon of bubble pinching is driven by the inertial force and restrained by surface tension, thereby, the event can be captured by the Weber number $We_h = \rho U^2 h / \sigma$, where $U = dh/dt$ is the focusing flow velocity. However, since the consistent measurement of U and h is not possible as they are both time dependent variables, the phenomenon here is scaled by the impact Weber number, $We = \rho V^2 D / \sigma$, as in figure 4.4, where the actual local Weber number will be two orders lower owing to the length scale of the problem (h). Equation 4.1 also assumes the flow to be inviscid potential flow, which requires the local Reynolds number, $Re_h = \rho U h / \mu >> 1$. For the bubble entrapment observed in reactive system, the Re is estimated to be greater than 100 based on the experimental measurement of h. Thus the viscous effects can be neglected.

If the bubble pinching process is purely driven by inertia ($We >> 1$), then as $h \to 0$ the most singular term of equation 4.1 is the one containing logarithmic term. One can find the asymptotic solution of $h \sim \tau^{1/2}$, which sets the term containing logarithmic expression identically to zero, considering $\ddot{h}h + \dot{h}^2 = 0$. The same 1/2 power law scale can be derived from incompressibility ($\nabla \cdot \tilde{u} = 0$) of the fluid. To satisfy $\nabla \cdot \tilde{u} = 0$, $\dot{h}h$ must be

a constant in the case of one dimensional focusing flow [81]. More recently, an asymptotic solution to equation 4.1 has been derived in the limit of h / h_∞<<1, with a logarithmic correction to the neck radius h, expressed as[82]:

$$h^*[-\log(h^*)]^{1/4} = \sqrt{2}\tau^{*1/2} \tag{4.2}$$

where the radius and time have been non-dimensionalized as $h^* = h / h_\infty$ and $\tau^* = \tau / \sqrt{gZ / h_\infty^{\,2}}$.

Another scenario is that during the pinching process, the local inertia force ($\rho \dot{h}^2$) due to focusing flow is balanced by the surface tension force (σ / h), in which case the characteristic *We* should be smaller than inertia dominated situation. Then $\dot{h}^2 h \sim \sigma / \rho$ approaches constant, which gives $h \sim \tau^{2/3}$. This two third law has also been obtained from numerical simulation [86] and analytical modeling of [80], where the surface tension force is included in the model.

For each reactive drop impact experiment of current study, the neck radius h from the picture has been measured, and labeled with time $\tau = t - t_0$ (t_0 being the moment of pinching determined from experiment). The best temporal resolution of the measurement is 0.1 ms with ± 0.04ms error. Figure 4.14.a shows three typical sets of h-τ data from drop impact experiments with different impact energy, where the neck radius data within 8 ms before the pinch-off is chosen for analysis. The focusing velocity, represented by the sectional slope of h-τ curve, increases as time approaches the pinching moment. After pinch-off, the high radial inertia is transferred into the vertical counterpart, so that the inertial jetting is observed along the symmetric axis, as seen in the last panel of figure 4.7.a. Additionally, the open symbols in figure 4.14 show the h-τ measurement for the non-

reactive poly-anion drop impact case, corresponding to figure 4.7.c. Here, the pinching process is slowed down and the necking speed decreases as τ approaches to 0, indicating a much different pinching dynamics associated with viscous effect, as expected.

The solid lines in figure 4.14.a shows the power-law fitting results, $h \sim t^{\alpha}$, for the data sets from reactive drop impact experiments with different impact conditions. Each set of data can be fitted well into a power-law curve, as evidenced by the fact that in all cases the R-squared value is greater than 0.995. The best fitting exponent α is plotted in figure 4.14.c against the impact *We* number. Figure 4.14.b shows the power-law fitting of the nondimensional parameters according to $h^*[-\log(h^*)]^{1/4} \sim \tau^{*\alpha_c}$. The corrected exponent α_c is also plotted in figure 4.14.c. The dashed line in figure 4.14.b shows the exact prediction of equation 4.2. It appears that equation 4.2 over predicts the neck radius, and the slopes of experimental fitting, represented by α_c, are close to the predicted value, 1/2. In addition, as *We* increases, the experimental result moves closer to the theoretical prediction for the inertia dominated regime, as seen in figure 4.14.b.

From figure 4.14.c it is seen that at low *We* (<100) the power-law fitting exponent α agrees well with 2/3, indicating the bubble pinching under the influence of both inertia and surface tension. As *We* increases to above 100, α decreases to reach a lower level. The logarithmic correction can only decrease the fitting exponent by a certain amount, and the universal exponent for α_c is still not observed. However, to the right side of figure 4.14.c (*We*>100), the fitting exponents α_c are very close to 1/2, suggesting the pinching occurs in the purely inertia dominated regime as discussed above. This result appears in agreement with the experimental data of entrapped bubble size, as shown in figure 4.4. Here the two dynamic regimes of bubble pinching agree well with the regimes I and II of

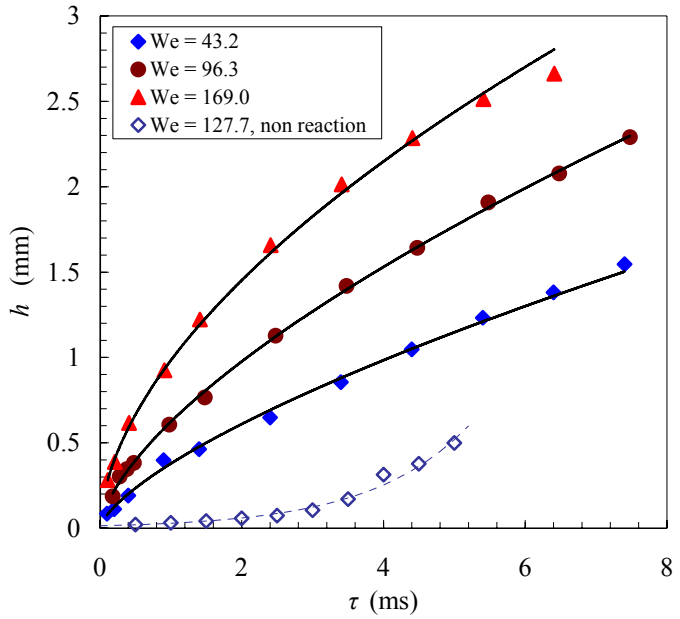

Figure 4.14 (a)

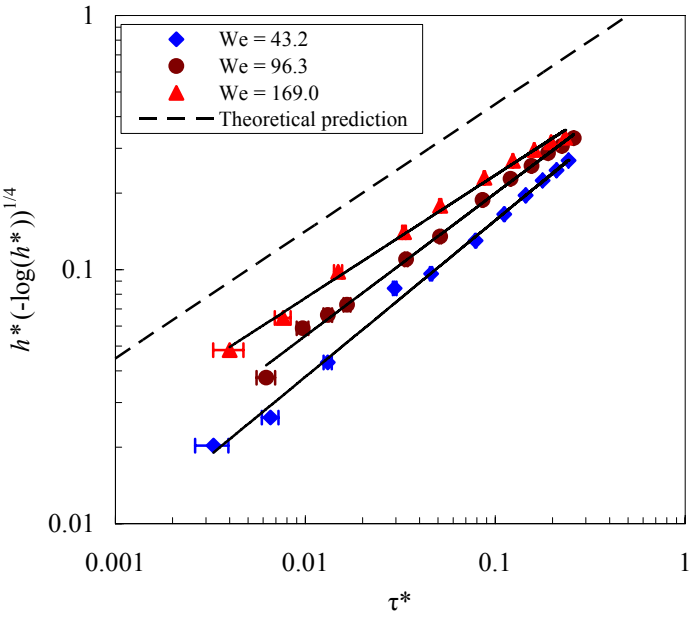

Figure 4.14 (b)

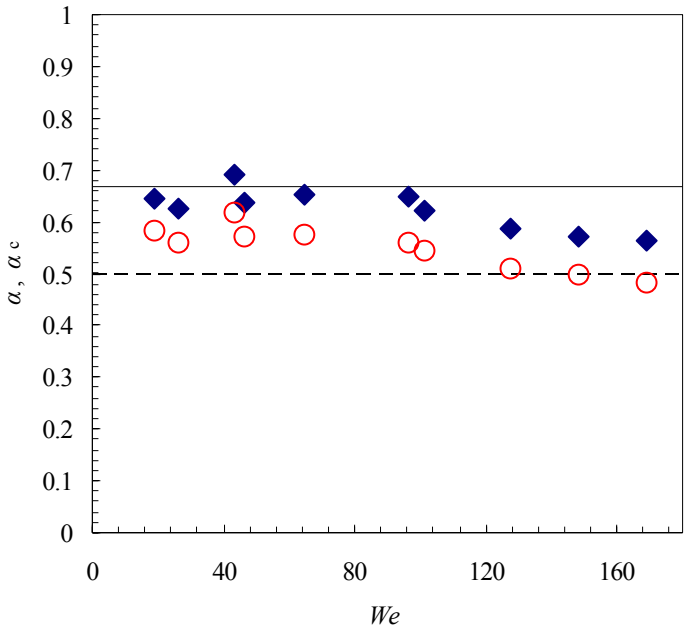

(c)

Figure 4.14.(a) Plot of measured minimal neck radius, h, versus time, τ, during the bubble pinching process. Solid symbols show the measurements for the 171 cp PA drop (D=3.15mm) impact onto the gelling pool at three typical impacting velocities, scaled as We. The open circles show the measurements from a PA drop impact onto a non-reactive water pool. (b) Data of (a) plotted in logarithmic nondimentional plane: $h^*\log(-h^*)^{1/4}$ versus time τ^*. The dashed line is the theoretical prediction in the inertia dominated regime (equation 4.2). (c) Experimental fitting exponent α (◆) and α_c (○) plotted versus impact Weber number, showing two regimes of 2/3 power law and 1/2 power law for the bubble pinching process.

figure 4.4, which are revealed by the entrapped bubble size measurement. As seen from the regime I of figure 4.4, since the phenomenon is surface tension dependent, the bubble size is sensitive to *We*; while in the regime II, the bubble size approaches a constant value due to the purely inertial effect.

More interestingly, the data of figure 4.14.c shows the transitional point from inertia-surface tension regime to pure inertia regime is very close to *We* = 100, which is the condition that the crater cone angle starts to approach the singularity point, 109.5^{o}, as seen in figure 4.6. This observation connects present surface pinching analysis to the earlier study of singularity conical flow. When the crater cone angle reaches 109.5^{o}, the entire flow field tends to experience a shock (velocity jump) at $\tau = 0$, predicting that the surface collapse becomes totally inertia driven at this condition.

The relative importance of the inertia force versus surface tension can be more adequately evaluated by the local Weber number, $We_h = \rho U^2 h / \sigma$. Here, We_h is a time dependent value, and the average value over the time span of our data analysis is estimated to be in the range of 0.5 to 5. Thus in our reactive drop impact system, the surface tension force shall not be neglected, especially when the impact kinetic energy is low. This is different from the case where the bubble pinching is caused by solid disk impact, as discussed in [82]. In their paper, Bergmann *et al.* reported the local Weber number to be greater than 100, and only the 1/2 scaling law was recovered from their experiments

Above model neglects the internal air flow inside the crater, which might slightly affect the exponent of the power-law scale. During the pinching, the air inside the neck must be squeezed out from the neck, leading to a pressure drop in the axis. This Bernoulli

effect may accelerate the collapse of the interface and hence decrease the power-law exponent, as discussed by Gordillo *et al.*[85]. For the bubble entrapment in the non-reactive case (figure 4.7.c), equation 4.1 is no longer applicable since the necking area is enclosed by the high viscous drop liquid (μ=171 cp). Here, the viscous force starts to play a role in the free surface pinching, and no simple power law fitting is found to such pinching process. The dotted line in figure 4.14.a is an exponential fitting to that set of data.

Conclusions and remarks

Bubble entrapment in reactive drop impact has been re-examined in this chapter under a wide range of impact kinetic and chemical conditions. Unlike the simple inviscid drop impact system, the bubble entrapment in reactive system does not depend on the traveling capillary wave, and the event occurs in a wider parametric regime with no apparent upper *Fr-We* limit. The experimental observation suggests the gelling reaction *freezes* drop surface rapidly before the crater collapse, so that the bubble entrapment occurs in a way more like a solid object impact onto water pool, where a dynamic wetting process occurs on the solid surface. Bubble entrapment in this context is caused by the dual effect of pinned impact crater bottom, due to the limited wetting speed, and the fast surface collapse driven by the bulk focusing flow near the crater bottom. Following this mechanism, the phenomenon is affected by the impact kinetic condition and the chemical component of the system as well, in agreement with the experimental observations. However, interestingly, the phenomenon can be examined through a global fluid dynamic perspective.

A simple one dimensional dynamic model is used to capture the free surface dynamics of the bubble pinching process in present reactive drop impact system. The experimental data indicates two dynamic regimes: inertia dominated (1/2 power law) regime and surface tension-inertia dominated (2/3 power law) regime, both in agreement with the theoretical predictions. The transitional point of these two regimes is found to coincide with the impact condition that singularity conical flow (critical cone angle of 109.5^{o}) starts to develop around the impact crater.

The current study suggests that the bubble entrapment in encapsulation can be avoided if the impact energy, determined by the drop size and impact velocity, is kept low. In the appendix it is shown that other morphological defects, like surface wrinkles and micro bubble entrapment due to initial drop-bulk contact, are also related to the impact kinetic condition. As impact *We* number increases, the intensity of inertial focusing flow and the degree of drop deformation upon impact increases, thus it is more likely that bubble entrapment and surface wrinkles will be present on the capsule surface. In general, the results of this study provide an upper limit for selecting the optimal drop impact speed and drop size in drop dispenser based encapsulation system, as illustrated in figure 4.15.

It appears that lower impact kinetic energy is always desirable in terms of capsule morphology. However, certain minimum amount of kinetic energy is required in order to help the falling poly-anion drop to penetrate through bulk-air interface. If the impacting kinetic energy is kept close to zero, then the only force that drags the anion drop through the interface is gravity. The time scale of the penetration dominated by gravity is usually several hundreds of milliseconds, ($t_s = \sqrt{2D/(\Delta\rho \cdot g/\rho)}$, $\Delta\rho/\rho$ being the density

difference between the anion drop and cation bulk divided by the anion density). In this scenario, the σ_{12} may grow large enough so that it prevents the full immersion of the anion drop. Thus, in a continuously running encapsulation system, the insufficient impacting kinetic energy (too low dispensing height, or too small drop sizes) may result in the poly-anion complex accumulation on the surface of receiving cation bulk, which ultimately fails the encapsulation operation. The micro bubble entrapment due to initial contact becomes more serious in the low velocity drop impact, as discussed in appendix C, which may pose additional lower parametric limit for encapsulation operation (dashed line in figure 4.15). Another consideration about selecting drop size comes from De Vos *et al.* [32,33], who suggest the poly-anion drop size (D) should not be smaller than 0.6 mm. This is because the percentage of incomplete encapsulation, caused by islets protrusion from the membrane, increases greatly when much smaller drop size is used. All these concerns justify the need for future study on the defining the lower parametric limit for optimal encapsulation process.

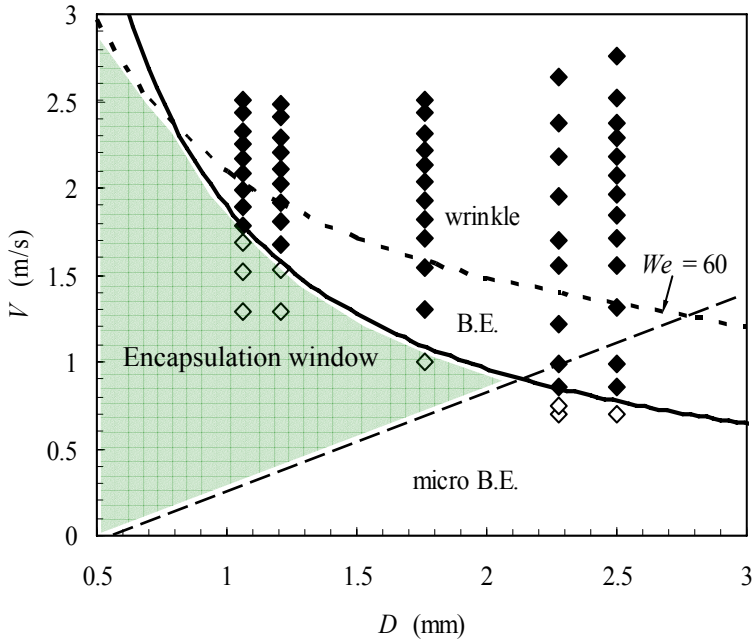

Figure 4.15. Operational map showing considerations for producing defect free microcapsules.

APPENDIX A

LONG TIME DROP (CAPSULE) SHAPE EVOLUTION FOLLOWING IMPACT

Studies of chapter IV (figure 4.3) have shown that the drop liquid experiences strong deformation during impact. However, the completely gelled capsule should have a perfect spherical shape in order to achieve maximum mechanical strength and optimal bio-performance. In fact, despite the strong impact deformation, the drop complex is able to recover into a spherical shape, primarily due to the competing chemical and fluid forces acting over the long time scale. In this appendix, the dynamics involved in the capsule shape deformation/recovery process following impact will be discussed, with the emphasis on the role of long-time gelling reaction and shape recovery.

Figure A.1 shows the measurement of the capsule shape evolution following the impact of a 2.5 mm poly-anion drop onto a cation pool. The capsule shape deformation during impact is evaluated by the aspect ratio e, defined as drop thickness divided by the width, $e = h_D/w$, and dimensionless drop width (or expansion ratio), $\beta = w/D$, where h_D is the drop thickness along the symmetric axis, and w is the longer axis length of the deformed drop, as shown in inset of figure A.1. The maximum deformation ($\beta_{max} = 1.77$, $e_{min} = 0.11$) of the drop is observed within five milliseconds after the initial contact of the drop with the bulk surface. After the maximum expansion, the drop shape has an intermediate temporal improvement, as seen from local peak values in both curves at $t = t_s = 12$ms. This is caused by the rebound of both the drop and the crater. Time t_s roughly corresponds to the separation of the anion drop from the air-liquid interface,

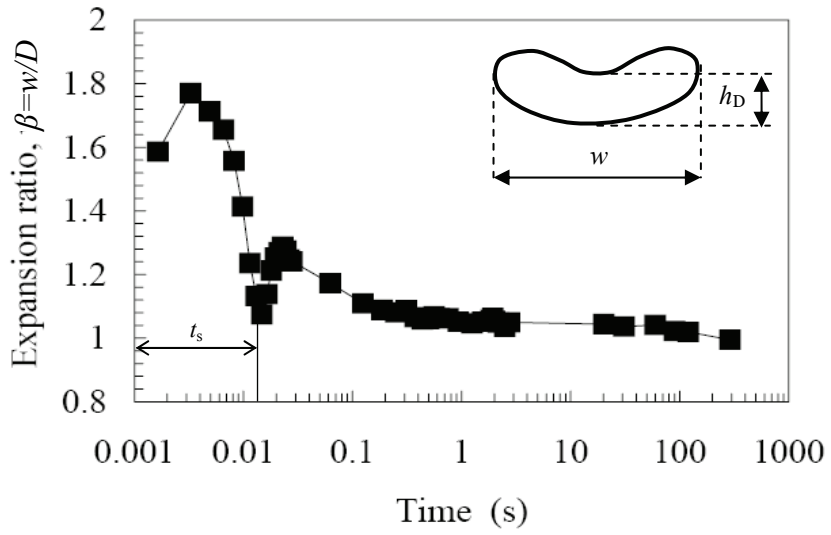

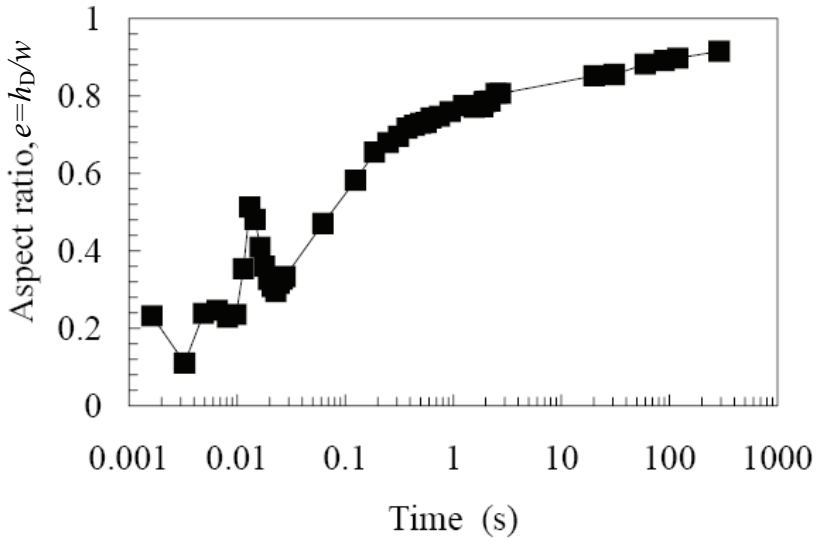

(b)

Figure A.1. Measured drop/capsule shape evolvement: (a) expansion ratio β, (b) aspect ratio e, versus time following the initial contact between drop and pool. The impact condition is Fr=117.9 We=100.3. t_s is the time span between the anion drop first contacting the bulk/air interface to completely separating from the air interface.

with possibly, the air bubble entrapment. The drop shape relaxes back to higher deformation following separation. Following which, over the long time scale, the drop starts to slowly recover its shape toward spherical. After 15 minutes, the bead aspect ratio reaches 0.92.

In conclusion, the shape deformation of the impacting anion drop can be divided into two phases: the fast deformation and recovery in the horizontal direction in the short time scale of about ten milliseconds, and the long time shape recovery toward spherical, in the time scale of seconds.

The dynamic forces involved in shape deformation/recovery following reactive drop impact are discussed here. As seen from figure 4.3, the direct outcome of drop impact is the spread of the drop liquid and formation of an air crater. The magnitude of the drop spreading, which is represented by the maximum expansion ratio β_{max}, depends on the kinetic energy of the impacting drop liquid, as in the case of a liquid drop impact onto a solid substrate [120]. A deformed immiscible drop, subjected to no external force, can quickly recover to a spherical shape under the effect of surface tension, e.g. a water drop recovers a spherical shape after impact onto an oil pool. In the context of drop impact onto a miscible and reactive gelling pool, membrane formation at the surface interferes with the drop spreading process, and aids the recovery process. Over the long time scale, gelling reaction and osmotic pressure-induced drop shape recovery come into play. The process of gelling reaction is illustrated in figure A.2. At the drop/bulk interface, the smaller divalent cation (Ca^{2+}) molecules first diffuse from bulk into the anion solution, and bind negatively charged sites along the polyelectrolyte molecular chains to form a solid-like network structure. This results in an intermediate semi-permeable membrane

around the drop interface, providing elastic membrane tension to the drop-bulk interface. On the other hand, the newly formed membrane restrains the poly-anion molecules from diffusing into the bulk, while allowing the cation to enter the complex, giving rise to an osmotic pressure between inside and outside of the drop complex. The osmotic pressure will be balanced by the membrane tension and finally reach a stable value when all the free poly-anion molecules inside the membrane are bonded. In complying with the minimum free energy requirement, both membrane tension and osmotic effect tend to recover the dramatically deformed drop shape into a spherical one.

It is proposed that the final shape of gelled capsule depends on the competition between shape recovery process and solidification of the drop complex. The ideal case for capsule formation is that the gelling reaction proceeds at a rate such that the solidification of drop liquid completes just after the drop complex shape recovers to spherical. However, if the membrane tension is not high enough to fully recover the spherical shape before solidification is complete, then the final capsule shape will be irregular.

Figure A.3 shows an example of the irregular capsule shape obtained after gelling a 19.5 cp 0.4/0.4 wt% MVG/CS drop, a similar observation as reported in [9, 41]. Here the lower chemical concentration of the poly-anion solution leads to a weaker membrane formation, especially at the separation region at the top, and lower osmotic pressure, which means the shape recovery process is weaker. In addition, when the chemical concentration is lowered, the viscosity of poly-anion drop decreases. Thus the shape of lower chemical concentration drop is more susceptible to the nearby bulk flow such as focusing or reversal flow. As a result, the final completely gelled capsule has an irregular

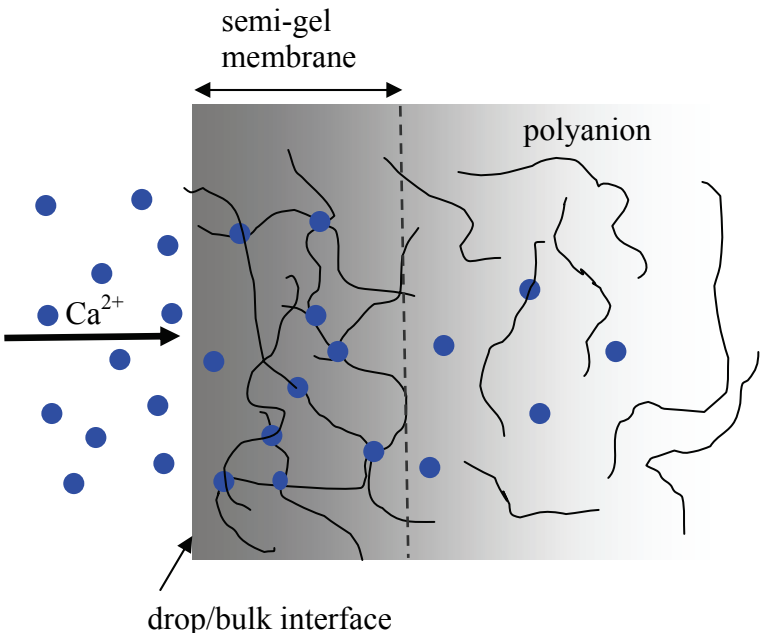

Figure A.2. Schematic showing the gelling process at the drop/bulk interface.

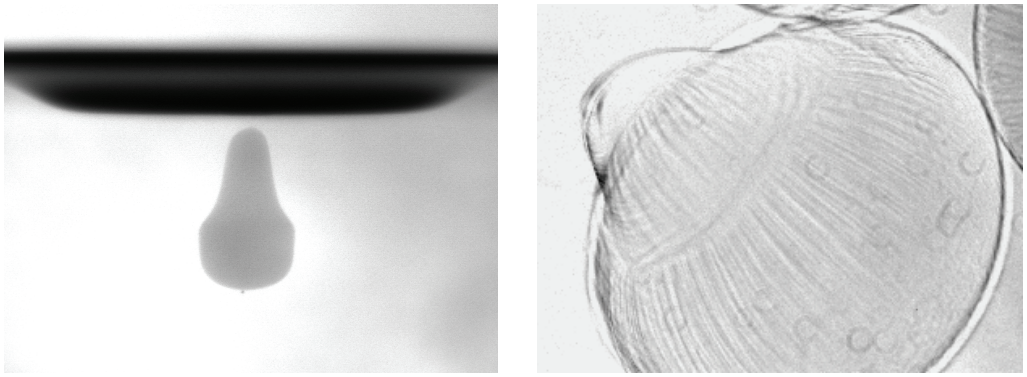

(a) (b)

Figure A.3. Pictures showing the irregular shape of the capsule made by dispensing 0.4/0.4 wt% MVG/CS (viscosity 19.5 cp) drop onto the gelling pool. (a). The drop complex shape right after its separation from the impacting crater. (b). Microscopic picture showing the irregular shape and strong wrinkles of the completely gelled capsule surface.

shape. Current experiments suggest that, the capsule can recover into a nearly spherical shape only if the poly-anion drop viscosity is higher that 59 cp, corresponding to chemical concentration of 0.6/0.6 wt% MVG/CS.

To demonstrate the effect of gelling reaction on drop shape evolvement, three pool liquids were used for the encapsulation experiments: 0.76 wt% $CaCl_2$ in PBS (0.9% NaCl solution), pure water, and 1 cs silicon oil. The drop liquid is 0.8/0.8 wt% MVG/CS mixture, which is released from a height of 15 cm above the pool surface for all the three experiments, with a constant drop diameter of 2.50 mm. The measured drop expansion ratio for the three cases is shown in figure A.4. For the water receiving pool, there is no drop/bulk interfacial tension since the two liquids are miscible. However, the drop/bulk interface is still observable because the diffusion rate is slow for poly-anion molecules. The measured maximum expansion ratio is 2.07, which occurs at 6.6 ms after initial contact. In longer time, the poly-anion liquid slowly diffuses and mixes with water, and the interface is no longer detectable. To the opposite, the interface between 1 cs silicon oil and water-based poly-anion is totally immiscible and chemically inert, so the drop/bulk interfacial tension is kept as a constant, which serves to restrain the spreading of drop liquid into the bulk. The corresponding β_{max} = 1.70, which is lower than the miscible non-reactive system, as expected. After impact, the drop liquid recovers to a spherical shape, due to the constant surface tension between the two liquids. For the third instance, the binding cation, Ca^{2+}, is presented in the water-based bulk liquid; thus the drop/bulk interface turns to be miscible but reactive. The maximum expansion ratio in this case is close to the immiscible system, which indicates the presence of interfacial/membrane tension. One important finding from figure A.4 is that the gelation

starts to affect the drop morphology as early as a few milliseconds after the initial contact between the drop and the bulk. This time scale is comparable to the drop deformation time scale (D/V), suggesting that the gelling reaction and shape deformation are two competing processes. It is also noted that although interfacial gelling reaction starts to compete with drop deformation as early as a few ms, the completion of gelation of the entire drop takes minutes. This can be explained by the higher diffusion impedance for Ca^{2+} as gel structure builds up, and the slow chemical process of the molecular structure rearrangement [6].

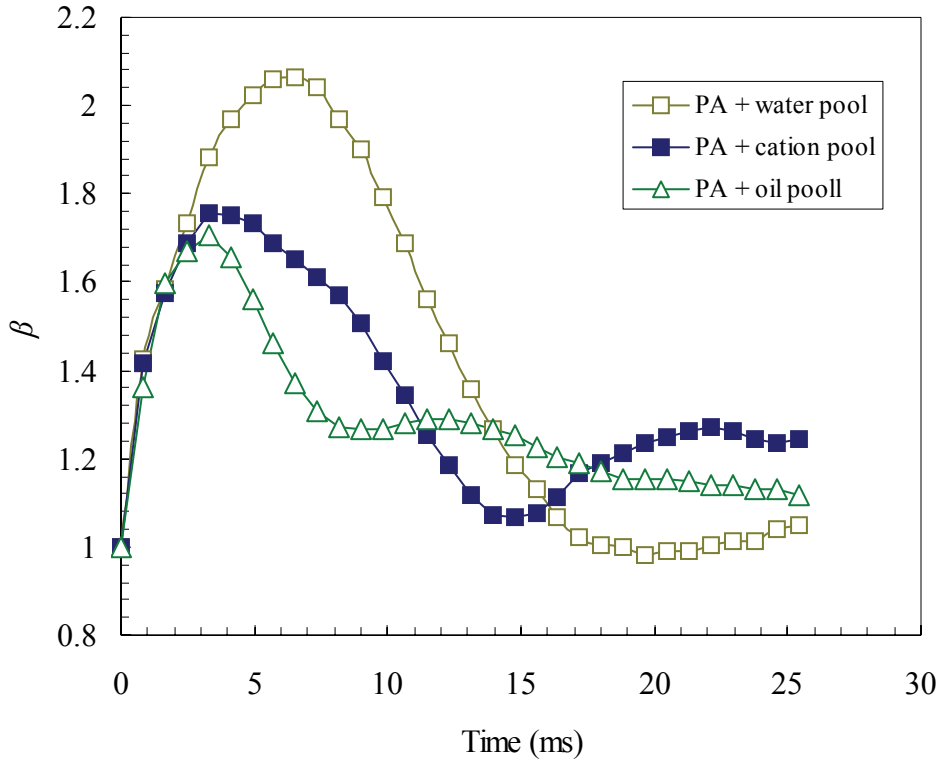

Figure A.4. Comparison of short term drop deformation profiles measured as same poly-anion drop (0.8/0.8 wt% MVG/CS) impacts onto different receiving pools: (□) pure water, (■) 0.76% $CaCl_2$ in PBS, (○) 1 cs silicon oil. (D=2.5mm, V=1.67m/s, We = 100.3).

The gelling induced membrane tension, during drop deformation, can be qualitatively evaluated by measuring the maximum drop expansion ratio during the impact. Since the membrane tension always counteracts the drop spreading, it must always induce a lower β_{max}. Figure A.5 shows the measured maximum expansion ratios for different concentrations of $CaCl_2$ and NaCl, where the impacting kinetic condition is kept the same. For lower $CaCl_2$ concentration region, β_{max} decreases continuously as $CaCl_2$ concentration increases, indicating a stronger membrane is formed. In addition, β_{max}. appears to reach a limiting value as $CaCl_2$ concentration is continuously increased above a saturation concentration.

The Na^+ anti-gelling effect is evidenced by the fact that in the low $CaCl_2$ concentration regime, β_{max} increases slightly as more NaCl is added in the gelling solution for the same $CaCl_2$ concentration (see figure A.5). This is because Na^+ competes against Ca_2^+ for the binding sites in the polyelectrolyte complex and therefore less inter-molecular junctions are formed [24,55,121]. Our experiments also show that as $CaCl_2$ concentration increased to greater than saturation value, the Na^+ concentration appears to no longer affect β_{max}..

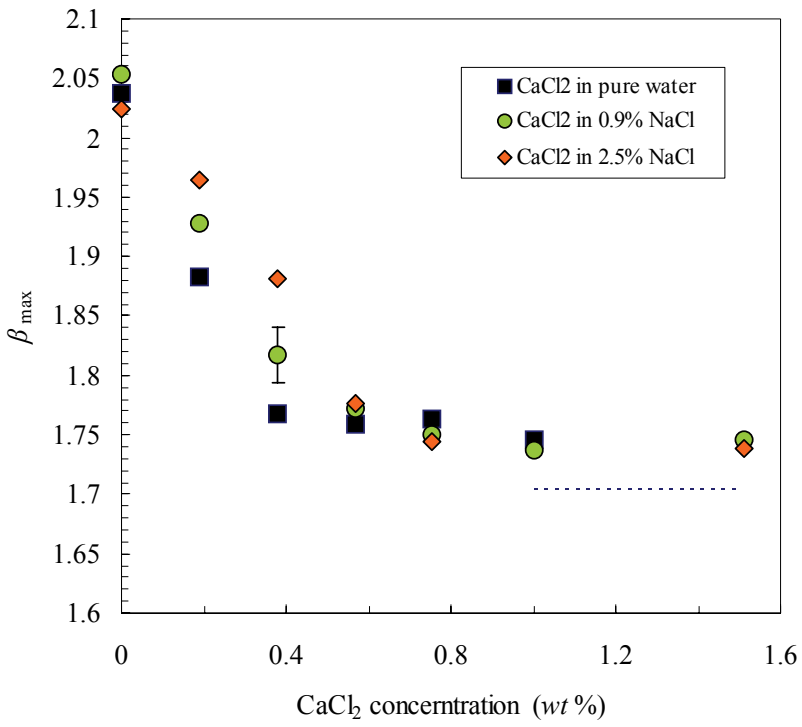

Figure A.5. Maximum expansion ratio of poly-anion drops versus chemical concentrations of the receiving cation solution. The impacting condition for all the data is the same (D=2.50 mm, V=1.70m/s, We = 100.3). The dotted line shows the β_{max} value obtained when the same poly-anion drop impacts on a 1 cs oil pool.

APPENDIX B

SURFACE WRINKLES ISSUE

Surface wrinkles formation is another evidence showing the competition between drop deformation-relaxation and gelation process in the reactive drop studies. Given that the gelation, of the surface layers, proceeds in the same time scale as drop deformation, the newly formed membrane at the expanded drop surface will result in surface wrinkles once that area contracts during the shape recovery phase (figure B.1). In fact, the observed wrinkles are all perpendicular to the capsule circumference and mostly located on the equatorial area (figure 4.1), where the area expansion/contraction ratio is the highest.

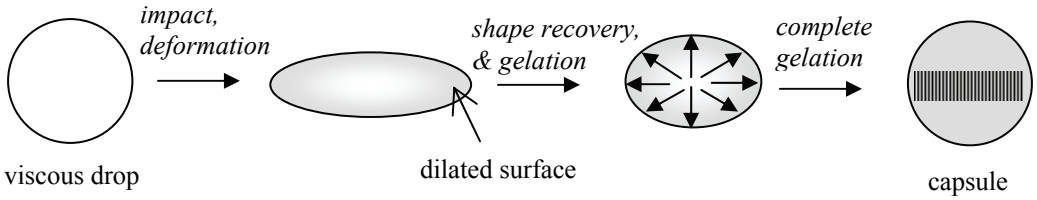

Figure B.1. Schematic drawing showing the formation of equatorial wrinkles on the capsule surface.

One immediate approach to reducing capsule's surface wrinkle is to reduce the amplitude of the drop deformation, represented by β_{max}, during drop impact, so as to lower the area dilation ratio at the equatorial region of the drop surface. In the context of liquid drop impact onto solid substrate, β_{max} has been found to be closely related to the kinetic condition of the impacting drop, which is usually measured as Weber number, *We*. The spread of drop liquid is a process of transformation of the kinetic energy of the impact liquid drop into the surface energy induced by the expansion. Drop impact with higher *We* (higher impact velocity and bigger drop size) will induce higher degree of drop spreading upon impact [120]. Figure B.2 shows β_{max} obtained in reactive drop impact experiments with different drop size and dispensing height, versus *We*. It is noted that the maximum expansion ratio increases with *We*, following the power scale: $\beta_{max} \sim We^{0.163}$. The observed *We* dependence is weaker than the case when drop impacts onto a solid surface, where $\beta_{max} \sim We^{0.25}$ [120]. This is because in the former case the impacting energy is also partially transformed to gravitational potential and surface energy stored in the impact crater. For each impact condition in figure B.2, the completely gelled capsules were collected and the surfaces were examined using a phase contrast microscope, as in the sample pictures seen in the inserts of figure B.2. The result suggests that the surface wrinkles are not observable when the maximum expansion ratio during impact is lower than 1.6. Accordingly, the wrinkle-free operational condition for the 0.8/0.8 wt% MVG/CS system appears to be $We < 60$.

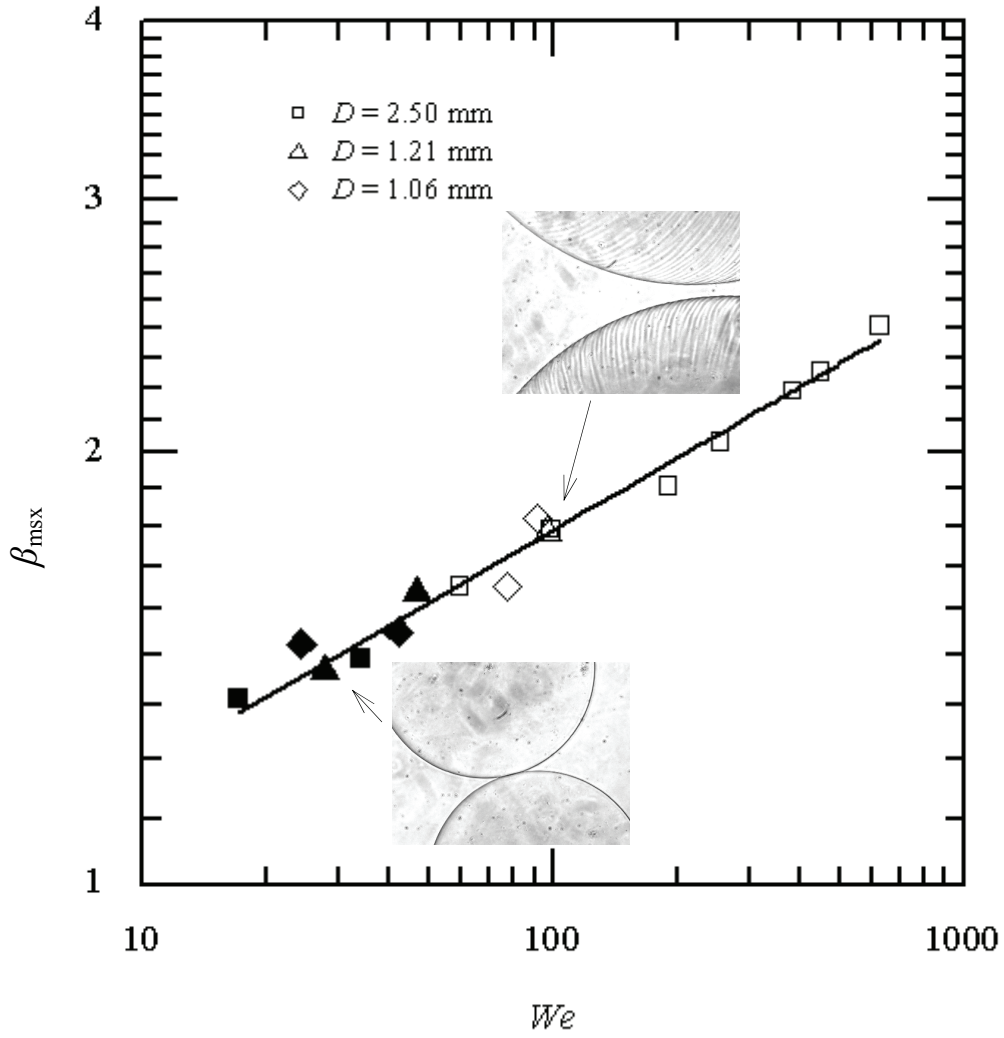

Figure B.2. Maximum expansion ratio of a poly-anion drop during impact versus the impacting *We* number. Poly-anion drop: 0.8/0.8 wt% MVG/CS; gelling solution: 0.76%, $CaCl_2$ in PBS. Open symbols denote that equatorial wrinkles are observed on the surface of completely gelled capsules and solid symbols denote that capsules are free of visible wrinkles. The solid line is a power-law fit to the experimental data.

APPENDIX C

SMALLER BUBBLE ENTRAPMENT DURING INITIAL CONTACT

In reactive drop impact experiments, besides the bubble entrapment observed during the crater collapse, a different type of bubble entrapment is also observed at the bottom of the impacting drop, within 1 ms after the initial drop-bulk contact. This bubble entrapment is most possibly caused by the rapid contraction of the thin air sheet entrapped during the initial contact between the drop bottom and pool/substrate surface, as illustrated in figure C.1. Recently, Thoroddsen *et al.* [64,122] studied this particular bubble entrapment in drop impact with the aid of ultra-high speed photography. In their observation of water drop impact onto water pool, the rapid contraction of air sheet usually leads to a pair of air bubbles being entrapped.

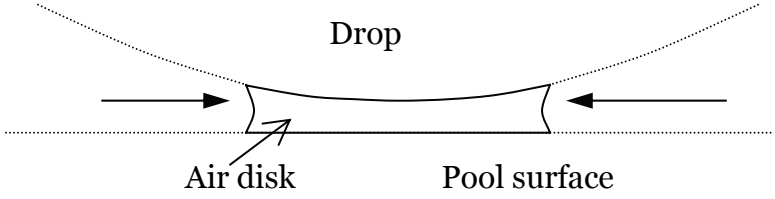

Figure C.1. Sketch showing the bubble entrapment during the initial contact between drop and pool surface.

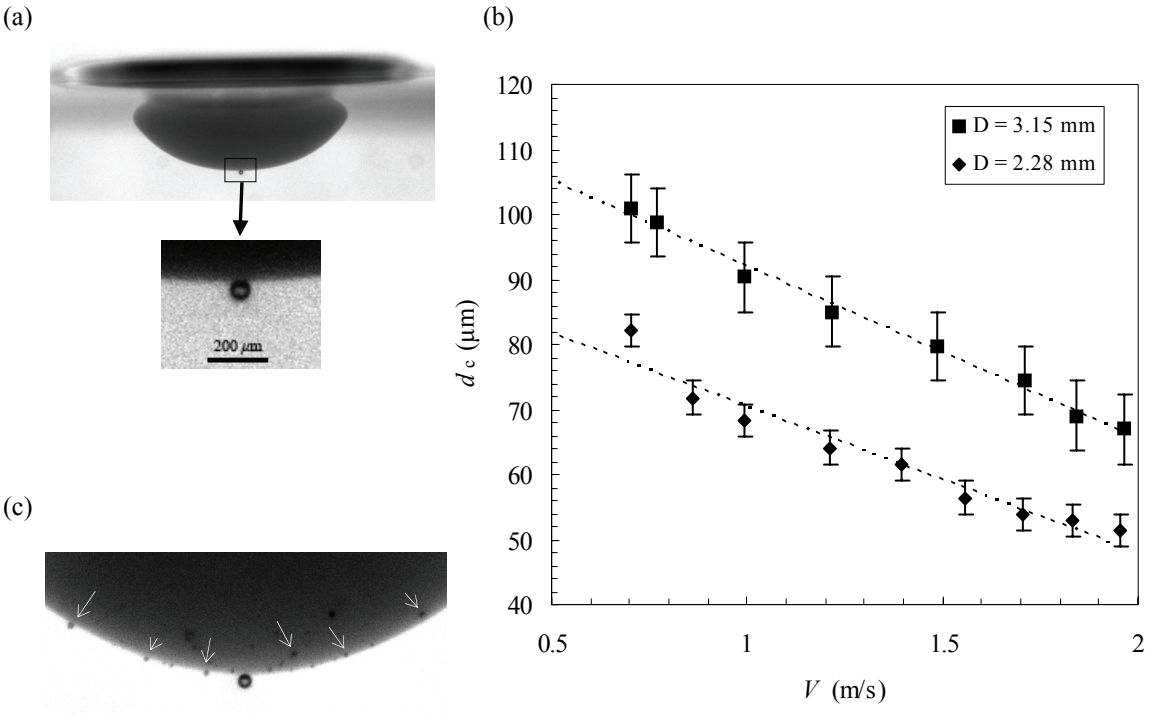

Figure C.2. Bubble entrapment due to the initial contact between drop and pool liquid. (a) Picture showing the location and size of the entrapped bubble following a 2.28 mm PA drop impact onto a gelling pool at We = 46.6. (b) Measured entrapped bubble size, d_c, versus impacting velocity, V. (c) Picture showing at lower entrapment velocity (We = 15.7), a trail of micro bubbles observed near the drop bottom, in addition to the big one located on the symmetric axis.

Figure C.2.a shows this smaller bubble entrapment observation in the reactive drop impact experiments. Here only one bubble is observed after the contraction, as compared with bubble pair in water system, probably because one side of the air sheet is less compliant due to the higher viscosity of the drop liquid. Figure C.2.b shows the measured bubble diameters as a function of impacting velocity. The bubble size is about one order smaller than the bubble entrapped due to the crater collapse. Owing to the smaller size,

these bubbles may not easily collapse or flow away from the drop surface as the big bubbles do. For the same impacting drop size, the entrapped bubble size is found to decrease linearly as the impacting velocity increases. This result agrees with the Thoroddsen *et al.*'s finding about the correlation between the air sheet thickness and Reynolds number [64]. It is also noted that the entrapped bubble size is bigger for bigger impact drop size (D), under same impact velocity, suggesting this particular entrapment is sensitive to the curvature of the impacting surface.

At very low impact velocity, more than one, even smaller, micro bubbles are entrapped and scatter over a small area near the drop bottom, as seen in figure C.2.c. The size of these micro bubbles is in the order of ten microns, which cannot be measured precisely using current optical set up. Thoroddsen *et al.*'s high speed photograph shows that at very low impacting energy, the air sheet is deformed into a spherical cap before contraction happens. The curvature of the sheet generates a component of capillary force perpendicular to the horizontal direction, which disintegrates the air sheet during retraction. This may explain the entrapment of micro bubble trails observed in the very low We impact experiment. The role of chemical reaction, if any, in promoting such bubble entrapment needs to be further explored.

REFERENCES

1. *Cell Encapsulation Technology and Therapeutics,* edited by W. M. Kuthreiber, R. P. Lanza and W. L. Chick, 1st ed., Boston, Basel, Berlin: Birkhauser (1999).

2. *Principles of Tissue Engineering,* edited by R. P. Lanza, R. Langer and J. P. Vacanti, 2nd ed., San Diego, San Francisco, New York Boston, London, Sydney, Tokyo: Academic Press (2000).

3. R. P. Lanza, J. L. Hayes and W. L. Chick, "Encapsulated cell technology," Nature Biotechnology, **14**, 1107 (1996).

4. A. Moer, V. Duvivier-Kali, J. Fernandes, V. Tchipashivili, C. K. Colton and G. C. Weir, "Long-term normoglycemia in rats receiving transplantation with encapsulated islets," Transplantation, **79** (2005).

5. R. P. Lanza, R. Jackson, A. Sullivan, J. Ringeling, C. McGrath, W. M. Kuthreiber and W. L. Chick, "Xenotransplantation of cells using biodegradable microcapsules," Transplantation, **67**, 1105 (1999).

6. I. Lacik, M. Brissova, A. V. Anilkumar, A. C. Powers and T. Wang, "New capsules with tailored properties for the encapsulation of living cells," Journal of Biomedical Material Research, **39**, 52 (1998).

7. T. G. Wang, I. Lacik, M. Brissova, A. V. Anilkumar, A. Prokop, D. Hunkeler, R. Green, K. Shahrokhi and A. C. Powers, "An encapsulation system for the immunoisolation of pancreatic islets," Nature Biotechnology, **15**, 358 (1997).

8. P. Soon-Shiong, R. E. Heintz, N. Merideth, Q. X. Yao, Z. Yao, T. Zheng, M. Murphy, M. K. Moloney, M. Schmehl, M. Harris, R. Mendez, R. Mendez and P. A. Sanford, "Insulin independence in a type q diabetic patient after encapsulated islets transplantation," The Lancet, **343**, 950 (1994).

9. E. C. Opara and W. F. Kendall, "Immunoisolation techniques for islet cell transplantation," Expert Opinion on Biological Therapy, **2**, 503 (2002).

10. G. Olive, R. M. Hernandez, A. R. Gascon, R. Calafiore, T. M. S. Chang, P. De Vos, G. Hortelano, D. Hunkeler, I. Lacik, A. M. J. Shapiro and J. L. Pedraz, "Cell encapsulation: Promise and progresses," Nature, **9**, 104 (2003).

11. A. C. Powers, M. Brissova, I. Lacik, A. V. Anilkumar, K. Shahrokhi and T. G. Wang, "Permeability assessment of capsules for islets transplantation," Annals of the New York Academy of Science, **831**, 208 (1997).

12. T. G. Wang and R. P. Lanza, "Bioartificial pancreas," in *Principles of Tissue Engineering,* edited by R. P. Lanza, R. Langer and J. P. Vacanti, 2nd ed., 495, San Diego, San Francisco New York Boston, London, Sydney, Tokyo: Academic Press (2000).

13. M. Brissova, I. Lacik, A. C. Powers, A. V. Anilkumar and T. G. Wang, "Control and measurement of permeability for design of microcapsule cell delivery system," Journal of Biomedical Material Research, **39**, 61 (1998).

14. F. Lim and A. M. Sun, "Microencapsulation islets as bioartificial endocrine pancreas," Science, **210**, 908 (1980).

15. F. W. Wolters GH, Gerrits D, van Schilfgaarde R., "A versatile alginate droplet generator applicable for microencapsulation of pancreatic islets," Journal of Applied Biomaterial, **3**, 281 (1991).

16. L. F. Halle JP, Pariseau JF, Jutras P, Brabant MJ, Lepage Y., "Studies on small (< 300 microns) microcapsules: II--Parameters governing the production of alginate beads by high voltage electrostatic pulses," Cell Transplant, **3**, 365 (1994).

17. Y. Senuma, C. Lowe, Y. Zweifel, J. G. Hilnborn and I. Marison, "Alginate hydrogel microspheres and microcapsules prepared by spinning disk atomization," Biotechnology and Bioengineering, **67**, 616 (2000).

18. D. Poncelet, "Production of alginate beads by emulsification/internal gelation," Annals of the New York Academy of Science, **944**, 74 (2001).

19. S. Sakai, K. Kawabata, T. Ono and K. Kawakami, "Preparation of mammalian cell-enclosing subsieve-sized capsules (<100 μm) in a coflowing stream," Biotechnology and Bioengineering, **86**, 168 (2004).

20. I. Cohen, H. Li, J. L. Hougland, M. Mrksich and S. R. Nagel, "Using selective withdrawal to coat microparticles," Science, **292**, 265 (2001).

21. A. Blandino, M. Macias and D. Cantero, "Formation of calcium alginate gel capsules: influence of sodium alginate and $CaCl_2$ concentration on gelation Kinetics," (1999).

22. C. Bienaime, J.-N. Barbotin and J.-E. Nava-Saucedo, "How to build an adapted and bioactive cell microenvironment? A chemical interaction study of the structure of Ca-alginate matrices and their repercussion on confined cells," Journal of Biomedical Material Research, **67A**, 376 (2003).

23. M. Heinemann, H. Meinberg, J. Büchs, H.-J. Koss and M. B. Ansorge-Schumacher, "Method for quantitative determination of spatial polymer

distribution in alginate beads using Raman spectroscopy," Applied Spectroscopy, **59**, 280 (2005).

24. K. Xu, D. M. Hercules, I. Lacik and T. G. Wang, "Atomic force microscopy used for the surface characterization of microcapsule immunoisolation devices," Journal of Biomedical Material Research, **41**, 461 (1998).

25. A. V. Anilkumar, I. Lacik and T. G. Wang, "A novel reactor for making uniform capsules," Biotechnology and Bioengineering, **75**, 581 (2001).

26. G. C. Weir. "Encapsulation of islets: how difficult are the problems. in Encapsulation and Immunoprotective strategies of islet cells". 2001. Washington DC: RTI-center for technology applications.

27. P. De Vos, C. G. Hoogmoed, B. J. d. Haan and H. J. Busscher, "Tissue responses against immunoisolating alginate-PLL capsule in the immediate post-transplant period," Journal of Biomedical Material Research, **62**, 430 (2002).

28. A. King, S. Sandler and A. Anderson, "The effect of host factors and capsule composition on the cellular overgrowth on implanted alginate capsules," Journal of Biomedical Material Research, **57**, 374 (2001).

29. P. De Vos, C. G. Hoogmoed and H. J. Busscher, "Chemistry and Biocompatability of alginate-PLL capsules for immunoprotection of mammalian cells," Journal of Biomedical Material Research, **60**, 252 (2002).

30. S. Juste, M. Lessard, N. Henley, M. Menard and J.-P. Halle, "Effect of poly_l-lysine coating on macrophage activation by alginate-based microcapsules: Assessment using a new in virtro method," Journal of Biomedical Material Research, **72A**, 389 (2005).

31. P. De Vos, C. G. v. Hoogmoed, J. v. Zanten, S. Netter, J. H. Strubbe and H. K. Busscher, "Long-term biocompatibility, chemistry, and function of microencapsulated pancreatic islets," Biomaterials, **24**, 305 (2003).

32. P. De Vos, B. D. Haan, J. Pater and R. V. Schilfgaarde, "Association between capsule diameter, adequacy of encapsulation, and survival of microencapsulation rat islet allografts," Transplantation, **62**, 893 (1996).

33. P. De Vos, B. D. Haan, G. H. J. Wolters and R. V. Schilfgaarde, "Factors influencing the adequacy of microencapsulation of rat pancreatic islets," Transplantation, **62**, 888 (1996).

34. D. R. Cole, M. Waterfall, M. McIntyre and J. D. Baird, "Microencapsulated islet grafts in the BB/E rat: a possible role for cytokines in graft failure," Diabetogia, **35**, 231 (1992).

35. R. Robitalle, F. A. Leblond, N. Henley, G. J. Prudhomme, E. Drobetsky and J.-P. Halle, "Alginate-poly-L-lysune microcapsule biocompatibility: A nove; RT-PCR method for cytokine gene expression analysis in pericapsular infiltrates," Journal of Biomaterial Research, **45**, 223 (1999).

36. A. King, A. Anderson and S. Sandler, "Cytokine-induced functional suppression of microencapsulated rat pancreatic islets in virtro," Transplantation, **70**, 380 (2000).

37. R. G. Gill, "Direct and indirect pathways of immunity to pancreatic islet transplants," Transplantation Reviews, **12**, 85 (1998).

38. R. G. Gill, "Celluar immunity to immunoisolated transplants," in *Encapsulation and Immunoprotective strategies of islet cells*. 2001. Washington DC: RTI-center for technology applications.

39. P. De Vos, B. J. De Haan, G. H. Wolters, J. H. Strubbe and V. S. R., "Improved biocompatibility but limited graft survival after purification of alginate for microencapsulation of pancreatic islets," Diabetogia, **40**, 262 (1997).

40. Y. L. Sun, X. Ma, D. Zhou, I. Vacek and A. M. Sun, "Porcine pancreatic islets: isolation, microencapsulation, and xenotransplantation," Artificial Organs, **17**, 727 (1993).

41. M. F. A. Goosen, G. M. OShea and H. M. Gharapetian, "Optimization of microencapsulation parameters: semipermeable microcapsules as a bioartificial pancreas," Biotechnology and Bioengineering, **27**, 146 (1985).

42. W. F. Kendall, M. D. Darrabie, H. M. EL-Shewy and E. C. Opara, "Effect of alginate composition and purity on alginate microspheres," Journal of Microencapsulation, **21**, 821 (2004).

43. A. Prokop and T. G. Wang, "Purification of polymers used for an immunoisolation barrier," Annals of the New York Academy of Science, **831**, 223 (1997).

44. U. Zimmermann, G. Klock, K. Federlin, K. Hannig, M. Kowalski, R. G.Bretzel, A. Horcher, H. Entenmann, U. Siber and T. Zekorn, "Production of mitogen-contamination free alginates with variable ratios of mannuronic acid to guluronic acid by free flow electrophoresis," Electrophoresis, **13**, 269 (1992).

45. G. Klock, H. Frank, R. Houben, T. Zekorn, A. Horcher, U. Siebers, M. Wohrle, K. Federlin and U. Zimmermann, "Production of purified alginates suitable for use in immunoisolated transplantation," Applied Microbiology and Biotechnology, **40**, 638 (1994).

46. P. De Vos, B. De Haan and R. Van Schilfgaarde, "Effect of the alginate composition on the biocompatibility of alginate-polylysine microcapsules," Biomaterials, **3**, 273 (1997).

47. P. De Vos, A. F. Hamel and K. Tataykiwicz, "Considerations for successful transplantation of encapsulated pancreatic islets," Diabetologia, **45**, 159 (2002).

48. C. M. Bunger, C. Gerlach, T. Freier, K. P. Schmitz, M. Pilz, C. Werner, L. Jonas and W. Schareck, "Biocompatibility and surface structure of chemically modified immunoisolating alginate-PLL capsules," Journal of Biomedical Material Research, **67A**, 1219 (2003).

49. A. King, V. Strand, A.-M. Rokstad, B. Kulseng, A. Andersson, G. Skjak-Brak and S. Sandler, "Improvement of the biocompatibility of alginate/poly-l-lysince/alginate microcapsules by the use of epimerized alginate as a coating," Journal of Biomedical Material Research, **64A**, 533 (2003).

50. B. L. Strand, T. A. Morch, K. R. Syvertsen, T. Espevik and G. Skjak-Brak, "Microcapsules made by enzymatically tailored alginate," Journal of Biomaterial Research, **64**, 540 (2003).

51. R. Robitaille, J. F. Pariseau, F. A. Leblond, L. M., L. Y. and H. J.P., "Studies on small (<350 microm) alginate-poly-L-lysine microcapsules. III. Biocompatibility Of smaller versus standard microcapsules," Journal of Biomaterial Research, **44**, 116 (1999).

52. T. M. Chang, "Artificial cells and bioencapsulation in bioartificial organs," Annals of the New York Academy of Science, **831**, 249 (1997).

53. M.-Y. Fan, Z.-P. Lum, X.-W. Fu, L. Levesque, I. T. Tai and A. M. Sum, "Reversal of diabetes in NN rates by transplantation of encapsulated pancreatic islets," Diabetes, **39**, 519 (1990).

54. R. P. Lanza, K. M. Borland, P. Lodge, M. Carretta, S. J. Sullivan, T. E. Muller, B. A. Solomon, T. Maki, A. P. Monaco and W. A. Chick, "Treatment of severely diabetic pancreatectomized dogs using a diffusion-based hybrid pancreas," Diabetes, **41**, 886 (1992).

55. I. Lacik, A. V. Anilkumar and T. G. Wang, "A two step process for controlling the surface smoothness of polyelectrolyte-based microcapsules," Journal of Microencapsulation, **18**, 479 (2001).

56. S.-T. Lin, T.-H. Young and Y. Fang, "Studies on the effect of surface properties on the biocompatibility of polyurethane membranes," Biomaterials, **22**, 1521 (2001).

57. S. Y. Chae, Y. Y. Kim, S. W. Kim and Y. H. Bae, "Prolonged glucose normalization of streptozotocin-induced diabetic mice by transplantation of rat islets co-encapsulated with crosslinked hemoglobin," Transplantation, **78** (2004).

58. S. Kim, S. Y. Chae, K. Na, S. W. Kim and Y. H. Bae, "Insulinotropic activity of sulfonylurea/pullulan conjugate in rat islet microcapsule," Biomaterials, **24** (2003).

59. J. M. Dufour, R. V. Rajotte, G. S. Korbutt and D. F. Emerich, "Harnessing the Immunomodulatory Properties of sertoli cells to enable xenotransplantation in type I diabetes," Immunological Investigations, **32**, 275 (2003).

60. G. S. Korbutt, A. Ao, M. Flasner, J. F. Elliott and R. V. Rajotte, "Coencapsulation of allogenic islets with allogeneic sertoli cells prolongs graft survival without systemic immunosuppression," Transplantation Proceedings, **30**, 419 (1998).

61. R. Calafiore, G. Luca, M. Calvitti, L. M. Neri, G. Basta, S. Capitani, E. Becchetti and P. Brunetti, "Cellular support systems for alginate microcapsules containing Islets, as composite bioartificial pancreas," Annals of the New York Academy of Science, **944**, 240 (2001).

62. A. V. Anilkumar, C. P. Lee and T. G. Wang, "Surface -tension-induced mixing following coalescence of initially stationary drop," Physics of Fluids A, **3**, 2587 (1991).

63. A. Prosperetti and H. Oguz, "The impact of drops on liquid surfaces and the underwater noise of rain," Annual Review of Fluid Mechanics, **25**, 577 (1993).

64. S. T. Thoroddsen, T. G. Etoh and K. Takehara, "Air entrapment under an impacting drop," Journal of Fluid Mechanics, **478**, 125 (2003).

65. L. J. Leng, "Splash formation by spherical drops," Journal of Fluid Mechanics, **427**, 73 (2001).

66. Y. Couder, E. Fort, C.-H. Gautier and A. Boudaoud, "From bouncing to floating: noncoalescence of drops on a fluid Bath," Physical Review letter, **94**, 1 (2005).

67. R. W. Cresswell and B. R. Morton, "Drop-formed vortex rings-the generation of vorticity," Physics of Fluids, **7**, 1363 (1995).

68. B. S. Dooley, A. E. Warncke, M. Gharib and G. Tryggavason, "Vortex ring generation due to the coalescence of a water drop at a free surface," Experiments in Fluids, **22**, 369 (1997).

69. M. Hsiao, S. Lichter and L. G. Quintero, "The critical Weber number for vortex and jet formation for drops impacting on a liquid pool," Physics of Fluids, **31**, 3560 (1988).

70. D. S. Chapman and P. R. Critchlow, "Formation of vortex rings from falling drops," Journal of Fluid Mechanics, **29**, 177 (1967).

71. F. Rodriguez and R. Mesler, "The penetration of drop-formed vortex ring into pools of liquid," Journal of Colloid and Interfacial Science, **121**, 121 (1988).

72. M. Rein, "The transitional regime between coalescing and splashing drops," Journal of Fluid Mechanics, **306**, 145 (1996).

73. H. C. Pumphrey and P. A. Elmore, "The entrainment of bubbles by drop impacts," Journal of Fluid Mechanics, **220**, 539 (1990).

74. H. N. Oguz and A. Prosperetti, "Bubble entrainment by impact of drops on liquid surfaces," Journal of Fluid Mechanics, **219**, 143 (1990).

75. P. A. Elmore, G. L. Chahine and H. N. Oguz, "Cavity and flow measurements of reproducible bubble entrainment following drop impacts," Experiments in Fluids, **31**, 664 (2001).

76. D. Morton, M. Rudman and L. J. Leng, "An investigation of the flow regimes resulting from splashing drops," Physics of Fluids, **12**, 747 (2000).

77. H. N. Oguz and A. Prosperetti, "Dynamics of bubble growth and detachment from a needle," Journal of Fluid Mechanics, **257**, 111 (1993).

78. M. S. Longuet-Higgins, "An analytic model of sound production by raindrops," Journal of Fluid Mechanics, **214**, 395 (1990).

79. M. S. Longuet-Higgins, "Bubbles, breaking waves and hyperbolic jets at a free surface," Journal of Fluid Mechanics, **127**, 103 (1983).

80. B. W. Zeff, B. Kleber, J. Fineberg and D. P. Lathrop, "Singularity dynamics in curvature collapse and jet eruption on a fluid surface," Nature, **403**, 401 (2000).

81. J. E. Hogrefe, N. L. Peffley, C. L. Goodridge, W. T. Shi, H. G. E. Hentschel and D. P. Lathrop, "Power-law singularities in gravity-capillary waves," Physica D, **123**, 183 (1998).

82. R. Bergmann, D. v. d. Meer, M. Stijnaman, M. Sandtke, A. Posperetti and D. Lohse, "Giant bubble pinch-off," Physical Review Letters, **96**, 154505 (2006).

83. D. Lohse, R. Bergmann, R. Mikkelsen, C. Zeilstra, D. v. d. Meer, M. Versluis, K. v. d. Weele, M. v. d. Hoef and H. Kuipers, "Impact on soft sand: void collapse and jet formation," Physical Review Letters, **93**, 198003 (2004).

84. J. C. Burton, R. Waldrep and P. Taborek, "Scaling and instabilities in bubble pinch-off," Physical Review Letters, **94**, 184502 (2005).

85. J. M. Gordillo, A. Sevilla, J. Rodriguez-Rodriguez and C. Martinez-Bazan, "Axisymmetric bubble pinch-off at high Reynolds numbers," Physical Review Letters, **95**, 194501 (2005).

86. D. Leppinen and J. R. Lister, "Capillary pinch-off in inviscid fluids," Physics of Fluids, **15**, 568 (2003).

87. M. Rein, "Phenomena of liquid drop impact on solid and liquid surfaces," Fluid Dynamics Research, **12**, 61 (1993).

88. A. M. Worthington, *A study of splash*, London: Longman's, Green and Company (1908).

89. O. G. Engel, "Crater depth in fluid impacts," Journal of Applied Physics, **37**, 1798 (1966).

90. L. Esmailizadeh and R. Mesler, "Bubble entrainment with drops," Journal of Colloid and Interfacial Science, **110**, 561 (1986).

91. H. N. Oguz and A. Prosperetti, "Surface tension effects in the contact of liquid surfaces," Journal of Fluid Mechanics, **203**, 149 (1989).

92. O. G. Engel, "Initial pressure, initial flow velocity, and the time dependence of crater depth in fluid impacts," Journal of Applied Physics, **38**, 3935 (1967).

93. C. P. Lee, A. V. Anilkumar and T. G. Wang, "Static shape of an acoustically levitated drop with wave-drop interaction," Physics of Fluids, **6**, 3554 (1994).

94. C. Josserand and S. Zalesk, "Droplet splashing on a thin liquid film," Physics of Fluids, **15**, 1650 (2003).

95. C. F. Hsu, "Impaction of a droplet on an orifice plate," Physics of Fluids, **16**, 400 (2004).

96. S. O. Unverdi and G. Tryggvason, "A front tracking method for viscous, incompressible, multi-fluid flow," Journal of Computational Physics, **100**, 25 (1992).

97. M. R. Nobari, Y. J. Jan and G. Traggvason, "Head-on collision of drops - a numerical investigation," Physics of Fluids, **8**, 29 (1996).

98. B. Bunner and G. Tryggvason, "Direct numerical simulations of three-dimensional bubbly flows," Physics of Fluids, **11**, 1967 (1999).

99. A. Esmaeeli and G. Traggvason, "An inverse energy cascade in two-dimensional, low Reynolds number bubbly flow," Journal of Fluid Mechanics, **314**, 315 (1996).

100. D. Juric and G. Tryggvason, "A front tracking method for dentritic solidification," Journal of Computational Physics, **123**, 127 (1996).

101. G. Tryggvason, D. Juric, J. Che, M. R. H. Nobari and S. Nas. *Computations of multiphase flows by a finite difference/front tracking method. III variable surface tension and phase change*. in *29th Computational Fluid Dynamics Lecture Series 1998-03*. 1998: Von Karman Institute for Fluid Dynamics.

102. J. Che, S. L. Ceccio and G. Tryggvason, "Computations of structures formed by the solidification of impinging molten metal drops," Applied Mathematical modeling, **28**, 124 (2004).

103. K. Andsager, K. V. Beard and N. F. Laird, "Laboratory measurements of axis ratios for large raindrops," Journal of the Atmospheric Sciences, 56, 2673 (1999).

104. F. Durst, "Penetration length and diameter development of vortex rings generated by impacting water drops," Experiments in Fluids, 21, 110 (1996).

105. A. N. Dingle and Y. Lee, "Terminal fall speeds of raindrops," Journal of Applied Meteorology, 11, 877 (1972).

106. P. Seitz, "Optical super-resolution using solid-state cameras and digital signal processing," Optical Engineering, 27, 535 (1988).

107. Z. Mohamed-Kassim and E. K. Longmire, "Drop coalescence through a liquid/liquid interface," Physics of Fluids, **16**, 2170 (2004).

108. M. Rein, "Capillary effect at newly formed liquid-liquid contact," Physics of Fluids, **14**, 411 (2002).

109. D. A. Weiss and A. L. Yarin, "Single drop impact onto liquid films: neck distortion, jetting, tiny bubble entrainment, and crown formation," Journal of Fluid Mechanics, **385**, 229 (1999).

110. H. N. Oguz and A. Prosperetti, "Numerical calculations of the underwater noise of rain," Journal of Fluid Mechanics, **228**, 417 (1991).

111. J. T. Jeong and H. K. Moffat, "Free-surface cusps associated with flow at low Reynolds numbers," Journal of Fluid Mechanics, **241**, 1 (1992).

112. H. Lamb, *Hydrodynamics*. 6th ed., New York: Dover Publications (1945).

113. A. Prosperetti, "Viscous effects on small-amplitude surface waves," Physics of Fluids, **19**, 195 (1976).

114. M. S. Longuet-Higgins and H. Oguz, "Critical microjets in collapsing cavities," Journal of Fluid Mechanics, **290**, 183 (1995).

115. L. Oddershede and S. R.Nagel, "Singularity during the onset of an electrohydrodynamic spout," Physical Review Letters, **85**, 1234 (2000).

116. E. B. Dussan V., "On the spreading of liquids on solid surfaces: static and dynamic contact lines," Annual Review of Fluid Mechanics, **11**, 371 (1979).

117. T. D. Blake, M. Bracke and Y. D. Shikhmurzaev, "Experimental evidence of non-local hydrodynamic influence on the dynamic contact angle," Physics of Fluids, **11**, 1995 (1999).

118. N. C. Keim, P. Moller, W. W. Zhang and S. R. Nagel, "Breakup of air bubbles in water: memory and breakdown of cylindrical symmetry," Physical Review Letters, **97** (2006).

119. P. Doshi, I. Cohen, W. W. Zhang, M. Siegel, P. Howell, O. A. Basaran and S. R. Nagel, "Persistence of memory in drop breakup: the breakdown of universality," Science, **302**, 1185 (2003).

120. C. Clanet, C. Beguin, D. Richard and D. Quere, "Maximal deformation of an impacting drop," Journal of Fluid Mechanics, **517**, 199 (2004).

121. C. Ouwerx, N. Velings, M. M. Mestdagh and M. A. V. Axelos, "Physio-chemical properties and rheology of alginate gel beads formed with various divalent cations," Polymer Gels and Networks, **6**, 393 (1998).

122. S. T. Thoroddsen, T. G. Etoh, K. Takehara, N. Ootsuka and Y. Hatsuki, "The air bubble entrapped under a drop impacting on a solid surface," Journal of fluid mechanics, **545**, 203 (2005).